Droplet Condensation on Superhydrophobic Graphite Composites

Dem Fachbereich Maschinenbau und Verfahrenstechnik
der Rheinland-Pfälzischen Technischen Universität Kaiserslautern-Landau
zur Erlangung des akademischen Grades

Doktor-Ingenieur (Dr.-Ing.)

vorgelegte

Dissertation

von

Herr

M.Sc. Raphael Raab

Tag der mündlichen Prüfung: 05.09.2025

Dekan:	Prof. Dr. rer. nat. Roland Ulber
Prüfungsvorsitzender:	Prof. Dr.-Ing. Fabian Jirasek
1. Berichterstatter:	Prof. Dipl.-Ing. Dr. tech. Hans-Jörg Bart
2. Berichterstatter:	Prof. Dr.-Ing. Erik von Harbou
3. Berichterstatter:	Prof. Dr. rer. nat. Egbert Oesterschulze

Kaiserslautern 2025

D386

Abstract

Heat exchangers play a crucial role in the chemical industry, where efficient heat management is essential for maintaining process control, reducing operational costs, and conserving energy. A considerable portion of the energy used in chemical production is associated with the heating and cooling of process fluids. Traditionally, metals such as stainless steel have been employed in heat exchanger construction due to their high thermal conductivity and mechanical robustness. However, their application is often limited by disadvantages such as high weight, high material cost, and susceptibility to corrosion in aggressive chemical environments.

Polymers have emerged as a promising alternative, particularly when reinforced with thermally conductive fillers. These materials combine chemical resistance, low weight, and ease of manufacturing. In this thesis, thermally conductive graphite-filled polymer composites were modified to create superhydrophobic surfaces. This was achieved through a combination of microscale structuring via thermal imprinting, nanostructuring using metal oxide nanostructures (MONSTRs), and subsequent functionalization with fatty acid coatings such as stearic and lauric acid. The resulting surfaces were systematically characterized to evaluate their wetting behavior, condensation dynamics, and heat transfer performance under varying relative humidity conditions.

Experimental results showed that the surface-modified composites achieved contact angles exceeding 170° with contact angle hysteresis below 5°, demonstrating effective superhydrophobicity. Condensation experiments revealed enhanced droplet shedding and significantly higher heat transfer coefficients compared to stainless steel and its filmwise condensation. Furthermore, droplet size distributions were determined from high-resolution imaging and compared with predictions from a population balance model based on the frameworks of Wang et al. [1] and Tancon et al. [2]. While good agreement was found in droplet size distribution, discrepancies in predicted heat fluxes were observed, primarily due to the presence of non-condensable gases (NCGs) in humid air, which are not fully captured by existing models.

These findings underscore the potential of surface-engineered polymer composites to enhance condensation-driven heat transfer and highlight the need for advanced modeling approaches that incorporate the effects of NCGs. The results provide valuable insights into the potential of surface-engineered polymer composites for condensation-based heat transfer enhancement.

Kurzfassung

Wärmetauscher spielen eine entscheidende Rolle in der chemischen Industrie, wo ein effizientes Wärmemanagement für die Aufrechterhaltung der Prozesskontrolle, die Senkung der Betriebskosten und die Energieeinsparung unerlässlich ist. Ein beträchtlicher Teil der in der chemischen Produktion benötigten Energie ist mit dem Erhitzen und Kühlen von Prozessflüssigkeiten verbunden. Traditionell werden Metalle wie Edelstahl aufgrund ihrer hohen Wärmeleitfähigkeit und mechanischen Robustheit für den Bau von Wärmetauschern verwendet. Ihre Anwendung ist jedoch oft durch Nachteile wie hohes Gewicht, hohe Materialkosten und Korrosionsanfälligkeit in aggressiven chemischen Umgebungen eingeschränkt.

Polymere haben sich als vielversprechende Alternative herausgestellt, insbesondere wenn sie mit wärmeleitenden Füllstoffen versehen werden. Diese Materialien vereinen chemische Beständigkeit, geringes Gewicht und einfache Verarbeitung. In dieser Arbeit wurden wärmeleitende, mit Graphit gefüllte Polymerverbundstoffe modifiziert, um superhydrophobe Oberflächen zu erzeugen. Dies wurde durch eine Kombination aus mikroskaliger Strukturierung durch thermisches Prägen, Nanostrukturierung unter Verwendung von Metalloxid-Nanostrukturen (MONSTRs) und anschließender Funktionalisierung mit Fettsäurebeschichtungen wie Stearin- und Laurinsäure erreicht. Die resultierenden Oberflächen wurden systematisch charakterisiert, um ihr Benetzungsverhalten, ihre Kondensationsdynamik und ihre Wärmeübertragungsleistung unter verschiedenen relativen Luftfeuchtigkeit zu bewerten.

Die experimentellen Ergebnisse zeigten, dass die oberflächenmodifizierten Verbundwerkstoffe Kontaktwinkel von über 170° mit einer Kontaktwinkelhysterese von unter 5° erreichten, was eine effektive Superhydrophobie demonstriert. Kondensationsexperimente zeigten eine verbesserte Tröpfchenablösung und deutlich höhere Wärmeübergangskoeffizienten im Vergleich zu Edelstahl und dessen filmartiger Kondensation. Darüber hinaus wurden die Tröpfchengrößenverteilungen mithilfe hochauflösender Bildgebung bestimmt und mit den Vorhersagen eines Populationsbilanzmodells verglichen, das auf den Rahmenbedingungen von Wang u. a. [1] und Tancon u. a. [2] basiert. Während bei der Tröpfchengrößenverteilung eine gute Übereinstimmung festgestellt wurde, wurden bei den vorhergesagten Wärmeströmen Diskrepanzen beobachtet, die hauptsächlich auf das Vorhandensein nicht kondensierbarer Gase (NCGs) in feuchter Luft zurückzuführen sind, die von den bestehenden Modellen nicht vollständig erfasst werden.

Diese Ergebnisse unterstreichen das Potenzial von oberflächenveredelten Polymerverbundwerkstoffen zur Verbesserung der kondensationsgetriebenen Wärmeübertragung und verdeutlichen die Notwendigkeit fortschrittlicher Modellierungsansätze, die die Auswirkungen von nicht kondensierbaren Gasen berücksichtigen. Die Ergebnisse liefern wertvolle Erkenntnisse über das

Potenzial von oberflächenmodifizierten Polymerverbundwerkstoffen zur Verbesserung der kondensationsbasierten Wärmeübertragung.

Contents

1 Introduction

In recent decades, global warming has gained significant prominence in scientific discourse and public awareness due to its far-reaching environmental, economic, and societal impacts [1–4]. This underscores the importance of energy conservation, the reduction of greenhouse gas emissions, and the development of resource-efficient and sustainable technologies [5–7]. The chemical industry is a major consumer of fossil fuels and is therefore responsible for a large proportion of greenhouse gas emissions [8]. A significant portion of the energy consumed in the chemical industry is used for heat management processes, in particular for heating and cooling process fluids, such as the use of steam, which are required to maintain optimal reaction and separation conditions [9].

Heat exchangers are essential components in thermal management systems, as they facilitate efficient heat transfer between working fluids and heating or cooling media while preventing direct mixing between the streams. In general, heat transfer components are made of metals such as stainless steel because of their high thermal conductivity, favorable manufacturability, and robust mechanical properties, which make them suitable for demanding industrial applications. However, stainless steel has notable drawbacks, including high weight and cost. The main limitation of stainless steel is its susceptibility to degradation under corrosive conditions, which can compromise long-term material integrity and performance [10].

Therefore, polymers have aroused the interest of researchers, especially for heat transfer in corrosive environments, such as seawater desalination. The main advantages of polymers are their easy processing, low weight and high corrosion resistance [11]. The major disadvantage of polymers is their poor thermal conductivity, which is a significant challenge for their application in heat exchanger components. A frequently used approach is to reduce the layer thickness of the polymers to lower the thermal resistance and create so-called polymer-film heat exchangers [12], or to fill the polymers with materials that are good heat conductors, such as carbon fibers or graphite particles [10, 13]. Recent studies have demonstrated promising performance in plate heat exchangers made of thermoplastic composites containing graphite. While their heat transfer efficiency is generally lower compared to stainless steel counterparts, polymers offer significant advantages in terms of corrosion resistance and reduced risk of fouling, making them superior in applications where these factors are critical [13].

Furthermore, it has been recognized for nearly a century that heat transfer is significantly enhanced when phase change occurs via droplet formation rather than as a continuous film [14], due to the reduced contact area and improved droplet mobility during dropwise condensation. So condensation can occur in two different ways: as filmwise condensation (FWC) and as dropwise condensation (DWC). In FWC, the condensate forms a continuous liquid film over the heat transfer surface, creating additional thermal resistance that impedes heat flow. In

contrast, DWC is characterized by the formation of individual droplets that cover a smaller portion of the surface. As these droplets grow, they merge and are more effectively removed from the surface, resulting in more efficient heat transfer [15–17]. The condensation behavior is largely determined by the wettability of the surface, with hydrophobic surfaces favoring DWC and hydrophilic surfaces favoring FWC [18, 19]. A scheme of the condensation types is illustrated in Figure 1.1.

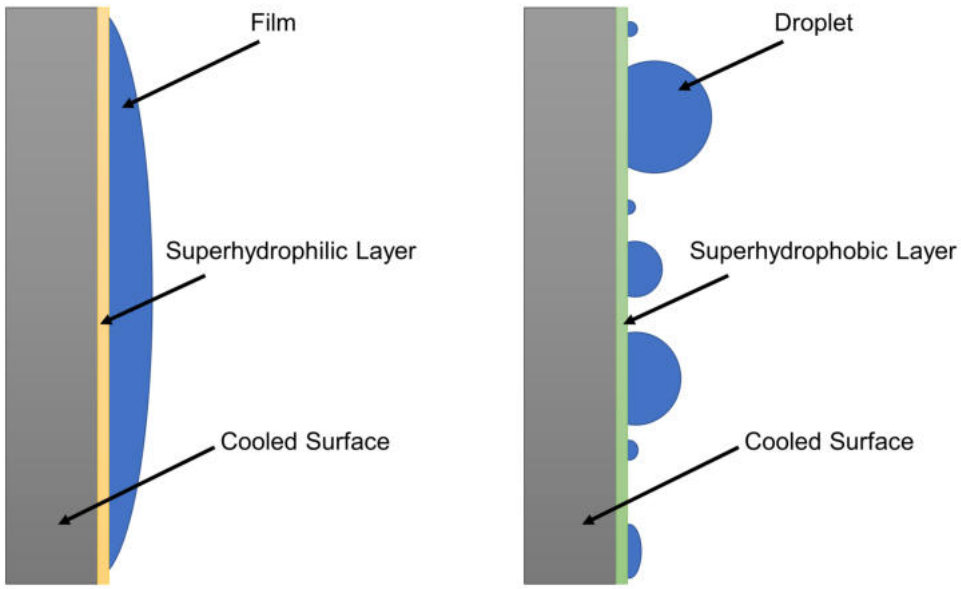

Figure 1.1: Scheme of FWC (l) and DWC (r).

Surface wettability is typically classified into four categories based on the static contact angle and the contact angle hysteresis. Superhydrophobic surfaces exhibit extreme water repellency, characterized by a contact angle greater than 150° and low contact angle hysteresis [20, 21]. Hydrophobic surfaces have contact angles ranging from 90° to 150°, while hydrophilic surfaces exhibit contact angles between 10° and 90°. Surfaces with contact angles below 10° are defined as superhydrophilic [22].

However, surface morphology plays a critical role in achieving superhydrophobic wetting behavior. Two principal wetting states have been identified: the heterogeneous Cassie-Baxter state and the homogeneous Wenzel state. In the Cassie-Baxter state, the liquid rests on a composite surface of solid and trapped air within surface roughness features, thereby minimizing solid-liquid contact. Conversely, the Wenzel state is characterized by the liquid fully penetrating and wetting the surface texture [23]. These distinct wetting mechanisms also influence the sliding dynamics of water droplets. In the Wenzel state, stronger adhesive interactions between the liquid and the surface lead to increased contact angle hysteresis, in contrast to the lower hysteresis observed in the Cassie-Baxter state. An illustration is displayed in Figure 1.2.

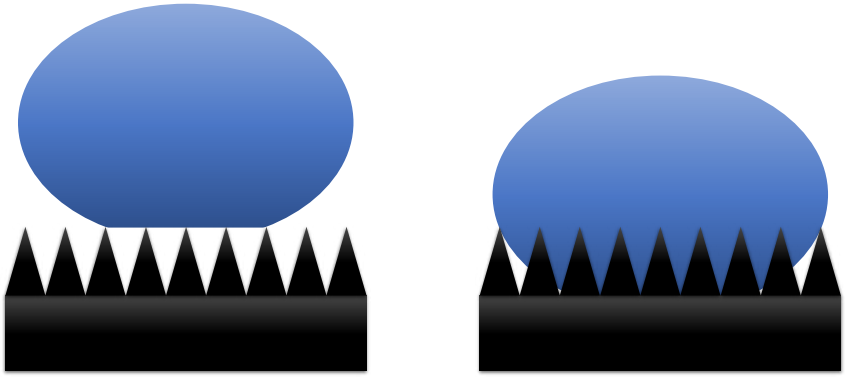

Figure 1.2: Scheme of the heterogeneous Cassie-Baxter (l) and the homogeneous Wenzel (r) wetting behavior.

An additional improvement in superhydrophobicity and droplet mobility can be achieved by introducing nanostructures on microstructured surfaces, resulting in so-called hierarchical structures. This improvement is primarily due to a further reduction in the effective wetted area, which enhances the Cassie-Baxter condition and minimizes liquid-solid contact [24]. This phenomenon is well-documented in nature and is commonly referred to as the lotus effect. The leaves of the lotus plant feature a hierarchical surface structure composed of micro- and nanoscale structures, overlaid with a hydrophobic wax layer exhibiting low surface energy. The combination of multiscale roughness and surface chemistry gives rise to exceptional superhydrophobicity, characterized by high water contact angles and minimal contact angle hysteresis [25–27].

The functionalization of thermoplastic polymer surfaces to achieve hydrophobic or superhydrophobic properties has gained considerable attention due to its potential in enhancing condensation heat transfer and surface durability. Among the various techniques, thermal imprinting has emerged as a particularly promising approach for superhydrophobization. Berendsen et al. [28] developed an injection molding process in which polystyrene (PS) and poly(methyl methacrylate) (PMMA) were embossed using a nickel mold fabricated via direct laser writing lithography followed by nickel electroplating. This method yielded contact angles up to 167° and contact angle hysteresis below 5°. Lin et al. [29] employed commercial sandpaper with varying roughness levels to imprint arbitrary microstructures onto polymer surfaces, achieving high contact angles but exhibiting poor droplet mobility due to elevated hysteresis.

A two-step fabrication method combining nanoimprinting and plasma etching was introduced by Durret et al. [30] for creating hierarchical structures on fluorinated ethylene propylene (FEP), poly(ethylene terephthalate) (PET), and PMMA. This approach successfully produced superhydrophobic surfaces with enhanced wetting resistance. In another study, Zhan et al. [31] demonstrated a single-step thermal embossing process for polypropylene (PP) using a titanium mold structured via femtosecond laser processing. The resulting hierarchical surface structures exhibited robust mechanical stability, maintaining contact angles above 150° and

contact angle hysteresis between 4° and 7° even after more than 100 cycles of sandpaper abrasion.

Despite the effectiveness of these approaches, a common limitation lies in the stochastic nature of the hierarchical structuring, which often lacks precise control over feature orientation and uniformity. Improved alignment and deterministic patterning of surface features could further enhance hydrophobic performance and extend the functional durability of the modified polymer surfaces.

In chapter 2, the modification of the surface and thus the superhydrophobization of the graphite composites was investigated. Chapter 2 details a scalable thermal imprinting technique employing microstructured silicon (Si) wafers as molds for the hot embossing of thermally conductive polymer composites. This method is subsequently combined with a metal coating and a controlled nanostructuring step using a simple hot water treatment which is described in the literature by Saadi et al. [32]. This nanostructuring step is simple to reproduce and can be applied to a wide range of metals and alloys, making it particularly interesting for research purposes [32]. An overview of the different metals, alloys and their structures can be seen in Figure 1.3.

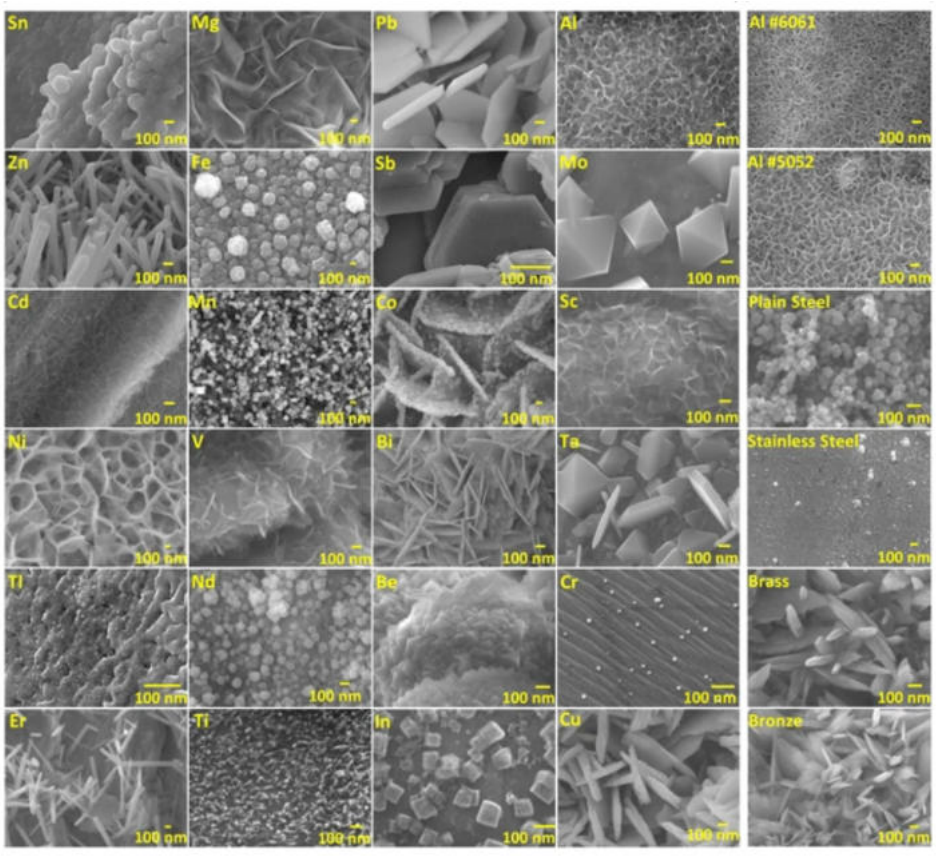

Figure 1.3: Top-view SEM images of various elemental metals and some alloys and metallic compounds after hot water treatment by Saadi et al. [32].

various metal oxides to fabricate hierarchically structured surfaces. The design schematics of the Si molds used in this study are illustrated in chapter 2.2. The thermal imprinting process allows for a broad range of microstructure geometries, with precise dimensional control enabled

through the fabrication of the Si molds. Representative imprints on graphite-filled polymer composites are provided in the Supporting Information. For industrial-scale implementation, mechanical replication methods such as roll-to-roll imprinting, which is described by Yi et al. [33], offer a more efficient and economically viable alternative.

However, the hot embossing process and Si wafers employed here were well-suited for laboratory-scale investigations. Following embossing, the microstructured samples were metallized via aluminum sputtering or copper electron beam evaporation, and subsequently nanostructured using a simple hot water treatment based on the approach reported by Saadi et al. [32]. This method enables precise tuning of the micro–nano interface by selecting different metals or metal alloys, each yielding distinct nanostructure morphologies.

Delicate aluminum nanostructures were compared with coarser, needle-like copper nanostructures, both with and without underlying microstructures, revealing significant morphological and functional differences. An example of the metal oxide nanostructures described can be seen in Figure 1.4.

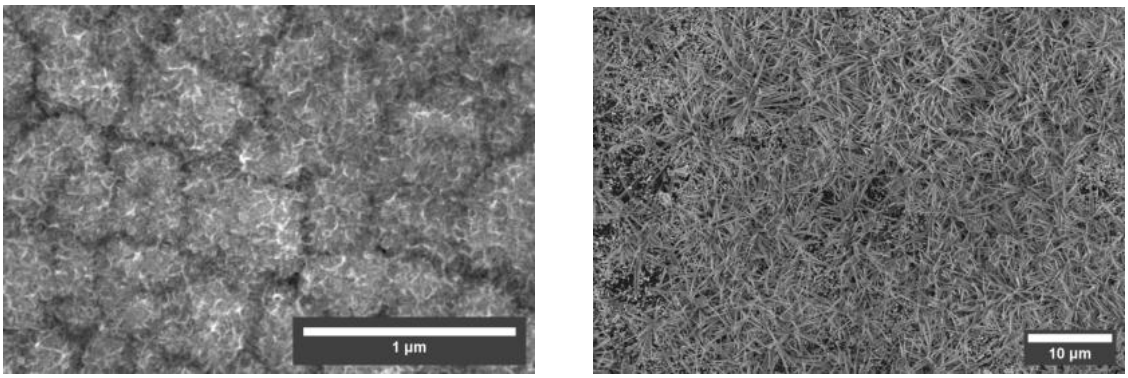

(a) Aluminium oxide nanostructures. **(b)** Copper oxide nanostructures.

Figure 1.4: Comparison of the top view SEM images with different magnifications of the two metal oxide nanostructures formed on the graphite composites

The combination of tailored microstructures and diverse nanostructures enables a wide design space for surface engineering. When further modified with stearic or lauric acid coatings, these hierarchical surfaces exhibit superhydrophobic properties, characterized by contact angles exceeding 160° and contact angle hysteresis below 5°. In contrast, uncoated hierarchical surfaces demonstrate near-complete wettability, with contact angles approaching 0°, indicative of superhydrophilic behavior.

This approach offers a rapid and versatile pathway for fabricating hierarchically structured thermoplastic composites with scalable microfeatures and tunable nanostructures. Surface functionalization to achieve superhydrophobic or superhydrophilic properties broadens the potential application spectrum of these materials in areas such as anti-fouling, self-cleaning, and enhanced heat transfer systems.

In chapter 3, the condensation behavior and heat transfer performance of humid air on thermally conductive graphite composites (GC) and stainless steel were systematically investigated. Stainless steel 1.4301 (X5CrNi18-10), a widely used material in conventional heat

exchanger applications, was selected as the reference. The performance of a modified graphite composite featuring superhydrophobic surface properties (SHGC) was evaluated against both the untreated GC and the stainless steel reference. The SHGC surface was fabricated by structuring the GC with copper oxide-based metal oxide nanostructures (MONSTRs) followed by a surface functionalization using lauric acid. This treatment resulted in a contact angle exceeding 170° and a contact angle hysteresis below 5°, providing ideal conditions for dropwise condensation (DWC). A comprehensive description of the materials and fabrication methods is provided in Raab et al. [34].

Experimental results indicated that, at lower relative humidities (RH) of $\varphi = 60\%$ and 80%, stainless steel exhibited higher heat fluxes. However, under saturated conditions ($\varphi = 100\%$), the heat flux densities were measured as 968 $W/m^2 \pm 3.5\%$ for stainless steel, 1320 $W/m^2 \pm 1.7\%$ for GC, and 1210 $W/m^2 \pm 2.3\%$ for SHGC. These findings demonstrate a substantial enhancement in heat transfer for GC and SHGC over stainless steel, with GC exhibiting a 36.4% higher heat flux. Corresponding heat transfer coefficients (HTCs) at 100% RH further supported this trend, with values of 134 $W/m^2K \pm 6.5\%$ for stainless steel, 309 $W/m^2K \pm 2.3\%$ for GC, and 244 $W/m^2K \pm 2.9\%$ for SHGC. The slightly lower performance of SHGC compared to GC is attributed to the Wenzel pinning effect and additional thermal resistances introduced by the nanostructures and hydrophobic coating.

Computational fluid dynamics (CFD) simulations corroborated the experimental findings, confirming laminar flow regimes and producing vapor-side HTC values in close agreement with experimental data, despite minor overestimations on the liquid side.

These results highlight the potential of graphite-based composites, particularly SHGC, to enhance condensation heat transfer. Nonetheless, further optimization of surface morphology and coating uniformity is necessary to fully leverage the benefits of superhydrophobic surface engineering in practical heat exchanger applications.

In chapter 4, the condensation of water from humid air on both an unprocessed and a structured, coated graphite composite in a condensation unit is investigated. The comparison of the two condensation behaviors can be observed in Figure 1.5.

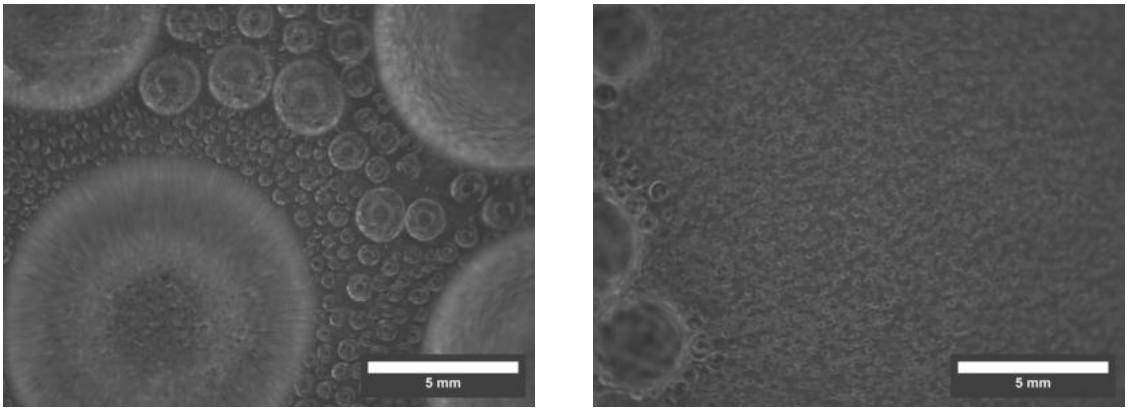

(a) Dropwise condensation after 12 h on unmodified graphite composite.

(b) Dropwise condensation after 12 h on modified, superhydrophobic graphite composite.

Figure 1.5: Comparison of the condensation behaviors of unmodified graphite composite and the modified, superhydrophobobic graphite composite.

The results were compared with the condensation behavior on polished stainless steel as a reference. The influence of the condensation behavior on the transferred heat flux is examined. Furthermore, the droplet size distribution on the unprocessed graphite composite is determined experimentally and additionally mapped using a model of the droplet size distribution from Wang et al. [35] and Tancon et al. [36]. This model is also used to predict the heat flux density during condensation.

2 Hierarchical Structured Superhydrophobic Surfaces on Graphite Composites

Contributor Roles Taxonomy

Raphael Raab: conceptualization; formal analysis; methodology; project administration; validation; visualization; writing - original draft; writing - review & editing

Chapter redrafted after the following main publication:

R. Raab, D. Fotachov, E. Oesterschulze, T. Melchior, E. von Harbou, and H.-J. Bart, "Hierarchical Structured Superhydrophobic Surfaces on Graphite Composites," *Applied Polymer Science*, vol. 142, no. 11, 2025. DOI: https://doi.org/10.1002/app.56598.

Abstract

A scalable thermal imprinting method and subsequent hierarchical structuring with metal oxide nanostructures forms superhydrophilic or superhydrophobic surfaces on graphite composites. Anisotropically etched silicon wafers serve as basis to create various microstructures by a thermal imprinting process on thermally conductive polymer graphite composites. Even after 32 times of embossing, the mold can be reused and restored by pyrolysis, ensuring its longevity and cost-effective process. Nanostructuring caused by sputtered aluminium or electron beam evaporated copper on the embossed microstructures and further oxidized with a simple hot water treatment offers a wide range of different hierarchical structures. The combination of microstructures and nanostructures with a low surface energy coating of stearic or lauric acid results in a superhydrophobic surface, which is completely water-repellent with a contact angle greater than 160° and low contact angle hysteresis lower than 5°. This work provides a deeper understanding of the effects of the interaction of aluminum and copper metal oxide nanostructures and thermally imprinted microstructures on surface of graphite compounds. It has been demonstrated that superhydrophobic surfaces can be created with both fatty acids. Lauric acid is easier to use due to its simple handling and reaches a maximum contact angle after 30 minutes of exposure time with copper oxide nanostructures of over 170°.

2.1 Introduction

Superhydrophobic surfaces are advanced materials characterized by their extreme water repellency, based on contact angles higher than 150° and a low contact angle hysteresis [37]. This unique property can be achieved through the combination of structured surfaces, with increased surface roughness, and a chemistry giving a low surface free energy [37, 38], which is inspired by natural models known as the lotus effect [39, 40]. Superhydrophobic surfaces have a wide range of applications and due to their high water-repellent effect, they remain dry and clean [41, 42]. They are used for self-cleaning textiles [43], anti-icing coatings [44, 45], oil-water separation technologies [46], water harvesting [47–49], heat transfer enhancement [16, 50, 51], and seawater desalination [52].

The surface structure has a significant influence on the wetting behavior. When investigating the wetting mechanisms, a distinction is made between two states: the heterogeneous Cassie-Baxter state and the homogeneous Wenzel state as depicted in Figure 2.1. The Cassie-Baxter state is characterized by the liquid being supported by air pockets within the surface roughness. Conversely, the Wenzel state involves the liquid fully penetrating the surface structure. The variation in surface wetting is also evident in the sliding behavior of water droplets which markedly improves heat transfer in falling films [53, 54]. In the Wenzel state, the adhesive forces between the water and the surface are significantly higher, resulting in considerably greater contact angle hysteresis compared to the Cassie-Baxter state [55]. A further improvement in superhydrophobization and sliding behavior [56] can be seen when the microstructured surface is covered with nanostructures and form so-called hierarchical structures, which is also due to a reduced wetted area [39]. There are a variety of methods that are used to create hierarchical structures, e.g. direct laser writing [57], soft-lithographic imprinting [58], electron-beam lithography [59], deep reactive ion etching [60], chemical etching [61], deposition [62], two-photon polymerization [63] and so on.

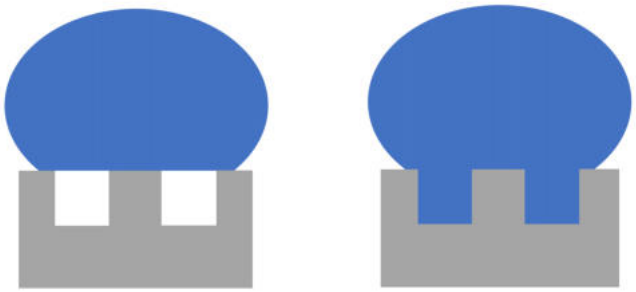

Figure 2.1: Scheme of Cassie-Baxter (l) and Wenzel (r) wetting behavior.

However, when it comes to the superhydrophobization of thermoplastic polymers, the process of thermal imprinting has aroused the interest of researchers. Berendsen et al. [28] introduced an injection molding process in which polystyrene (PS) and poly(methyl methacrylate) (PMMA) were embossed with a nickel stamp, which was produced by direct laser writing lithography and subsequent nickel plating resulting in contact angles of 167° and a contact angle hysteresis of less than 5°. Lin et al. [29] used commercial sand paper with different

roughnesses to create arbitrarily structured polymer coatings with comparatively high contact angles but poor sliding behavior. A two-step approach for hierarchical structures on fluorinated ethylene propylene (FEP), poly(ethylene terephthalate) (PET) and PMMA is presented by Durret et al. [30] with nanoimprinting and plasma roughening to achieve superhydrophobic properties. Zhan et al. [31] introduced a one-step thermal embossing method to form hierarchical structures on polypropylene (PP) with a titanium mold produced by femtosecond laser processing. The modified PP is resistant to rough cleaning and mechanical abrasion, which retained a contact angle of over 150° and a contact angle hysteresis of 4-7° even after over 100 cycles of sandpaper abrasion. When comparing these methods it is noticeable that the hierarchical structuring is always arbitrary and cannot be influenced precisely. A more precise alignment and arrangement of the structures would result in an enhanced hydrophobic behavior and longer a durability.

This work presents a scalable thermal imprinting technique with microstructured silicon (Si) wafers, which serve as a mold during the embossing process, and a subsequent, precise nanostructuring with various metal oxides creating hierarchically structured thermally conductive polymer composites. The scheme of the Si molds used for this scientific work are depicted in Figure 2.2. A wide variety of shapes of the microstructures are possible using the thermal imprinting process. The size of the structures can also be precisely controlled by the production of the Si molds, diverse imprints of the graphite composite can be seen in the Supporting Information. For industrial application, a mechanical production, e.g. a roll-to-roll imprinting process described by Yi et al. [33], of the microstructures would be suitable because it is much more efficient and economical. The hot embossing process used here and the silicon wafers produced were suitable on bench scale. The embossed microstructured samples were sputtered with aluminum or with electron beam evaporated copper and the nanostructures were created by a simple hot water treatment according to Saadi et al. [32]. Due to the wide variety of metal oxide nanostructures of different metals and their alloys, the microstructure-nanostructure relationship can be precisely adjusted. In this work, delicate aluminum nanostructures were compared to larger, needle-like copper nanostructures, which, based on their morphology alone, show significant differences, whether with or without microstructuring. The interplay of different forms of hot-stamped microstructures and the diverse morphology of the nanostructures opens up a multitude of possible combinations. This hierarchical structuring, combined with a coating of stearic or lauric acid, creates a superhydrophobic surface with a contact angle $> 160°$ and a low contact angle hysteresis $< 5°$. The hierarchically structured surface without low surface energy coating has perfect wetting characteristics and a contact angle that approaches 0°. This is a simple and fast approach to produce various hierarchically structured thermoplastic polymer composites with scalable microstructures and a wide range of possibilities to create diverse nanostructures when using different metals or alloys. A surface treatment in order to generate superhydrophilic or superhydrophobic surface properties expands potential applications.

2.2 Experimental Section

2.2.1 Materials

Thermally conductive graphite-polymer composites, containing 80 wt.-% graphite particles and polypropylene as the matrix, were manufactured by the Hydrogen and Fuel Cell Center (Duisburg) with a thickness of 1.6 mm. More information about these polymer composites can be found in Kiepfer et al. [13].

Anisotropically etched silicon (Si) wafers were produced for thermal imprinting. The production of similarly prepared silicon wafers is given by Fotachov et al. [64]. The silicon wafers were used as molds in the embossing experiments. A schematic of the 3D topography of the etched Si wafers is shown in Figure 2.2. The wafer dimensions L_W are 30 x 30 mm², the height H of the microstructures is approximately 20 µm, and the width W of the etched structures ranges from 60 µm to 120 µm in 20 µm intervals.

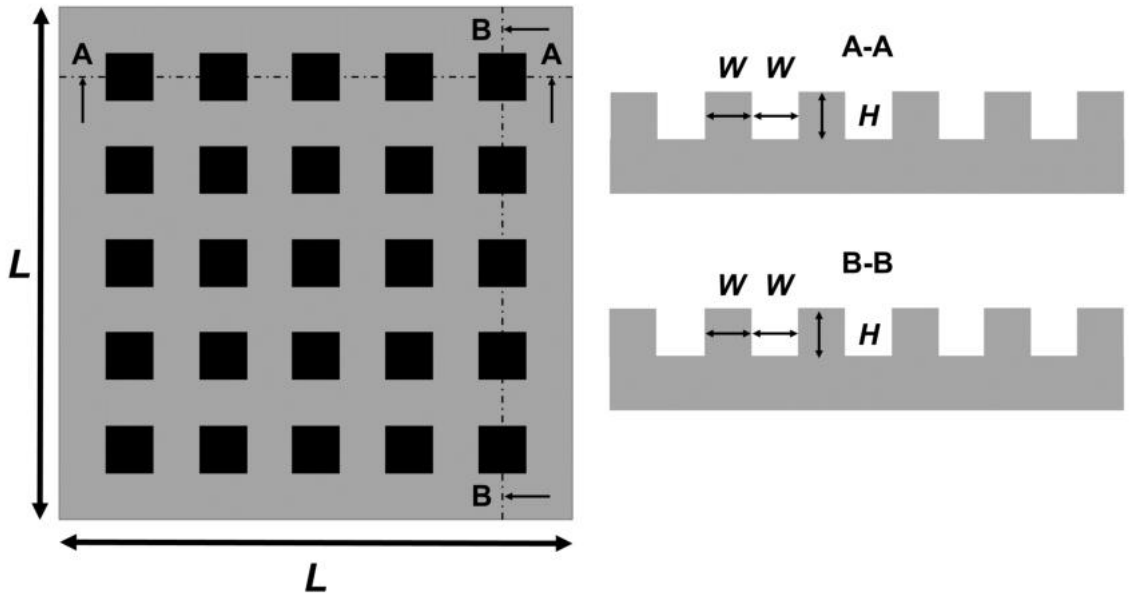

Figure 2.2: Scheme of the Si molds showing top view (l) and profiles (r).

2.2.2 Preparation of the Superhydrophobic Surface

To fabricate the superhydrophobic surfaces, four subsequent steps are carried out. Prior to this, the graphite polymer compound was cut into square samples of 50 x 50 mm² and then cleaned in an ultrasonic bath in acetone, isopropanol and deionized (DI) water for 10 min each. The SI wafers have the same cleaning steps. All chemicals used in the experiments were analytical grade reagents and were used as received.

Thermal imprinting

A TA.XTplus texture analyzer (Stable Micro Systems, England) was used for the thermal imprinting of the microstructures. The device is typically designed for tensile and compression

tests. An embossing die was developed to make the machine suitable for thermal imprinting. A conventional 50 W 12 V heating cartridge from a 3D printer was inserted into the embossing stamp so that the die can be tempered accordingly. The temperature is regulated via the current and voltage of a connected laboratory power supply unit. The temperature is measured inside the tip of the embossing die by a NiCr-Ni type K thermocouple (Ahlborn, Germany). The scheme of the thermal imprinting setup can be seen in Figure 2.3.

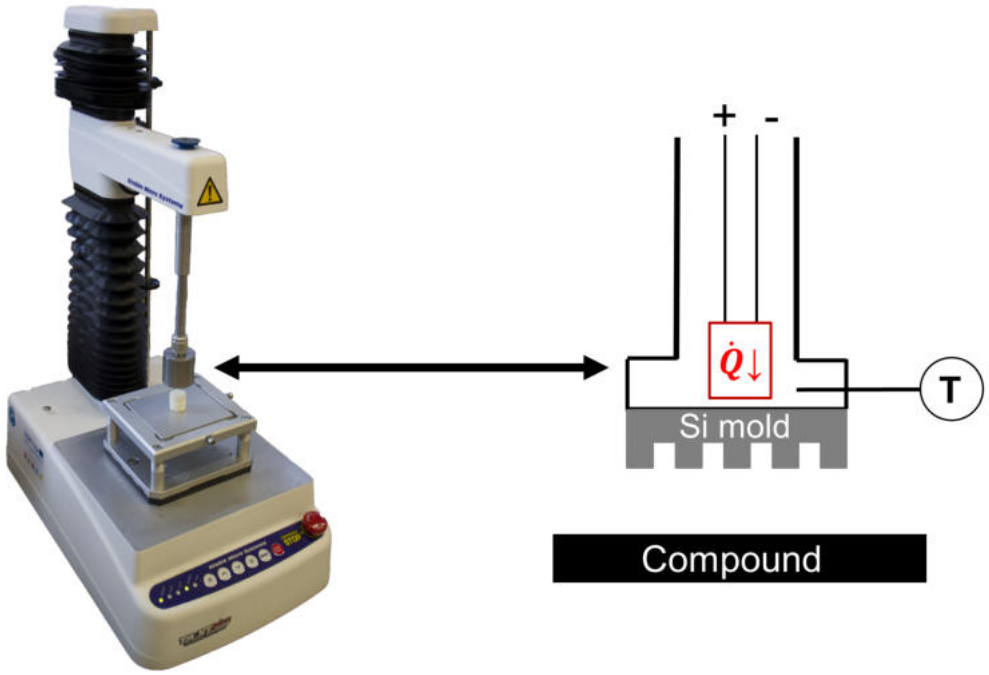

Figure 2.3: Image (l) and scheme (r) of the set-up of the thermal imprinting experiments.

The silicon wafer is attached to the die with a double-sided adhesive thermal pad and the die is then screwed to the arm of the Texture Analyzer A.XTplus. The maximum current of 2.5 A is set on the laboratory power supply. Meanwhile, the graphite composite sample is placed on the sample table under the die. After a temperature of 230°C has been reached, the experiment is started. The die is driven towards the sample and exerts a force of 450 N, which corresponds to a pressure of 0.5 MPa, on the sample over a period of 360 s. A temperature higher than the melting temperature of polypropylene is deliberately set because the sample is at room temperature before the compression and the test stand is not thermally insulated from the environment. The temperature drops to 115°C a few seconds after the start of the compression test. The pressure of 450 N and the high temperature at the stamp base ensure that the graphite composite reaches the glass temperature and that the wafer can penetrate into the sample at the beginning of the test before the temperature drops. This allows the negative of the silicon mold to displace the graphite composite and the desired microstructures are imprinted on the surface.

Metal coating

To form the metal oxide nanostructures (MONSTRs) on the surface, it is necessary to coat the graphite compounds with a layer of metal. The metal coating can be deposited using e.g. sputtering or electron beam evaporation. An aluminum layer was deposited on the samples with a sputtering system (Oerlikon UNIVEX 450 C, Leybold, Germany). The samples were sputtered with argon plasma at 300 W and a gas flow of 30 sccm for 15 min, resulting in an aluminum layer of 200 nm. Copper was also applied via sputtering at the same conditions. In order to be able to compare the surface quality of the coating method, the copper layer was also applied by electroplating and electron beam evaporation. For electron beam evaporation (Classic 500 L, Pfeiffer, Germany) the samples were coated at 300 W for 12:30 min resulting in a copper layer of 200 nm.

Nanostructuring

The MONSTRs were processed according to Saadi et al. [32]. The metal layer was oxidized within a simple hot water bath. A beaker with deionized water (DI) was placed in a thermostat (Alpha RA 8, Lauda, Germany). The aluminum coated samples were immersed in the hot water bath for 15 minutes at a temperature of 75°C and the copper coated samples were immersed in the hot water bath for 48 h at a temperature of 75°C. The temperature was measured with a NiCr-Ni type K thermocouple (Ahlborn, Germany). In addition, compressed air was injected at the bottom of the beaker throughout the oxidation, which ensured better mixing of the DI water in terms of the temperature gradient and a saturation with oxygen in the liquid. To reduce the long oxidation time of the copper surface, the surface can also be treated with a mixture of 2 M sodium hydroxide solution (NaOH) and 0.1 M potassium peroxodisulphate ($K_2S_2O_8$) for 10 min at room temperature as described by Bethke et al. [65]. The success of the copper nanostructures can be visually tracked, as the copper surface turns deep black due to the structuring, similar to black silicon. After oxidation the nanostructured samples are rinsed in a DI water bath to remove contaminants. They are dried at room temperature for 24 h.

Low surface energy coating

As a final step, a low surface energy coating was added in the MONSTRs processing. To investigate the influence of the chain length of the low surface energy coating two different fatty acids, lauric acid (Fisher Scientific, Germany) stearic acid (Omnilab, Germany), were used for this purpose. According to Lotz [66] a stearic acid coating was applied using a supersaturated solution of 2 wt.-% (48 mmol/L) stearic acid in heptane at 50°C for 10 min. Excess fatty acid was rinsed off with heptane after the coating at 50°C. Lauric acid was dissolved in ethanol according to Bethke et al. [65]. The influence of the lauric acid concentration and exposure time of the lauric acid bath was also investigated. Three lauric acids concentrations were prepared with 5 mmol/L, 10 mmol/L and 20 mmol/L. The static and dynamic contact angle was measured every 15 min for 1 h and after 24 h to see how the wetting behavior and the lauric acid coating changes over time.

2.2.3 Surface Characterization

For cross-section measurements, 3D topographic and surface roughness, a laser confocal microscope (µSurf Explorer, NanoFocus, Germany) was used. The evaluation of the confocal microscope images was carried out with the program MountainMaps. For a more detailed view of the micro- and nanostructures of the hierarchically structured polymer compound, scanning electron microscope (SEM, SU8000, Hitachi, Japan) images were taken with an accelerating voltage of 5 kV. The static and dynamic contact angle measurements were performed with an optical contact angle goniometer (OCA 15EC, DataPhysics, Germany). The fluid used for the contact angle measurement was DI water and the volume of a drop was 8 µl. For dynamic contact angle measurements the needle-in method was used. An 8 µl DI water droplet was placed on the surface, and the needle was inserted into the droplet. The machine then pumped 40 µl into the drop to measure the advancing contact angle and subsequently pumped 40 µl out of the drop to measure the receding contact angle. The difference between the advancing and receding contact angles is the contact angle hysteresis. The values of the contact angle measurements were automatically obtained using the SCA20 software from DataPhysics. The high-speed camera (IDT OS8, Imaging Solutions, Germany) recordings were performed at 4000 fps, using a high-performance LED light source (IDT/ Veritas Constellation 120E, Imaging Solutions, Germany). The droplet that fell onto the surface was produced with a 500 µL Hamilton syringe, which is also used for contact angle measurements.

2.3 Results and Discussion

2.3.1 Surface Morphology of the Imprinting Experiments

The 3D surface profile of the Si wafer, depicted in Figure 2.4, and the top-view scanning electron microscope (SEM) images in Figure 2.5 provide a comprehensive view of the wafer surface characteristics. These figures reveal that the surface exhibits a smooth, angular microstructured morphology, characterized by well-defined edges and periodic patterns. The cross-section measurement of the example of the 60 µm Si mold in Figure 2.4 b) illustrates a height of approximately 19 µm of the etched structures and highlights the perpendicularity of the sharp edges. All confocal microscope images and cross-section measurements of the other Si molds can be found in the Supplementary Information.

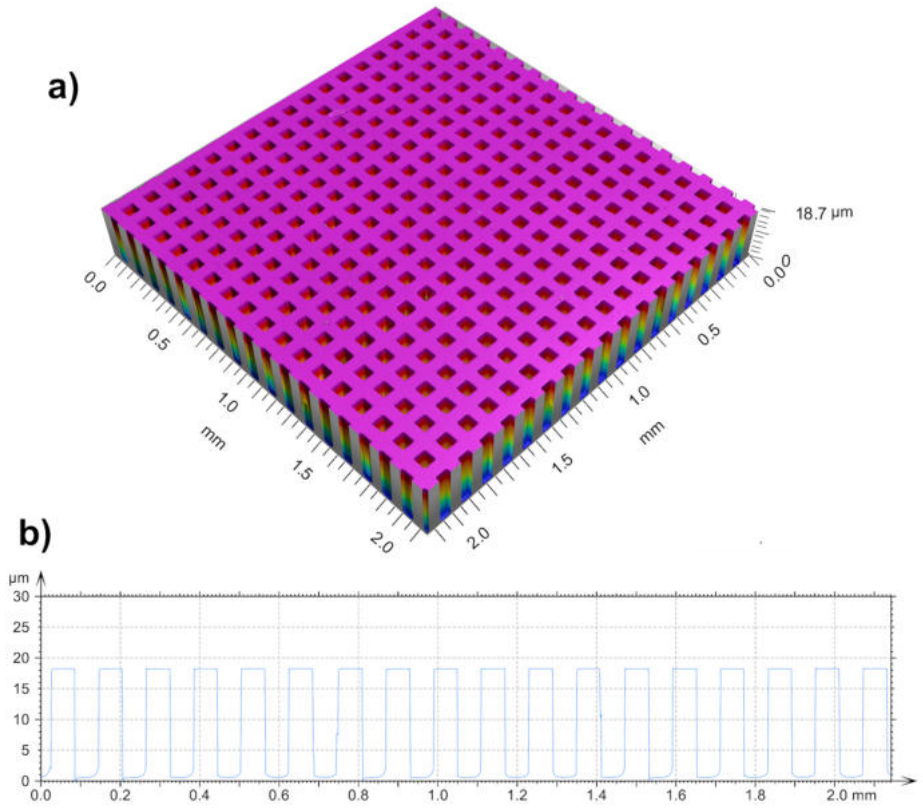

Figure 2.4: a) 3D profile of the silicon wafer captured by a confocal microscope and b) cross-section measurement showing the height of the 60 µm structured Si wafer.

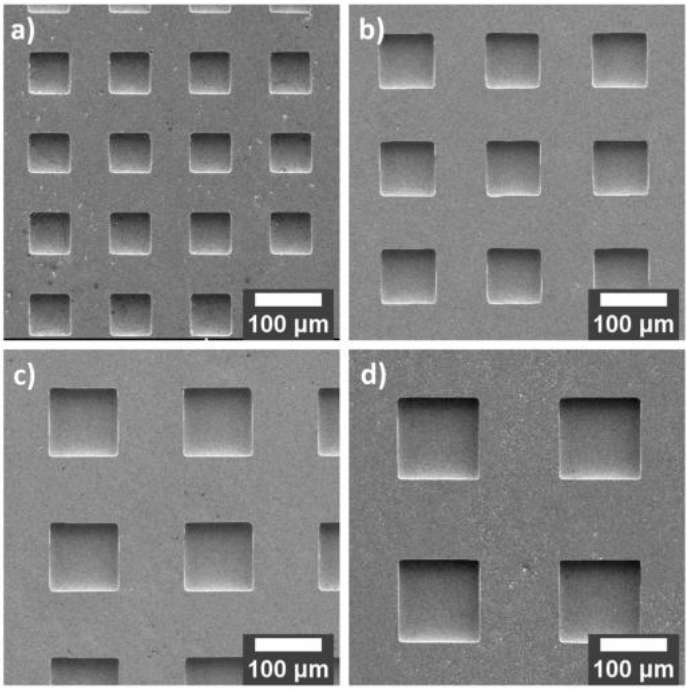

Figure 2.5: Top view SEM images of the Si wafers with a) 60 µm, b) 80 µm, c) 100 µm and d) 120 µm etched structures.

The 3D topography and a SEM image of the untreated compound are presented in Figure 2.7.

These images reveal that the surface of the unembossed compound exhibits a high degree of roughness, indicating significant textural variations. The measured mean arithmetic roughness S_a of the compound is 2.0 µm, which is more than 20 times higher compared to stainless steel 1.4571 [13]. However, it must be taken into account that the manufacturing methods and the different forms of graphite particles, their particle size distribution and the different types of PP have a considerable influence on the surface properties of the composite and the mean arithmetic roughness S_a [13].

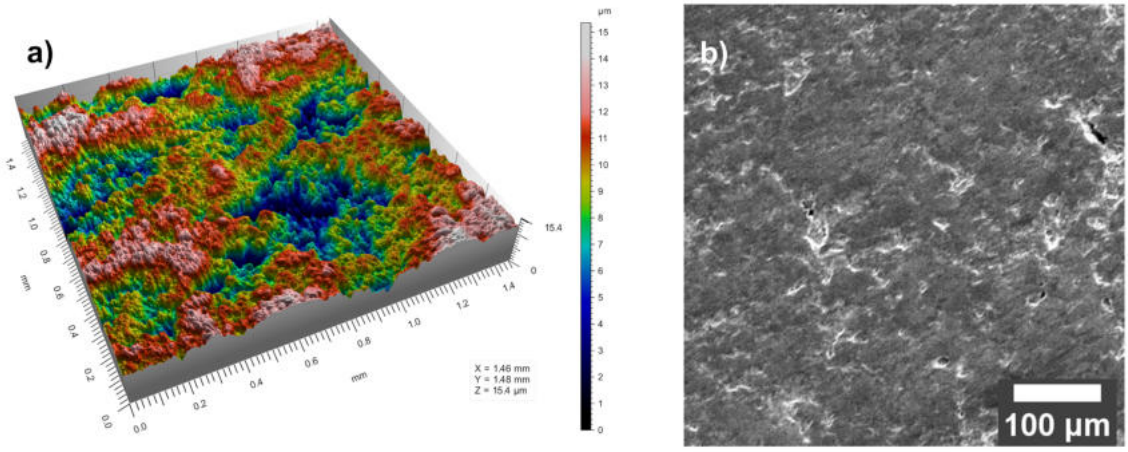

Figure 2.6: a) 3D profile by a confocal microscope and b) top view SEM image of the untreated graphite compound.

As the hot embossing machine lacks an adiabatic chamber and the samples were not preheated, the temperature decreased to approximately 100 °C due to heat conduction over the imprinting time of 360 s. After thermal imprinting, the Si wafer can be easily demolded after cooling without damaging the fragile mold, even though no additives such as lubricants or fatty acids were used for surface treatment of the imprinting matrices compared to the literature [31]. The results of the surface structures of the embossed compounds are shown in Figure 2.7. The surface of the imprinted composites replicates the negative structures of the Si wafer molds, resulting in periodic columnar structures with a height H of approx. 20 µm. The 3D profiles and cross-sectional measurements indicate that larger structures have more rectangular and sharper edges. However, it is demonstrated that 60 µm structures can also be successfully imprinted onto the polymer composites and easily be demolded without additives. As the structures become smaller, more defects and broken spots appear, caused by the significant interlocking of the microstructures during hot embossing. Nevertheless, no missing columns were observed, and the height profile shows an almost rectangular shape up to 60 µm. Comparing the SEM and confocal microscope images of untreated sample shown in Figure 2.6 to the imprinted samples, the embossing process creates a smoother surface and seals imperfections such as microcracks or holes.

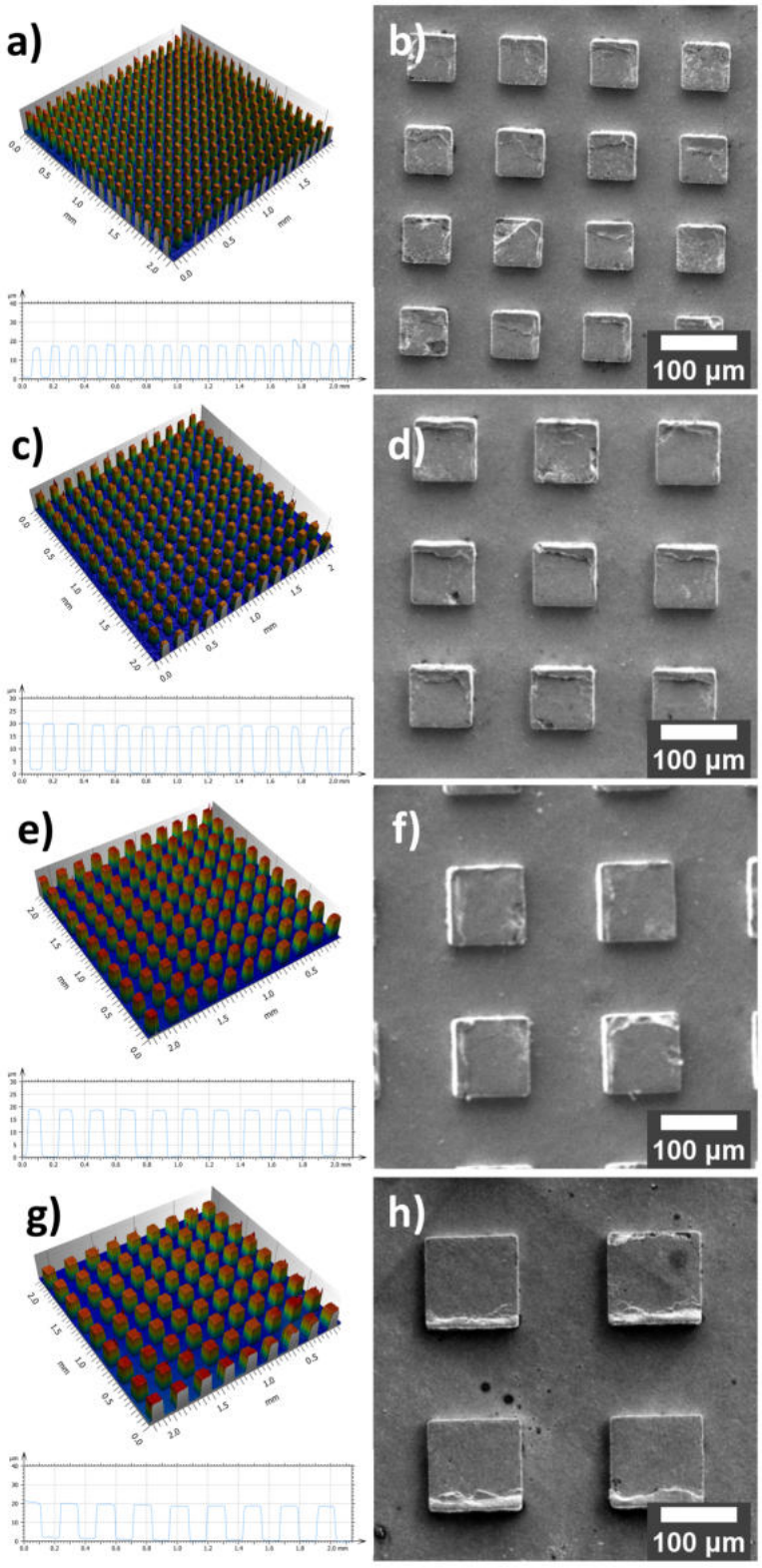

Figure 2.7: 3D profiles of imprinted compounds captured by a confocal microscope for a) 60 µm, c) 80 µm, e) 100 µm, g) 120 µm columns and top view SEM images for for b) 60 µm, d) 80 µm, f) 100 µm, h) 120 µm columns.

2.3.2 Wetting Behavior of the Microstructures

To characterize the wetting behavior of the surface, static and dynamic contact angle measurements were performed, as shown in Figure 2.8. To ensure good reproducibility of the imprinting process, each surface texture was embossed at least twice. The 3D profiles and cross-section measurements of all surfaces are provided in the Supplementary Information. The static contact angle increases from about 97° on the untreated sample to about 140° on the embossed samples, indicating improved hydrophobicity of the surface. However, the dynamic contact angle measurements show large contact angle hysteresis with significant error bars, indicating poor sliding behavior. The contact angle hysteresis of the untreated sample is the lowest, with an average hysteresis of 39°. All embossed compounds exhibit a larger contact angle hysteresis of more than 60°, which suggests a decrease in hydrophobic surface properties. The large error bars can be attributed to the pinning of the droplets to the surface. If the droplets remain in the Cassie-Baxter state during dynamic measurements, the contact angle hysteresis is low, at approximately 15-20°. If the droplets penetrate the structures and transition from the Cassie-Baxter state to the Wenzel state, they adhere strongly, resulting in large contact angle hysteresis of over 80°.

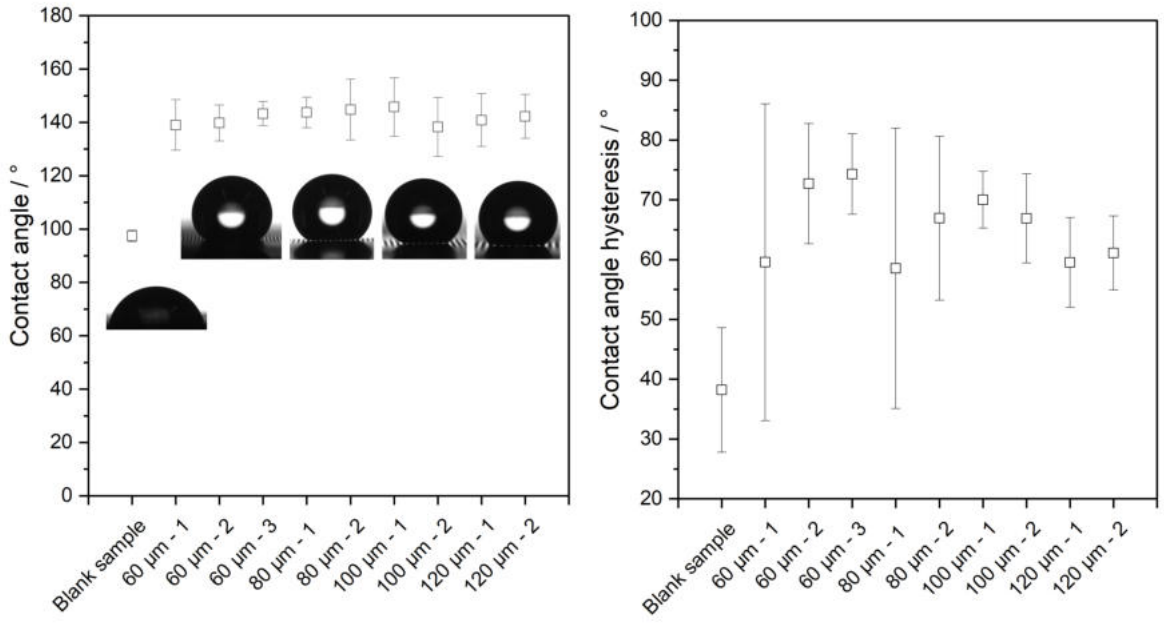

Figure 2.8: Static and dynamic contact angle measurements of the thermally imprinted and the blank compound.

2.3.3 Hierarchical Structuring and Superhydrophobic Wetting Behavior

To obtain a completely superhydrophobic surface, nanostructures were applied to the existing microstructure, creating a hierarchical structure. A simple approach to generate nanostructures is demonstrated by Saadi et al. [32]. Various metals and alloys can be nanostructured through an oxidation step using a hot water bath. During oxidation, the metal oxides self-assemble into nanostructures, forming what are known as metal oxide nanostructures (MON-

STRs). Since the wetting behavior of the embossed column structures showed no significant differences in the static and dynamic contact angle, the smallest embossments of 60 µm columns were used for the hierarchical structuring. The samples were coated with metal by sputtering aluminum or electron beam evaporated copper. Both coating processes resulted in a 200 nm thick metal layer. In order to investigate the impact of hierarchical structuring, embossed and unembossed composites were coated and later oxidized according to the method described by Saadi et al. [32]. Figure 2.9 illustrates the metal layers before and after oxidation. A comparison of the metal coatings reveals that the sputtered aluminum in Figure 2.9 a) has a rougher grain than the electron beam evaporated copper in Figure 2.9 b). The resulting MONSTRs of aluminum in Figure 2.9 c) and copper in Figure 2.9 d) are quite different and similar to literature findings [32]. It is also noticeable that the aluminum MONSTRs are finer and smaller than the copper MONSTRs and show a specific pattern of a just few nanometers, while the copper nanostructures form needle-like, non-directional columns of about 100-200 nm in diameter and a couple of micrometers in length. Furthermore, it can be added that there is no change in the morphology of the copper nanostructures whether they are oxidized for 48 h after Saadi et al. [32] in a hot water bath at 75 °C or oxidized for 10 min with a mixture of 2 M NaOH and 0.1 M $K_2S_2O_8$ at room temperature.

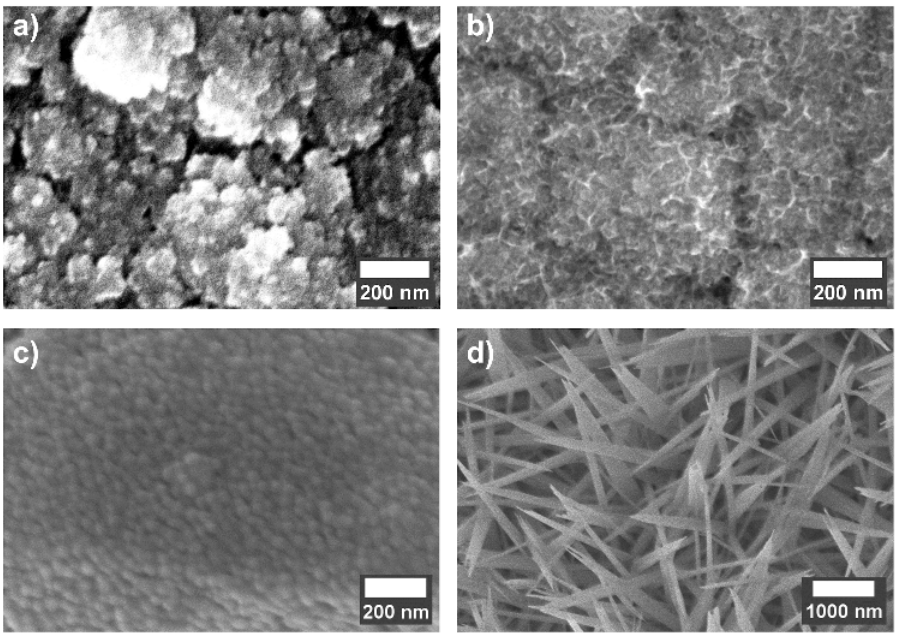

Figure 2.9: Top view SEM images of a) sputtered aluminum b) aluminum oxide nanostructures c) electron beam evaporated copper and d) copper oxide nanostructures.

The hierarchical structuring and the high surface energy of the MONSTRs result in a superhydrophilic surface with perfect wetting behavior, where the contact angle approaches 0° and cannot be measured. This phenomenon is depicted in the the Supplementary Information. To achieve a superhydrophobic surface, a coating with low surface energy is required. Two different fatty acids, lauric acid and stearic acid, which differ only in the length of the carbon body, are investigated. Lauric acid has a C12 body and stearic acid has a C18 chain. According to Lotz [66], stearic acid is dissolved in a supersaturated solution with 2 wt.-% (48 mmol/L)

heptane. The same practice was used for lauric acid to compare the results. The supersaturated solution of stearic acid is only homogeneous above 50 °C and has a white fatty acid precipitate at room temperature. If you compare the two low surface energy substances with each other, it is seen that there is no difference in terms of the wetting and sliding behavior of the surfaces according to the coating with heptane at 50°C and a supersaturated solution for 10 min. However, it has a major influence whether the aluminum nanostructures are hierarchically structured or whether the aluminum MONSTRs are applied directly to the graphite composite without embossed microstructures. The hierarchical structuring with aluminum oxide has a contact angle of approximately 160°+-2° and a contact angle hysteresis of less than 10°. The pure nanostructuring of aluminum oxide compared to hierarchical structuring has a contact angle of 90° and a contact angle hysteresis of 38°+-5°, which does not indicate any superhydrophobic surface behavior. In the case of copper MONSTRs, the hierarchical structuring has no apparent influence on the wetting behavior, since both forms exhibit superhydrophobic surface behavior with a contact angle of greater than 170° +-1° and contact angle hysteresis of less than 5° +-1°. In most cases, no contact angle hysteresis could be measured using the needle-in method because the drop either rolled away when it was placed on the surface or when the needle was inserted into the drop. The static contact angle measurements are depicted in Figure 2.10.

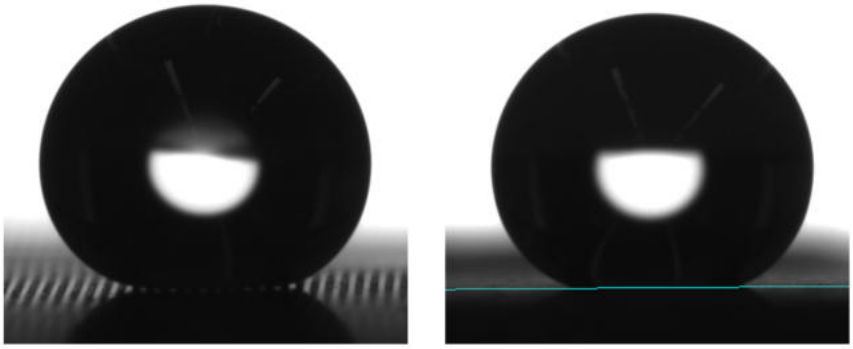

Figure 2.10: Static contact angle measurement of the hierarchically structured aluminum surface (l) and the copper nanostructures (r) both coated with stearic acid.

The C12 body of lauric acid dissolves better, e.g. also in ethanol and is homogeneous at room temperature. Due to these advantages and the easy handling three different solutions with 5 mmol/L, 10 mmol/L and 20 mmol/L lauric acid in ethanol were prepared to examine the impact of the concentration and the exposure time of the fatty acid for the copper oxide nanostructures. The fine aluminum nanostructures rapidly clog with the waxy fatty acids, which is why the experiments for exposure time and concentration of lauric acid were only carried out for the copper MONSTRs. Due to the long needle-like structures of 100-200 nm in diameter and a few µm in length, no differences were found whether the graphite composites were previously embossed or not. This can be explained by the fact that the copper oxide nanostructures already form a hierarchical structure by nature and thus the wettable area is not reduced as compared to the aluminum nanostructures, which require embossing of the graphite composites to get superhydrophobic behavior. The impact of the lauric acid concentration and

the exposure time can be seen in Figure 2.11. The highest concentration of 20 mmol/L has the highest contact angle after 15 min and reaches its maximum of approx. 179.8° after 30 min, after 30 min the contact angle decreases to 147° after 24 h. Similar behavior can be seen for the other concentrations. Their maximum lies always between 30 to 60 min and decreases after 24 h. The decrease in the contact angles after 24 hours can be explained by the fact that the lauric acid overgrows the copper nanostructures and only a few needle-like oxides still protrude from the wax layer. This can be confirmed by the top-view SEM recordings depicted in the Supporting Information as it shows a continuous layer of lauric acid with only a few copper MONSTRs.

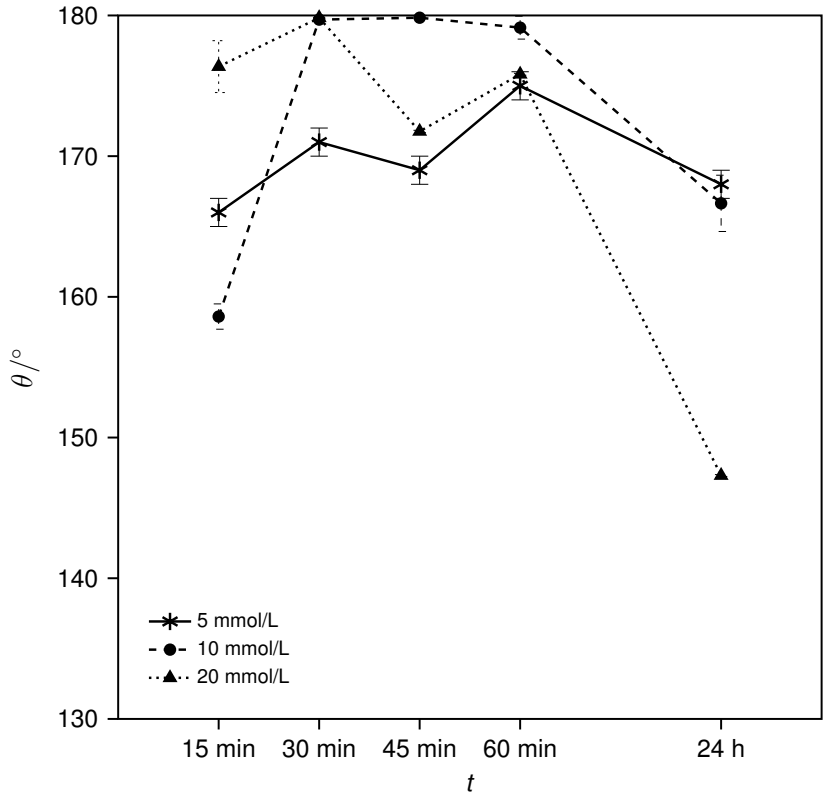

Figure 2.11: Impact on the static contact angle of the copper oxide nanostructures of the lauric acid concentration and exposure time.

To illustrate the superhydrophobic behavior a high-speed camera footage was captured at 4000 fps. In the footage, a water droplet of approximately 10 µl is seen falling onto the surface. Upon contact, the droplet is completely repelled and bounces off the surface without leaving any trace of wetting. This sequence of events highlights the surface's ability to repel water, and a series of selected frames from the footage is displayed in Figure. 2.12.

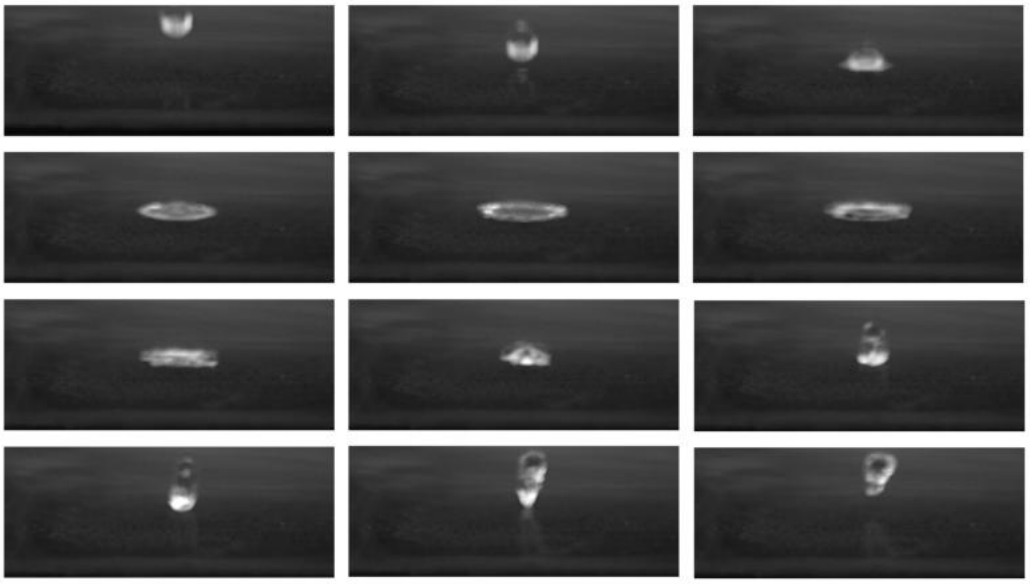

Figure 2.12: Series of high-speed camera recording at 4000 fps.

2.3.4 Restoration of the Embossing Molds

After repeated use the Si wafer used for thermal imprinting may accumulate graphite composite particles on its surface. To clean the wafers and ensure they can be reused without contamination, the wafers are subjected to pyrolysis, heating them to 500°C for half an hour. This process burns off the contaminant particles. The effectiveness of the cleaning process is demonstrated in Figure 2.13.

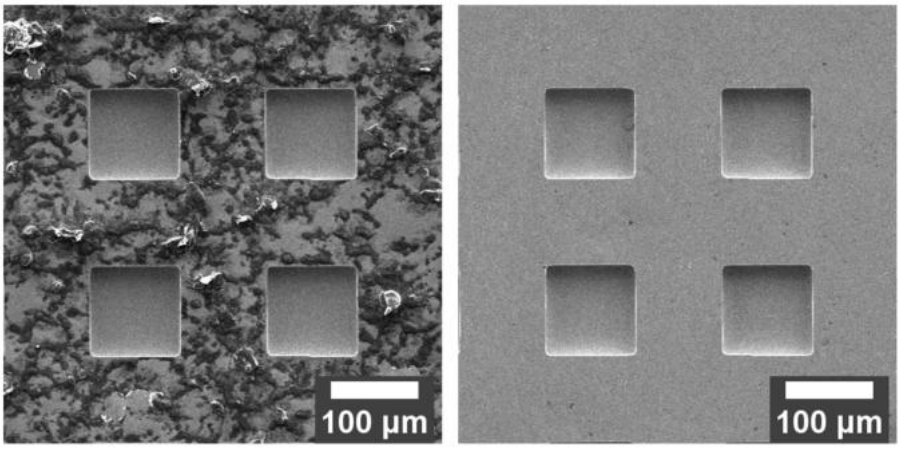

Figure 2.13: SEM images of the 100 µm Si mold -as an example- after 32 embossings (l) and restored by pyrolysis (r).

2.4 Conclusion and Outlook

This study successfully demonstrates a scalable method for fabricating superhydrophilic and superhydrophobic surfaces on thermally conductive polymer-graphite composites using ther-

mal imprinting and hierarchical structuring with metal oxide nanostructures (MONSTRs). The process involves the precise use of silicon wafers as molds, which can be repeatedly used and restored via pyrolysis, ensuring both longevity and cost-effectiveness. The combination of microstructured surfaces with additional nanostructuring and stearic acid or lauric acid coating achieved superhydrophobic properties, evidenced by a high static contact angle $>160°$ for the aluminum oxide nanostructures and $>170°$ for the copper oxide nanostructures and minimal contact angle hysteresis $<5°$. The aluminum structures require a previous microstructured embossing of the surface, whereas the copper structures exhibit superhydrophobic behavior despite the need for thermal imprinting of the surface. The dependence of the contact angle in relation to the fatty acid concentration and the exposure time was demonstrated. All concentrations reached their mamximum after 30 to 60 min with contact angles up to 180°. After an exposure time of 24 hours, the copper nanostructures were mostly covered by the fatty acid at all concentrations, which caused a decrease in the contact angle. The versatility of this technique opens up diverse applications in self-cleaning materials, anti-fouling coatings, and heat transfer systems, making it highly suitable for industrial implementation. The work highlights the potential of polymer composites in advanced material applications, particularly where surface properties are crucial.

3 Heat Transfer on Hierarchical Structured Graphite Composites

Contributor Roles Taxonomy

Raphael Raab: conceptualization; formal analysis; methodology; project administration; validation; visualization; writing - original draft; writing - review & editing

This chapter is submitted to a peer-reviewed journal for publication.

Abstract

This study investigates the wetting behavior, condensation dynamics, and heat transfer performance of stainless steel (SS), graphite composite (GC), and a modified superhydrophobic graphite composite (SHGC) under varying relative humidity (RH) conditions. Static and dynamic contact angle measurements revealed significant differences in wetting behavior, with SS demonstrating hydrophilic properties ($65° \pm 7°$), GC exhibiting hydrophobicity ($97° \pm 2°$), and SHGC achieving superhydrophobicity ($> 170°$). Condensation experiments at 100% RH showed that GC and SHGC outperformed SS in both heat flux densities and heat transfer coefficients (HTCs) at higher RH levels. At 100% RH, GC achieved the highest heat transfer coefficient of $309\,\mathrm{W/m^2K} \pm 2.3\%$, followed by SHGC $244\,\mathrm{W/m^2K} \pm 2.9\%$, while SS remained at $134\,\mathrm{W/m^2K} \pm 6.5\%$ compared to 60 % and 80 % RH. Computational fluid dynamics simulations confirmed the experimental findings, validating laminar flow and demonstrating strong agreement with measured vapor-side HTCs. The reduced performance of SHGC compared to GC is attributed to the Wenzel pinning effect and additional thermal resistances. These findings highlight the need for further optimization of surface structure and coating uniformity to enhance the condensation heat transfer performance of SHGC in practical applications.

3.1 Introduction

The condensation of water from humid air is of crucial importance for various technical applications, such as seawater desalination [67, 68], energy generation [69], air conditioning [70] and water harvesting [48, 71–73]. Condensation is a process in which a fluid changes from a gaseous to a liquid state. This process occurs, for example, when water vapor encounters a surface whose temperature is colder than the vapor's dew point and the vapor pressure of the gas rises above the saturation vapor pressure [74]. There are two different forms of condensation: filmwise condensation (FWC) and dropwise condensation (DWC). As early as a hundred years ago, Schmidt et al. [14] showed that DWC results in improved heat transfer compared to FWC. In the case of FWC, the condensate completely covers the heat-transferring surface. This layer of condensate acts as an additional thermal resistance. At DWC, the droplets cover a smaller surface area compared to FWC. As the droplets grow, they coalesce and detach from the surface with greater efficiency [48]. The wettability of the surface usually determines the condensation behavior, where hydrophobic surfaces favoring DWC and hydrophilic surfaces promoting FWC [50]. The two different forms of condensation are shown in Figure 3.1.

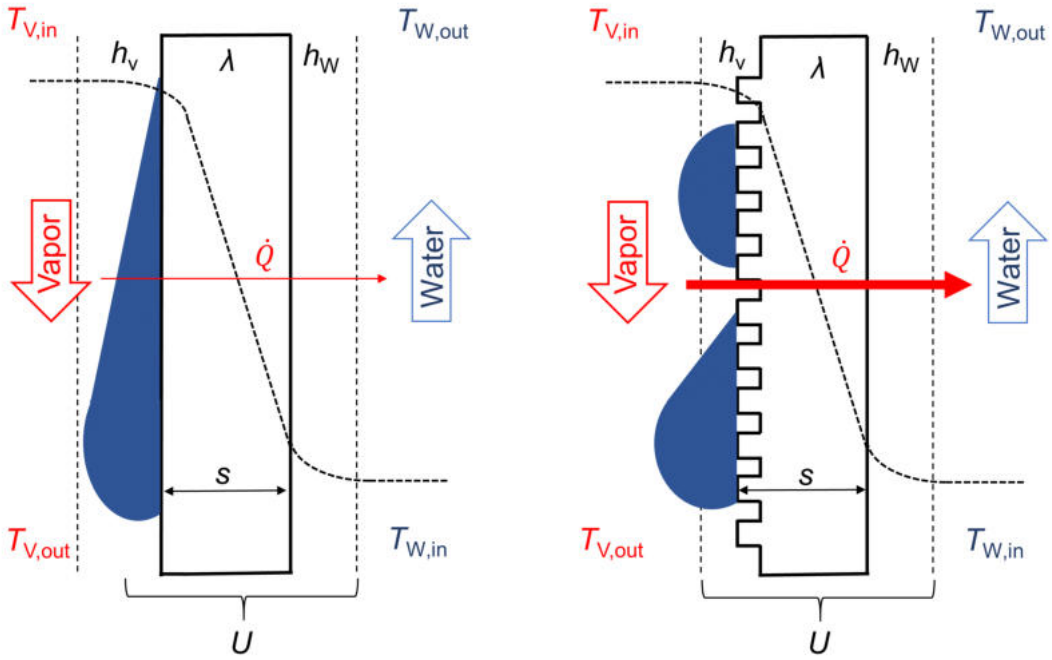

Figure 3.1: Scheme of FWC (l) and DWC (r).

Surface wettability is generally categorized into four different categories, which depend on the static contact angle (CA) Θ. Superhydrophobic surfaces (SHS) are characterized by their extreme water repellency, based on CA higher than 150° and a low contact angle hysteresis [37]. Hydrophobic surfaces have CA ranging between 90° to 150°. The CA of hydrophilic surfaces are between 10° to 90° and the CA of superhydrophilic surfaces are lower than 10° [50].

However, the surface structure has a significant influence when it comes to superhydrophobic wetting behavior. Examining the wetting mechanisms, two distinct states are identified: the

heterogeneous Cassie-Baxter state and the homogeneous Wenzel state. In the Cassie-Baxter state, the liquid is supported by air pockets within the surface roughness (s. Figure 3.1), preventing complete surface contact. In contrast, the Wenzel state involves the liquid fully wetting the surface texture. Differences in wetting behavior are also reflected in the sliding dynamics of water droplets, which notably enhance heat transfer in falling films [53, 54]. In the Wenzel state, the adhesive forces between the water and the surface are substantially higher, resulting in significantly greater contact angle hysteresis compared to the Cassie-Baxter state [55].

Furthermore, superhydrophobic surfaces are linked to the droplet pinning effect, where the drops adhere strongly in Wenzel states due to the complete wetting of the structured surface, preventing the droplets from sliding off [75, 76]. In general, a superhydrophobic surface requires two elements, a structured surface with an increased surface roughness and a surface chemistry with low free energy [37, 38]. To achieve this special combination, manufacturing steps such as structuring, e.g. with thermal imprinting [31] and additional coatings such as long-chain fatty acids [77] are required. Low surface energy coatings provide additional resistance to heat transfer and often have poor thermal conductivity [77]. For industrial use, the superhydrophobic surface properties must remain robust and stable over a long period of time in order to ensure economic efficiency. Even today, there are only a few areas of application for superhydrophobic surfaces in industrial use, and these are often only investigated under laboratory conditions [78]. It is therefore necessary to critically examine whether a surface modification of heat-transferring components is economically viable and robust for industry.

In this work, the condensation behavior and heat transfer of humid air on thermally conductive graphite composites and stainless steel are investigated. Stainless steel 1.4301 (X5CrNi18-10), commonly used in the production of conventional heat exchangers, is chosen as a reference material for this study. A modified graphite composite (GC) with superhydrophobic surface (SHGC) properties is compared to an untreated GC and the reference material. The SHGC is created by structuring the surface of the GC with metal oxide nanostructures (MONSTRs) made of copper oxide and a coating of lauric acid. The SHGC surface has a CA of over 170° and a CA hysteresis of under 5°, which are perfect conditions for DWC. A detailed description of the materials and the manufacturing process is presented in Raab et al. [34]. The experiments have shown that the heat flux of stainless steel is higher at lower relative humidities (RH) $\varphi = 60\%$ and 80%, but condensation experiments at 100% RH showed heat flux densities of $968\,\mathrm{W/m^2} \pm 3.5\%$ for SS, $1320\,\mathrm{W/m^2} \pm 1.7\%$ for GC, and $1210\,\mathrm{W/m^2} \pm 2.3\%$ for SHGC. These results confirm that GC and SHGC significantly outperform SS, with GC achieving a 36.4% higher heat flux than SS. The heat transfer coefficients (HTCs) at 100% RH similarly reflect this trend, with values of $134\,\mathrm{W/m^2K} \pm 6.5\%$ for SS, $309\,\mathrm{W/m^2K} \pm 2.3\%$ for GC, and $244\,\mathrm{W/m^2K} \pm 2.9\%$ for SHGC. SHGC is not superior to GC due to the Wenzel pinning effect and additional thermal resistances from the surface structures and coating. CFD simulations validated experimental data, confirming laminar flow conditions and providing comparable HTCs. Simulated and experimental results for the vapor-side HTC showed good agreement, despite slight overestimations on the water side.

These findings highlight the superior performance of GC and SHGC in promoting condensation

and heat transfer efficiency. However, further optimization of SHGC surface structure and coating uniformity is necessary to fully exploit its potential in practical applications.

3.2 Experimental Section

3.2.1 Materials

For the condensation experiments three different materials were examined. Stainless steel 1.4301 (X5CrNi18-10) was used as a reference material with a thickness of 1.5 mm and a thermal conductivity of 17 W/mK[79]. Thermally conductive graphite-polymer composites, containing 80 wt.-% graphite particles and polypropylene C143 as the matrix, were manufactured by the Zentrum für Brennstoffzellen-Technik (Duisburg) with a thickness of 1.6 mm. The GCs have a thermal conductivity λ of 1.58 W/mK, more information about these polymer composites can be found in Kiepfer et al. [13]. A surface-modified graphite composite with hierarchical, superhydrophobic coated copper oxide nanostructures and an untreated graphite composite were examined in order to provide information on the influence of the surface hydrophobicity and the additional surface coatings on the heat transfer and the condensate mass flow for drinking water generation. The superhydrophobic surfaces used were applied directly to the graphite composites without prior hot embossing. Lauric acid was used to coat the copper nanostructures. The explicit production and characterization of the surface is described in Raab et al. [34].

3.2.2 Experimental Setup

Wetting behavior

The wetting behavior was characterized with an optical contact angle goniometer (OCA 15EC, DataPhysics, Germany). Static and dynamic CA measurements were performed. The fluid used for the CA measurements was DI water and the volume of a drop was 8 µl. The dynamic CA measurements were performed with the needle-in method. Further information about the surface characterization can be found in Raab et al. [34]

Heat transfer measurements

To investigate the different materials and their condensation behavior, heat transfer measurements were carried out in the experimental plant depicted in Figure 3.2. The test rig contains a vertically aligned heat exchanger test section HX1 through which humid air and cooling water are passed in counter flow. The heat transfer surface of the test section HX1 is 49 cm^2. Dry compressed air is fed into the system through a compressed air valve, whereby the volume flow of the air can be adjusted using the mass flow controller MFC1 (Brooks, GF 040). A bypass follows the mass flow controller. The needle valve V1 can be used to regulate which part of the air mass flow passes through the bubble column B1 filled with DI water, which serves as a humidifier, and which part flows through the bypass. The temperature of the bubble column and the humified air can be controlled with a heat exchanger and the thermostat T1 (Lauda,

RA 8). The ratio of humid air through the bubble column B1 to dry air through the bypass can be used to adjust the relative humidity φ. The two subsequent heat exchangers, which can be tempered by thermostat T2 (Julabo, F25 HD), serve to regulate the temperature of the humid air flowing into heat exchanger cell HX1 and to avoid the entrainment of droplets from bubble column B1. Temperature, relative humidity and air pressure are measured at the inlet and outlet of the heat exchanger cell HX1 with a digital sensor (Ahlborn, FHAD46-C2L05). The system is open to the environment and the operating pressure is therefore the atmospheric pressure. The hoses and the heat exchanger cell are insulated to minimize heat loss. HX1 is made of poly(methyl methacrylate) (PMMA) to allow condensation behavior on the surface to be optically observed. To record the condensation behavior, a camera is mounted in front of HX1 on the side of the humid air. The ace U acA1440-73gm camera from Basler (resolution: 1440 px $\times$ 1080 px, sensor size: 4.97 $\times$ 3.73 mm^2) is equipped with a telecentric objective with fourfold magnification from Edmund Optics, which results in a maximum field of view of 1.24 mm x 0.93 mm. The camera system is connected to a high-performance LED ring light (MBJ Imaging, SRL-12) that is only triggered when the camera takes a picture, so that no additional heat is introduced into the system by the light source. The temperature of the cooling water circuit of HX1 is controlled by thermostat T3 (Lauda, RE 360 S). The water mass flow is regulated by a gear pump (Ismatec, MCP-Z) and measured by a Coriolis flow meter (Siemens, SITRANS FCT030). The temperature at the inlet and outlet of HX1 of the cooling water circuit is measured using PT100 sensors (Ahlborn, FPA15L0100).

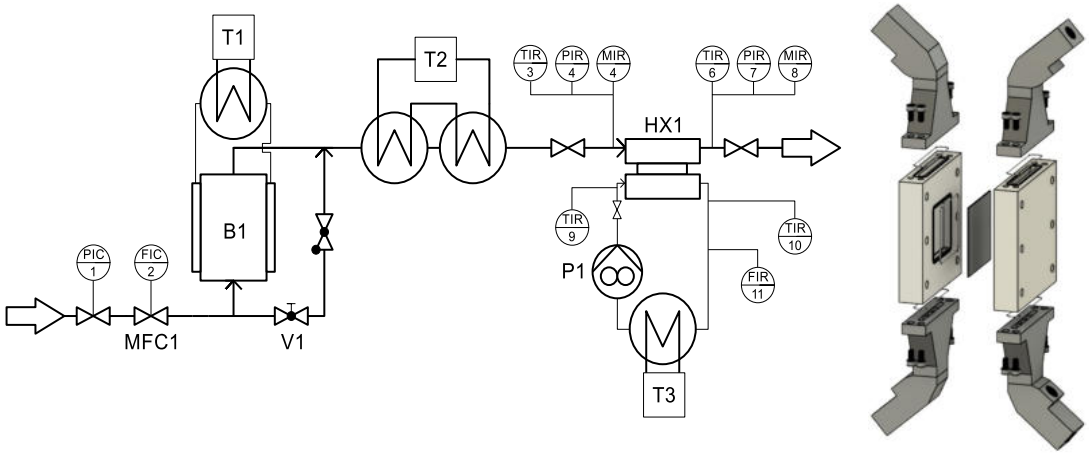

Figure 3.2: Schematic flowchart of the experimental set-up (l) and exploded view of the HX1 heat exchanger cell (r).

At the start of the experiments, the air temperature was regulated using thermostat T2 (Julabo, F25 HD) and thermostat T1 (Lauda, RA 8), both set to 20°C. Water cooling was achieved by setting thermostat T3 (Lauda, RE 630 S) to 5°C, resulting in an inlet water temperature at HX1 of approximately 6°C. Compressed air was adjusted to a pressure of 6 bar, and the volumetric flow rate was controlled at 10 L/min using the mass flow controller (Brooks, MFC GF 040). Resulting in a flow rate of the humid air of around 0.3 m/s and laminar flow with a Reynolds-number Re of 1,360. The temperature of the humid air is raised to 21°C which yields a temperature difference of 15°C between cooling water inlet temperature and humid air inlet temperature. Furthermore, the bypass valve was adjusted to reach the target relative humidity φ. The condensation experiments were performed at three different relative humidities φ = 60%, 80% and 100%. The HX1 is open to the environment, which is why the heat exchanger cell is at ambient pressure.

The mass flow rate of the cooling water was regulated using the gear pump P1 (Ismatec, MCP-Z) to achieve a measured mass flow of about 10 kg/h, as determined by the Coriolis flow meter (Siemens, SITRANS FCT030), which corresponds to a flow rate of the cooling water of around 5 mm/s. Resulting in a slow laminar flow with a Reynolds-number Re of 231.

Data acquisition was performed using the Ahlborn sensors and the mass flow data from the Coriolis flow meter were interfaced with the Almemo 2890-9 data logger from Ahlborn. The recorded data were subsequently transmitted to the Almemo Control Software (version 6.2.0.47) for further analysis.

Condensate mass

It is not possible to measure the condensate mass flow rate with the pilot plant, which is why the condensate mass flow rate was determined using an environmental chamber (Memmert, HPP 260). A 20 mm thick aluminum sample holder with a surface of 30 x 30 mm^2 is installed in the environmental chamber, which can be cooled by a thermostat (Julabo, FP51-SL). The samples are aligned vertically and attached to the aluminum cuboid with a self-adhesive heat-conducting tape (RS Pro Heat, conduction pad, 4.5 W/mK). The condensate mass drips down in a petri dish and is weighted by a microbalance (Kern, EWJ 300-3, stated reproducibility: 0.005 g). To record the condensation behavior two cameras are installed in the chamber. A ASI 1600 MM Mono (resolution: 4656 px × 3520 px, sensor size: 17.7 x 13.4 mm^2) with a tenfold magnifying lens resulting in a maximum field of view of 2.18 x 1.65 mm^2 perpendicular to the sample and a IDS UI-336xCP-M (resolution: 2,048 px × 1,088 px) under a grazing incidence of about 5∘ with a field of view of about 30 × 8 mm^2 to get a macroscopic view of the condensation, coalescence and sliding behavior. A detailed description of the system can be found in Fotachov et al. [80] and Fotachov et al. [64].

3.2.3 Data Reduction

The heat transfer can be calculated with the following equation [74].

$$\dot{Q} = \dot{M}_{\mathrm{W}}\, c_{\mathrm{p,W}}\, \Delta T_{\mathrm{W}} = U\, A\, \Delta T_{\log} \tag{3.1}$$

Where $\dot{M}_{\mathrm{W}}$ is mass flow of the cooling water circuit, $c_{\mathrm{p,W}}$ is the specific heat of water and ΔT_{W} is the temperature difference between the inlet and outlet of the heat exchanger cell HX1, U is the mean overall heat transfer coefficient and $\Delta T_{\log}$ is the logarithmic mean temperature difference. The mean overall heat transfer coefficient U is defined as [74]:

$$U = (\frac{1}{h_{\mathrm{V}}} + \frac{s}{\lambda} + \frac{1}{h_{\mathrm{W}}})^{-1} \tag{3.2}$$

Where h_{V} is the heat transfer coefficient of the humid air, h_{W} is the heat transfer coefficient of the cooling water, s is the thickness and λ the thermal conductivity of the sample. The heat flux density is calculated as [74]:

$$\dot{q} = \frac{\dot{Q}}{A} \tag{3.3}$$

With A as the heat transfer surface. In accordance with the law of energy conservation, the heat transferred to the water is equivalent to the heat released by the air. The heat transfer coefficient on the cooling water side h_{W} can be derived from the Nusselt number Nu [74]:

$$Nu = \frac{h_{\mathrm{W}}\, L}{\lambda_{\mathrm{W}}} \tag{3.4}$$

With the thermal conductivity of water λ_{W}. To determine the Nusselt number Nu, a Nusselt correlation is used for a plate in a parallel flow with laminar conditions. The Nusselt number Nu can be calculated for Reynolds numbers $Re < 5{\cdot}10^5$ using the following Nusselt correlation, as in Equation 3.4 [74].

$$Nu = 0.664\, Re^{\frac{1}{2}}\, Pr^{\frac{1}{3}} \tag{3.5}$$

Where Pr is the Prandtl number, which can be calculated using Equation 3.5 [74].

$$Pr = \frac{\eta_{\mathrm{V}}\, c_{\mathrm{p,V}}}{\lambda_{\mathrm{V}}} \tag{3.6}$$

η_{V} is the dynamic viscosity of the humid air and $c_{\mathrm{p,V}}$ is the specific heat capacity of humid air. The Reynolds number Re is calculated using Equation 3.7 [74].

$$Re = \frac{u_{\mathrm{V}}\, L}{\nu_{\mathrm{V}}} \tag{3.7}$$

In Equation 3.7, u_{V} is the velocity of the humid air and ν_{V} is the kinematic viscosity of the humid air.

3.2.4 CFD

CFD simulations were performed using OpenFOAM (vers. v2306) to compare the numerical results with experimental data and to ensure that the flow regime was laminar. Taking

advantage of the symmetry of the problem, the fluid domain was reduced to half the geometry and discretized using a high-resolution hexahedral mesh of approx. 3 million cells. The simulations used the rhoSimpleFoam solver, with water properties such as density, dynamic viscosity, thermal conductivity, and heat capacity approximated by polynomial regression curves derived from Stephan et al. [74]. These regressions, covering a temperature range of 0°C to 95°C, demonstrated a high degree of accuracy, with coefficients of determination close to 1, ensuring reliable property representation in the simulations. In addition to the heat capacity, the parameters density, dynamic viscosity and thermal conductivity are also approximated. All numerical analyses are assumed to be steady state. All simulations were performed for at least 10,000 iterations. The second-order linear upwind method was used for all analyses.

3.3 Results and Discussion

3.3.1 Wetting Behavior

The values of the CA measurements depicted in Table 3.1 show that the three different samples have a varied wetting behavior. SS has a static CA of 65°±7 which indicates a hydrophilic surface and the GC has a static CA of 97°±2° which indicates a hydrophobic surface. The SHGC exhibits superhydrophobic behavior with a CA greater than 170°, making accurate measurement challenging as droplets roll off due to minimal surface irregularities. The three images of the CA measurements in Figure 3.3 underline the different wetting behavior of the various surfaces.

The dynamic CA measurements demonstrated that the hydrophobic surface of GC has a better sliding behavior with a contact angle hysteresis (CAH) of 38°±10° compared to the hydrophilic surface of SS with a CAH of 51°±2°. The SHGC showed a superhydrophobic wetting behavior and the CAH could not be measured with the needle-in method because the drop ran away on the surface or the drop slipped when the needle was immersed into the drop, which is why a CAH of <5° is assumed. A short movie of the problems of the CA measurements of the SHGC surfaces can be seen in the Supporting Information.

Table 3.1: Static and dynamic contact angle measurements of the three different surfaces.

Sample	CA	Advancing CA	Receding CA	CA hysteresis
SS	65°±7°	70°±2°	19°±2°	51°±2°
GC	97°±2°	103°±5°	65°±9°	38°±10°
SHGC	>170°	-	-	<5°

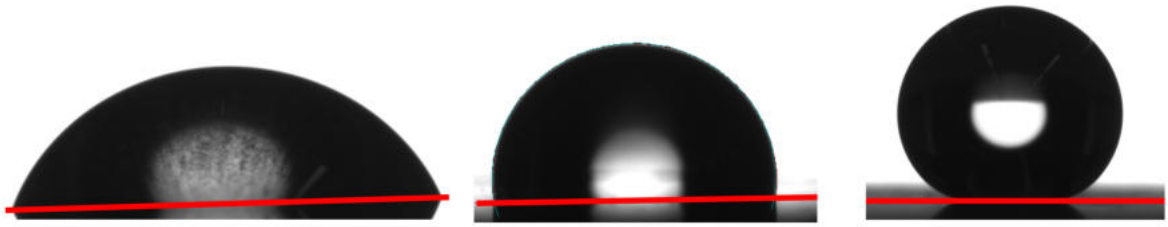

Figure 3.3: Comparison of the static contact angle measurements of the three different samples SS (l), GC (m) and SHGC (r).

A detailed description of the superhydrophobic copper nanostructures on the graphite composite is presented in Raab et al. [34]. For clarity and comprehensive analysis, the static and dynamic contact angle measurement values for the three different surfaces are presented in Figure 3.4. Furthermore, the Supporting Information includes a short movie about the perfect sliding behavior.

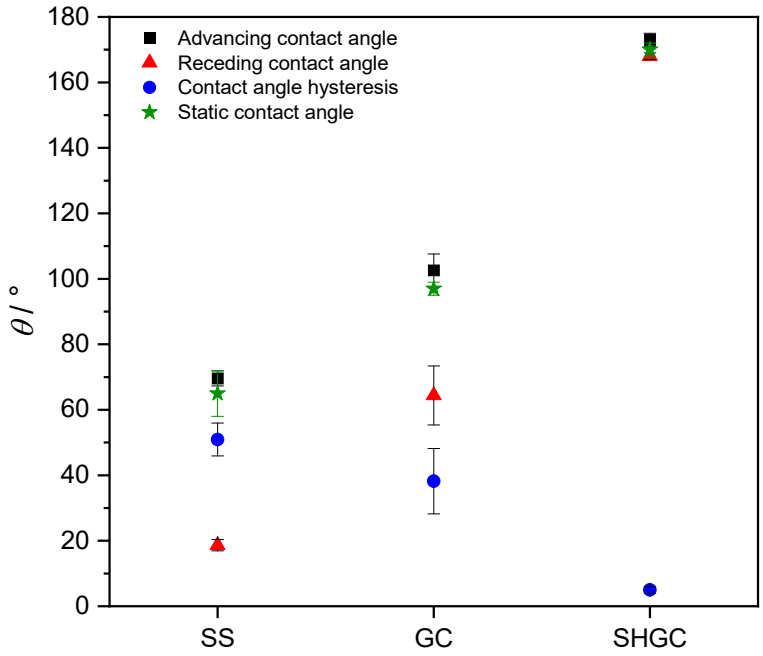

Figure 3.4: Comparison of the static and dynamic contact angle measurements.

3.3.2 Condensation Behavior and Heat Transfer

To determine the condensation heat transfer and the condensation behavior, the experiments were conducted for a period of four hours to ensure that a steady state behavior could be assumed. However, after 30 min to 60 min, all temperatures exhibited stability. The heat transfer rates presented are the average values measured from the point of steady state behavior (after 60 min) until the end of the experiments. To ensure the reproducibility of the results,

each experiment was conducted at least twice. The initial analysis presents findings for RH of 60% and 80%, serving as representative examples. While the overall condensation behavior remains consistent across different RH levels, the roll-off frequency increases with higher RH. This observation justifies the selection of 60% RH and 80% RH as illustrative cases. The impact of all investigated RH levels on heat transfer is comprehensively addressed in the discussion of the heat transfer results.

Condensation behavior

As previously stated, reflected-light images of the surface were obtained at regular intervals throughout the course of the experiments. This was done in order to gain a deeper insight into the condensation behavior. Figure 3.5 depicts the reflected-light images of the hydrophllic SS surface. Figure 3.6 illustrates reflected-light images of the hydrophobic GC surface and Figure 3.7 depicts reflected-light images of the superhydrophobic SHGC surface. The images were captured at designated time points $t_1 = 10$ min, $t_2 = 30$ min and $t_3 = 90$ min with a RH of $\varphi = 60$ %. It was observed that the condensation behavior of the surfaces at different RHs exhibited a high degree of similarity, with a notable increase in roll-off frequency. As illustrated in Figure 3.5, the condensation on SS predominantly manifests as a film. While no continuous film is observed, a limited number of round droplets are discernible. During the condensation process, the drops display hydrophilic surface behavior and are irregular in shape. By comparison, Figure 3.6 illustrates that the droplets on the GC are significantly rounder than those on SS. On the SHGC, the droplets appear to be perfectly round, as illustrated in Figure 3.7, indicating that condensation in this case occurs predominantly in the dropwise form. It is evident that, despite the samples being vertically positioned within the condensation system, drops exceeding 250 µm in diameter form on the surface. This is at odds with the findings of the contact angle measurements, which demonstrated perfect roll-off behavior and a notably low CAH.

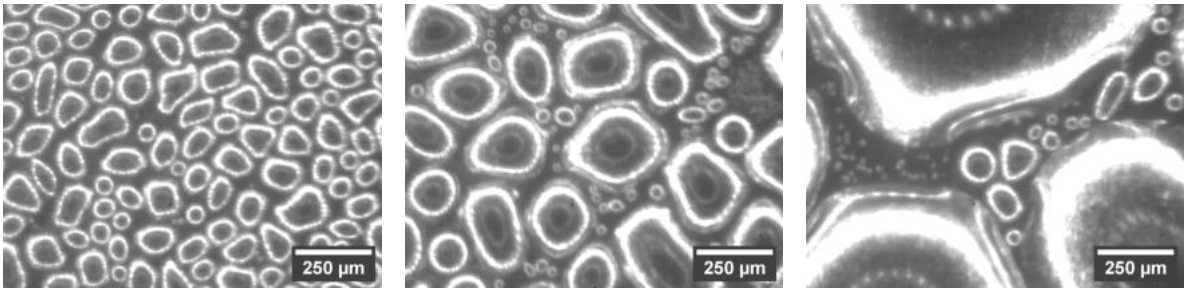

(a) t_1 **(b)** t_2 **(c)** t_3

Figure 3.5: Reflected-light images of the condensation experiment on SS at times t_1, t_2 and t_3 during an experiment with a RH of $\varphi = 60$ %.

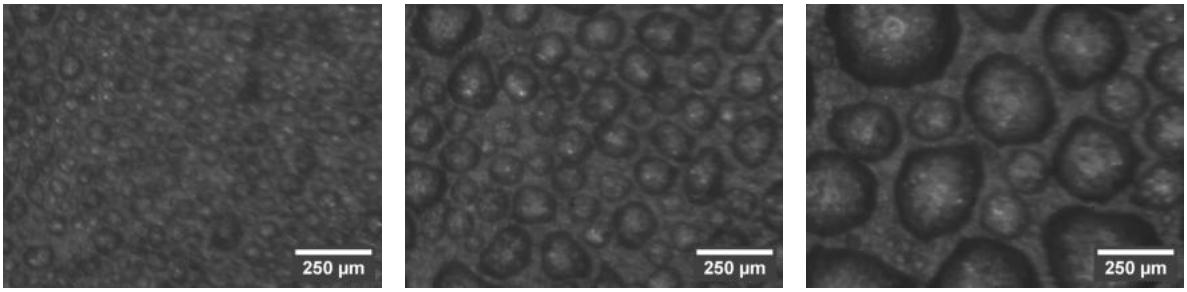

(a) t_1 **(b)** t_2 **(c)** t_3

Figure 3.6: Reflected-light images of the condensation experiment on GC at times t_1, t_2 and t_3 during an experiment with a RH of $\varphi = 60$ %.

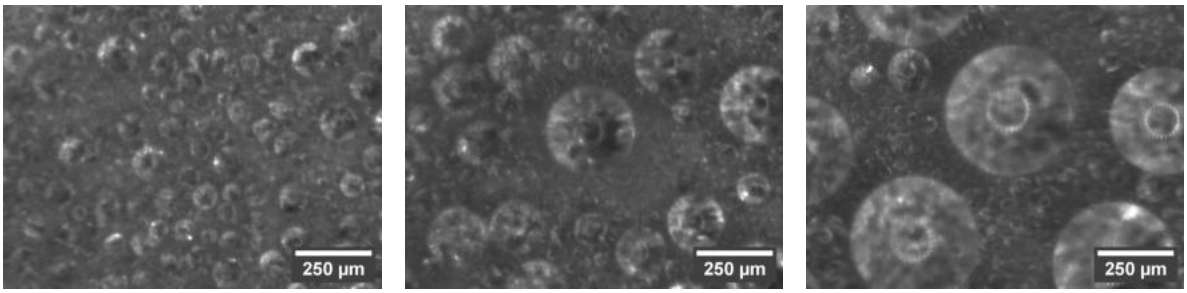

(a) t_1 **(b)** t_2 **(c)** t_3

Figure 3.7: Reflected-light images of the condensation experiment on SHGC at times t_1, t_2 and t_3 during an experiment with a RH of $\varphi = 60$ %.

The macroscopic images of the entire sample surface confirm the observations from the microscopic images. Figures 3.8, 3.9 and 3.10 depict the macroscopic images captured at the designated time points, $t_2 = 30$ min and $t_3 = 90$ min. The images were obtained at a temperature of $\vartheta = 20$°C and a RH of $\varphi = 80\%$. The images in Figure 3.8 show that condensation on SS is predominantly in the form of irregular, non-round droplets. This behavior is characteristic of a surface with high CA and CAH, where water spreads more easily over the substrate. The droplets were relatively large compared to the more hydrophobic GC and SHGC surfaces in Figures 3.9 and 3.10, indicating that the coalescence process was dominant on SS, resulting in the formation of fewer but larger droplets. The hydrophilic nature of SS favors the formation of a thin liquid film at higher condensation levels. However, under the experimental

conditions, the film remained discontinuous, highlighting the intermediate wetting state of the surface. This finding is consistent with previous studies. These observations serve as a reference point for comparing condensation behavior on more hydrophobic surfaces, where droplet formation and roll-off dynamics are expected to be significantly different. It should be added that the larger droplets ran off the sample into the Petri dish, which measured the mass of condensate throughout the experiments, whereas the droplets on the GC and SHGC adhered to the lower edge of the sample, which may distort the condensate mass measurements.

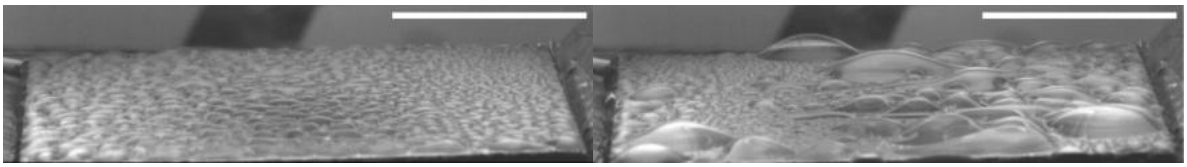

(a) t_2 **(b)** t_3

Figure 3.8: Macroscopic image of the entire sample surface on SS at times t_2 and t_3 during a condensation experiment with a RH of $\varphi = 80$ % at 20°C, scale bar equals 1 cm.

Figure 3.9 illustrates that condensation on the GC surface results in smaller droplets with a more uniform droplet size distribution (DSD) across the entire sample. A notable observation in Figure 3.9a is the presence of numerous larger droplets hanging from the lower edge of the sample after 30 min. This phenomenon can be attributed to the anisotropic thermal conductivity of the graphite composite, which is significantly higher in the in-plane direction than in the through-plane direction. This anisotropy results from the manufacturing process, such as calendering, which preferentially aligns the graphite particles in the in-plane direction. Ddetailed information on the graphite composites and their manufacturing processes are found in the work of Kiepfer et al. [13]. The increased thermal conductivity in the in-plane direction results in lower temperatures at the edges of the sample, promoting the initial formation of larger droplets in these regions. At t_2 after 90 min, very large droplets are also observed at the lower edge of the sample. This behavior can be explained by the strong adhesion of the droplets to the edges of the sample. In contrast to the hydrophobic surface of the GC, where droplets tend to roll off, the edge effects of the GC allow for better droplet adhesion compared to the SS where drops just run off. This combination of thermal and wetting properties significantly affects droplet dynamics and distribution, highlighting the role of material properties and manufacturing methods in condensation behavior.

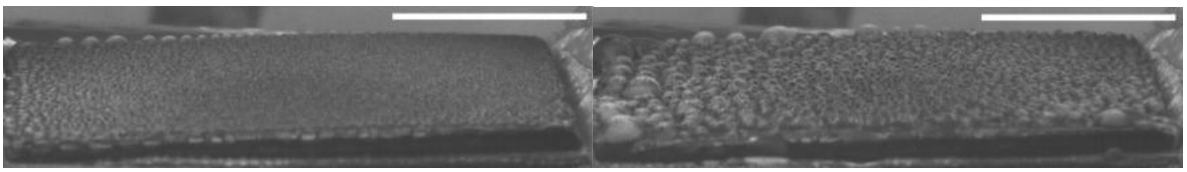

(a) t_2 **(b)** t_3

Figure 3.9: Macroscopic image of the entire sample surface on GC at times t_2 and t_3 during a condensation experiment with a RH of $\varphi = 80$ % at 20°C, scale bar equals 1 cm.

Figure 3.10 highlights the condensation behavior on the superhydrophobic graphite compos-

ite (SHGC), revealing distinct differences compared to the previously observed GC surface. The SHGC displays even smaller and rounder droplets, indicative of enhanced hydrophobicity. However, the DSD across the entire sample is less uniform compared to that of the GC surface. An important observation is the improved adhesion of droplets in the vertical condensation setup compared to the behavior observed during contact angle measurements. This discrepancy can be attributed to the Wenzel state, wherein droplets grow within the micro- and nanoscale surface structures of the metal oxide nanostructures (MONSTRs) of the SHGC. The strong interaction between the droplets and the textured surface leads to the so-called Wenzel pinning effect [81]. The Wenzel pinning effect occurs as droplets larger than approximately 100 µm in diameter experience enhanced adhesion to the surface, preventing them from rolling off. This phenomenon arises due to the increased contact area between the droplet and the surface features in the Wenzel state, resulting in stronger capillary forces that resist detachment. Consequently, larger droplets remain adhered to the surface, even under vertical conditions, leading to a non-uniform DSD. Another finding is the shedding of several droplets after 90 min, which effectively clears off smaller droplets as they run down the surface of the sample. This dynamic process not only removes existing droplets but also allows for the re-exposure of the surface, potentially facilitating further nucleation and growth of new droplets, that are essential for heat transfer [82]. This phenomenon highlights the role of droplet mobility in maintaining active condensation sites and influencing the overall droplet size distribution on the surface. Especially in Figure 3.10b it can be observed that rolling droplets become pinned at the lower edge of the sample resulting in large hanging drops. In the top-right corner of the sample, several larger droplets are visible that are noticeably less round. This irregularity indicates that the MONSTRs formation is governed by a stochastic process, leading to variability in the surface texture. Additionally, the coating with lauric acid appears to lack uniformity in this region. The droplets in this area deviate from typical superhydrophobic behavior, suggesting localized deficiencies in surface modification or inconsistent surface properties. In contrast, other regions of the sample exhibit characteristic superhydrophobic behavior, with smaller, more circular droplets and enhanced water repellency.

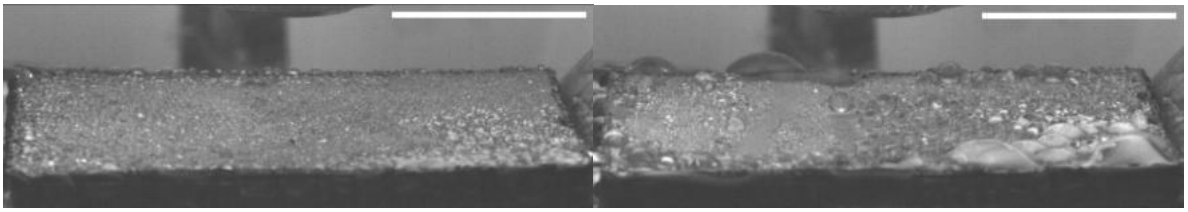

(a) t_2 **(b)** t_3

Figure 3.10: Macroscopic image of the entire sample surface on SHGC at times t_2 and t_3 during a condensation experiment with a RH of φ = 80 % at 20°C, scale bar equals 1 cm.

Heat transfer

The following section discusses the heat transfer characteristics observed during the experiments. Initially, the results for RH of 60% and 80% are presented, followed by the analysis of 100% RH. Figure 3.11 provides an example of the heat flux density for the SHGC at an RH

of $\varphi = 80\%$ as a function of time. After 60 minutes, all temperatures reach a stationary state, allowing the condition to be considered steady state. The average heat flux density determined from multiple experiments is 773 W/m^2 $\pm$ 4.5%. Diagrams from all additional experiments are included in the Supporting Information. A comprehensive summary of the heat flux densities is presented in Table 3.2. The heat flux densities are calculated using Equation 3.3 with Equation 3.1.

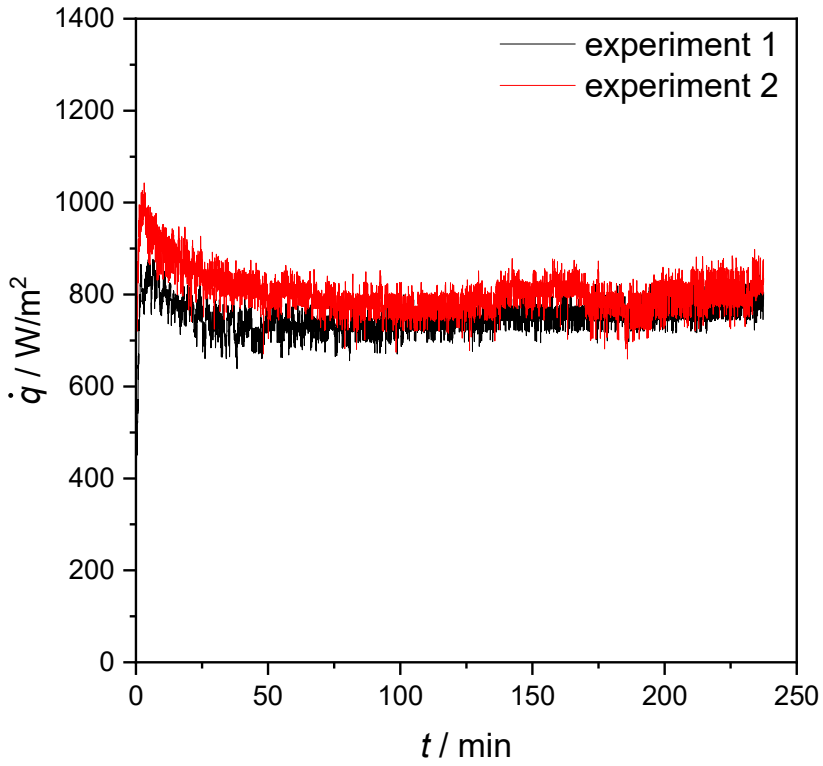

Figure 3.11: Heat flux density $\dot{q}$ for the SHGC at a RH of $\varphi = 80\%$.

The condensation heat transfer experiments conducted at 60% and 80% RH revealed distinct variations in heat flux densities across the tested samples, along with their associated uncertainties. At 60% RH, the SS sample demonstrated a heat flux density of 541 W/m^2 $\pm$ 12.1%, while GC achieved 556 W/m^2 $\pm$ 5.8%. The SHGC showed a lower heat flux density of 449 W/m^2 $\pm$ 7.3%. At 80% RH, the heat flux densities increased significantly due to higher condensation rates. The SS sample exhibited the highest heat flux density, reaching 978 W/m^2 $\pm$ 3.4%. The GC sample followed with 810 W/m^2 $\pm$ 7.2%, while the SHGC recorded 773 W/m^2 $\pm$ 4.5%. These results demonstrate a clear relationship between RH levels and heat flux densities, with higher RH leading to increased condensation rates and greater heat flux. The SS sample consistently showed the highest heat flux densities across both RH levels. In contrast, the GC and SHGC samples exhibited lower values. It is found that the values of the heat flux densities are all of the same order of magnitude. It is noticeable that the heat flux of the superhydrophobic surface is always the lowest. The reduced heat flux density of the

SHGC is due to the Wenzel pinning effect, which limits droplet mobility, and the additional thermal resistances introduced by the MONSTRs and lauric acid coating. Together, these factors hinder efficient heat transfer, resulting in lower performance compared to GC.

Table 3.2: Heat flux densities for 60% RH and 80% RH.

Sample	60% RH/ Wm^{-2}	80% RH/ Wm^{-2}
SS	541±12.1%	978±3.4%
GC	556±5.8%	810±7.2%
SHGC	449±7.3%	773±4.5%

The findings from the heat transfer measurements conducted at 100% RH are now analyzed and compared with the previously discussed results for 60% and 80% RH to identify trends and deviations in thermal performance. Diagrams from the heat flux densities over time for 100% RH are included in the Supporting Information as mentioned above. A comprehensive summary of the heat flux densities is presented in Table 3.3 and in Figure 3.12. The heat flux densities of the GC and the SHGC increased significantly compared to the stainless steel (SS), which exhibited nearly unchanged values under 100% RH. This indicates that the surface properties of the GC and SHGC, including enhanced droplet dynamics and potential modifications in thermal transport, play a critical role in condensation heat transfer under saturated conditions. The measurements were conducted multiple times to ensure reproducibility, and the observed values demonstrated consistent results, confirming the reliability of the experimental data. At 100% RH, the heat flux density of the SS sample was measured to be $968\,W/m^2 \pm 3.5\%$, remaining nearly unchanged compared to its performance at 80% RH. In contrast, GC exhibited a significantly higher heat flux density of $1320\,W/m^2 \pm 1.7\%$, representing a 36.4% increase in performance compared to SS. Similarly, the SHGC achieved a heat flux density of $1210\,W/m^2 \pm 2.3\%$, outperforming SS by 25%. The results reflect the shift in dominant mechanisms: at lower RHs, nucleation site activation energy limits condensation resulting in higher heat flux densities at the SS surface, while at saturated conditions, condensation behavior and droplet roll-off dynamics dominate heat transfer, favoring GC and SHGC over SS. Although the SHGC outperforms SS under saturated conditions, its heat flux density remains lower than that of GC. This difference is primarily due to the effects previously introduced. To further enhance the performance of SHGC, future work should focus on optimizing the surface structure and improving the uniformity and effectiveness of the low free surface energy coating.

Table 3.3: Heat flux densities for 60% RH, 80% RH and 100% RH.

	60 % RH	80 % RH	100 % RH
Sample	$W\,m^{-2}$	$W\,m^{-2}$	$W\,m^{-2}$
SS	541±12.1%	978±3.4%	968±3.5%
GC	556±5.8%	810±7.2%	1320±1.7%
SHGC	449±7.3%	773±4.5%	1210±2.3%

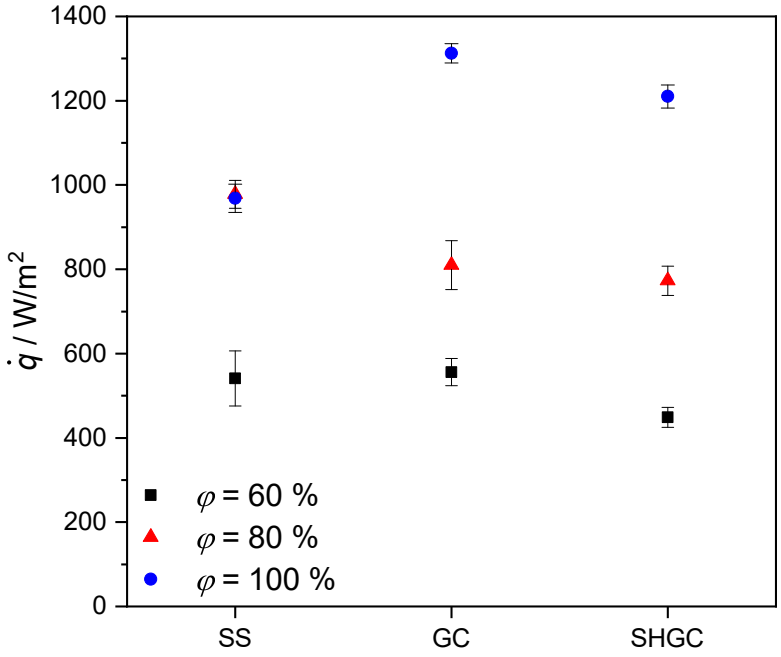

Figure 3.12: Heat flux densities $\dot{q}$ for all experiments with RH $\varphi = 60\%$, RH $\varphi = 80\%$ and RH $\varphi = 100\%$.

Now the heat transfer coefficient (HTC) of the vapor will be discussed, which represents the most critical parameter in evaluating the condensation performance. This is because the thickness s and thermal conductivity λ of the materials remain constant across all experiments. Additionally, the conditions in the cooling water circuit were maintained consistently, ensuring that the HTC on the water side is uniform for all measurements. To calculate the HTC of the cooling water side the Nusselt equation (see. Equation 3.5) for laminar flow was used [74]. Although the Reynolds number was 232, CFD simulations were performed to ensure that the flow was in a laminar regime due to the sharp edges at the inlet and outlet of the HX1. The CFD simulations confirmed that the flow was laminar. The HTC of the water cooling circuit was also determined using CFD simulations to provide a comparative benchmark for the experimental results, which will be discussed in chapter 3.4. The results of the experimental measured HTCs are provided in Table 3.4. Since the results of the HTCs depend on the measured heat flux densities and heat conductivities, the results of the heat flux densities and the HTCs behave almost the same. The largest difference is the thermal conductivity of stainless steel, which is about 8 times higher than that of the graphite composite, which is why GC and SHGC outperform SS at the HTCs even more. At 100% RH, GC achieves the highest HTC of $309\,\mathrm{W/m^2K} \pm 2.3\%$, followed by SHGC at $244\,\mathrm{W/m^2K} \pm 2.9\%$, while SS remains nearly unchanged at $134\,\mathrm{W/m^2K} \pm 6.5\%$.

Table 3.4: Heat transfer coefficient of the condensation experiments.

	60 % RH	80 % RH	100 % RH
Sample	$\mathrm{W\,m^{-2}\,K^{-1}}$	$\mathrm{W\,m^{-2}\,K^{-1}}$	$\mathrm{W\,m^{-2}\,K^{-1}}$
SS	60±6.3%	136±14.9%	134±6.5%
GC	64±4%	106±7.6%	309±2.3%
SHGC	51±1.9%	100±5.2%	244±2.9%

The experiments measuring condensate mass over 24 hours confirm the heat transfer measurements, as both GC and SHGC exhibited a little higher condensate mass compared to SS under the same conditions of 30°C and 60% RH (see Table 3.5). The condensation masses were measured at 30°C and 60% RH, since the climate chamber cannot reach 100% RH at 20°C and this constellation best matches the water content of the air, which could be explained by the previously mentioned drops adhering at the lower edges. Another reason could be that the condensation mass was only determined once due to the long period of time. The values of the lower RHs agree very well with the measured heat flux densities.

Table 3.5: Condensate mass after 24 h.

Sample	20°C 60% RH	20°C 80% RH	30°C 60% RH
SS	0.85 g	3.51 g	5.19 g
GC	0.56 g	2.93 g	5.24 g
SHGC	0.23 g	2.89 g	5.21 g

3.4 CFD

In this section the results of the CFD analysis are discussed. To evaluate convergence, both residuals and monitor points are observed. Residuals of about $1 \cdot 10^{-6}$ for pressure and $1 \cdot 10^{-8}$ for velocity and enthalpy could be achieved. Monitor points were set for pressure and temperature at several points near the inlet, the outlet and the region of interest. After about 2,500 steps, a constant course of all curves can be recognized. The heat transfer coefficient is calculated using a function which uses a fixed reference temperature for the calculation. The function is given by Equation 3.8:

$$h = \frac{\dot{q}}{T_\mathrm{c} - T_\mathrm{ref}} \tag{3.8}$$

Here, T_c is the local fluid temperature and T_ref is the reference temperature, which is set equal to the inlet temperature of the fluid domain. Therefore, T_ref is approx. 275.5 K, depending on the measurement result of the respective case. The entire numerical study consists of 12 different CFD simulations, which are compared to the 12 condensation experiments with 60% and 80% RH. Each simulation is carried out in agreement with an experimental study. The boundary conditions for the mass flow and the temperature inlet are determined in accordance with the measurement results. As a further parameter, the total heat flow was taken from the

experiment and set as constant in the simulation. The heat transfer coefficient and the mean outlet temperature were defined as target values for the simulation.

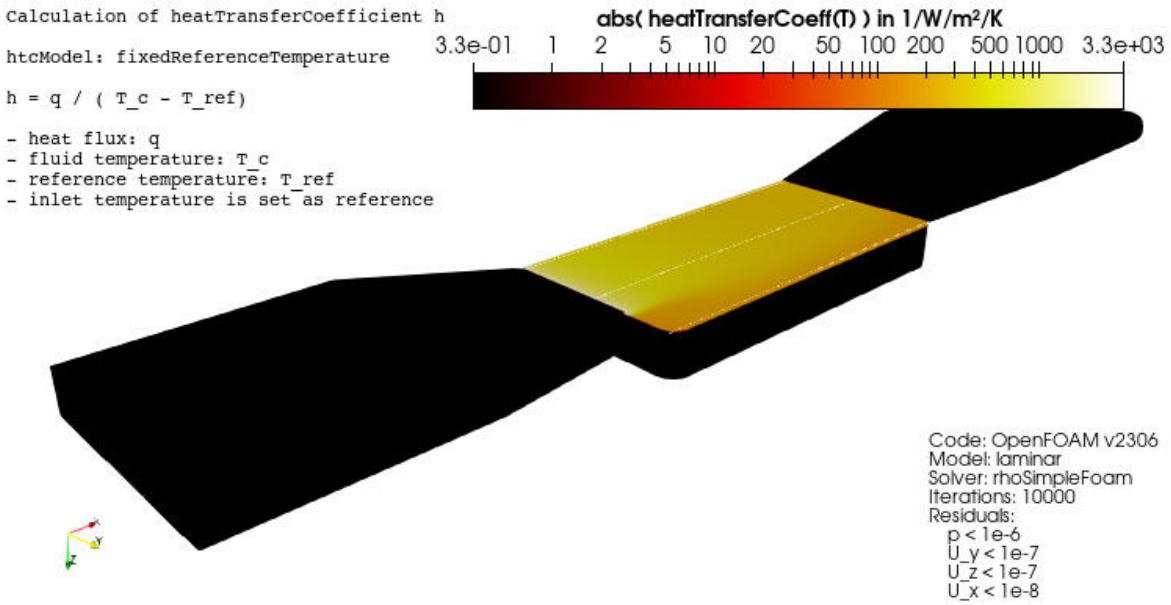

Figure 3.13: Results of the CFD analysis of the HTC of SHGC of the cooling water circuit for 60% RH condensation experiment - 3D contour plot of the HTC.

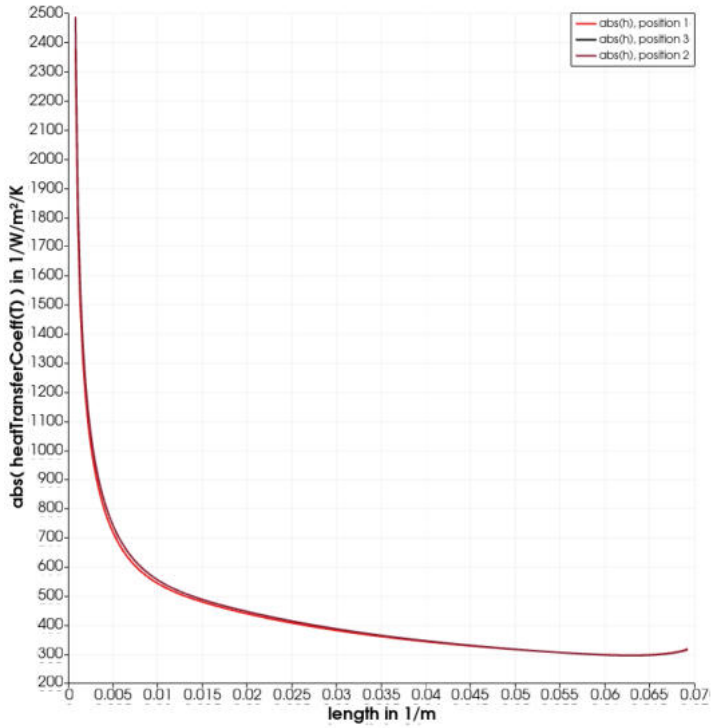

Figure 3.14: Results of the CFD analysis of the HTC of SHGC of the cooling water circuit for 60% RH condensation experiment - local heat transfer coefficient over the symmetry line.

Figures 3.13 and 3.14 show the heat transfer coefficient for a mass flow of approx. $\dot{M}_{\mathrm{W}} = 10$ kg/h and $T_{\mathrm{inlet}} = 279.47$ K as an example. All other data of the CFD simulations are

shown in the Supporting Information. Figure 3.13 depicts a 3D contour plot as an overview, while Figure 3.14 shows the course of the local heat transfer coefficient over the symmetry line. The mean value of the HTC for this case is $h_W = 378.72$ W/m^{2}K. Table 3.6 summarizes all the results of the tests carried out and the calculated, rounded HTCs without errors.

Table 3.6: Comparison of the experimental and the CFD analysis calculated HTCs.

	60 % RH		80 % RH	
Sample - Method	HTC_W W/m^{2}K	HTC_V W/m^{2}K	HTC_W W/m^{2}K	HTC_V W/m^{2}K
SS - CFD	383	53	386	109
SS - Exp.	187	60	187	136
GC - CFD	383	54	382	87
GC - Exp.	186	64	185	106
SHGC - CFD	381	44	384	83
SHGC - Exp.	184	51	187	100

The CFD simulations slightly overestimate HTCs on the water side, resulting in a lower calculated HTC for the vapor side compared to the experimental results. However, the simulated and experimental values remain within the same order of magnitude, and the HTCs on the vapor side show good agreement, demonstrating consistency between the numerical and experimental findings. This alignment reinforces the validity of the CFD model while highlighting minor deviations due to the inherent assumptions and simplifications in the numerical approach.

3.5 Conclusion and Outlook

This study investigates the wetting behavior, condensation dynamics, and heat transfer performance of stainless steel (SS), graphite composite (GC), and superhydrophobic graphite composite (SHGC) under varying relative humidity (RH) conditions. The results demonstrate that surface properties play a crucial role in influencing condensation behavior and heat transfer efficiency. Static and dynamic contact angle measurements revealed distinct wetting characteristics, with SS exhibiting hydrophilic properties ($65° \pm 7°$), GC displaying hydrophobic behavior ($97° \pm 2°$), and SHGC achieving superhydrophobicity ($> 170°$).

Condensation experiments conducted at RH levels of 60%, 80%, and 100% showed varying performance trends. While SS exhibited superior performance at lower RH levels, heat flux measurements at 100% RH revealed $968\,\mathrm{W/m^2} \pm 3.5\%$ for SS, $1,320\,\mathrm{W/m^2} \pm 1.7\%$ for GC, and $1,210\,\mathrm{W/m^2} \pm 2.3\%$ for SHGC. These results confirm that GC and SHGC significantly outperform SS, with GC achieving a 36.4% higher heat flux than SS. At 100% RH, GC also recorded the highest heat transfer coefficient (HTC) of $309\,\mathrm{W/m^2K} \pm 2.3\%$, outperforming SHGC ($244\,\mathrm{W/m^2K} \pm 2.9\%$) and SS ($134\,\mathrm{W/m^2K} \pm 6.5\%$). The superior performance of GC and SHGC is attributed to their enhanced surface properties, which facilitate efficient droplet nucleation, coalescence, and roll-off dynamics.

The condensate mass measurements corroborated the heat flux data, demonstrating that SS exhibits higher condensation performance at lower RHs but is surpassed by GC and SHGC at 100% RH. The slightly lower performance of SHGC compared to GC is attributed to the Wenzel pinning effect and additional thermal resistances introduced by its surface structures and hydrophobic coating.

Computational fluid dynamics (CFD) simulations validated the experimental results, showing strong agreement in vapor-side HTCs and confirming laminar flow conditions throughout the experiments.

These findings highlight the potential of GC and SHGC for enhancing condensation heat transfer in practical thermal management applications. Future work should focus on optimizing SHGC's surface architecture and improving the uniformity and effectiveness of its low surface energy coating to address current limitations and fully exploit its potential in advanced thermal systems.

The droplet size distribution will be addressed in subsequent publications, where it will be compared with predictions from a population model to provide deeper insights into droplet dynamics and their impact on condensation behavior.

4 Modeling Heat Transfer and Droplet Size Distribution on Graphite Composites

Contributor Roles Taxonomy

Raphael Raab: conceptualization; formal analysis; methodology; project administration; validation; visualization; writing - original draft; writing - review & editing

This chapter is intended for submission to a peer-reviewed journal for publication.

Abstract

In this study, the condensation behavior on stainless steel, graphite composites and superhydrophobic, hierarchically structured graphite composites was experimentally investigated. The influence of surface modification on droplet nucleation, growth, and detachment under humid air conditions was analyzed. To describe the condensation process, a previously established model from Wang et al. [83], originally developed for pure steam condensation, was extended by introducing correction terms to account for the presence of non-condensable gases and the properties of humid air from Tancon et al. [84].

The droplet size distribution on the untreated graphite composite was experimentally measured and successfully described using the modified model, showing good agreement with the experimental data.

Subsequently, the heat flux density on the structured and coated superhydrophobic graphite composite was predicted using the adapted model and compared to experimentally determined values. The comparison revealed that, although the modified model captured the general trends, further adjustments are required to accurately represent condensation behavior in the presence of humid air.

This work demonstrates the necessity of considering non-condensable gases in condensation modeling and provides a foundation for the development of more accurate predictive tools for condensation heat transfer on advanced, functionalized composite surfaces.

4.1 Introduction

Heat exchangers are critical components in various industries, particularly in the chemical sector. These devices frequently utilize condensation processes to enhance heat transfer, as phase change enables the release of significant amounts of latent heat. Condensation refers to the phase transition of a substance from a gaseous to a liquid state and can be classified into two primary types: film condensation and dropwise condensation. In film condensation, the condensate forms a continuous liquid film that envelops the heat-exchange surface, introducing an additional thermal resistance that impedes heat transfer efficiency. Conversely, dropwise condensation occurs when discrete liquid droplets form on the surface. These droplets grow, merge, and eventually detach, thereby minimizing thermal resistance and facilitating more effective heat transfer. Recently, the surface modification of superhydrophobic surfaces has been suggested as a promotion layer, shown in Figure 4.1.

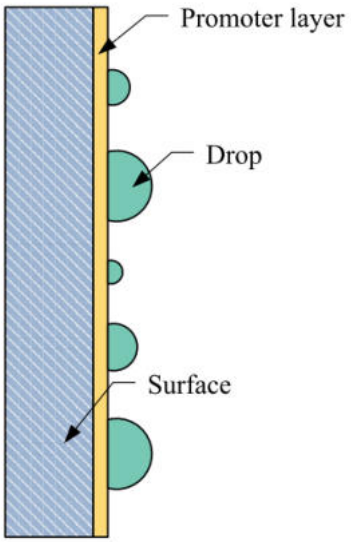

Figure 4.1: Schematic representation of droplet condensation [83].

Recently, polymers have been receiving more attention as materials for heat transfer devices because they have the advantages of high corrosion resistance and low cost compared to conventional materials such as metals [85]. However, one disadvantage of polymers is their low thermal conductivity, which impairs their efficiency in heat transfer. To solve this problem, composite materials are produced by incorporating carbon-based materials or ceramics into the polymers to increase thermal conductivity [86]. Additionally, heat transfer can be improved by structuring and coating the surfaces of polymer composites in a controlled manner. This increases the hydrophobicity of the surface, which promotes droplet condensation and thus achieves better heat transfer [87]. The number and size of the droplets during condensation can be investigated by means of a droplet size distribution. This distribution indicates how many droplets of a certain size are present on the surface. A common approach to modeling this distribution is a population balance, which maps the dynamics of droplet formation and development [88].

In this work, the condensation of water from humid air on a unprocessed and a structured

and coated graphite composite in a condensation unit is investigated and compared with the condensation behavior with that of polished stainless steel. The influence of the condensation behavior on the transferred heat flow is investigated. Furthermore, the droplet size distribution on unprocessed graphite composite is determined experimentally and additionally analyzed using the droplet size distribution model from Wang et al. [83] and Tancon et al. [84]. This model is also used to predict the heat flux density during condensation.

4.2 Experimental Section

4.2.1 Materials

The materials employed in this study were identical to those described in Chapter 3.2. For detailed information regarding their composition and preparation, refer to Chapter 3.2.

4.2.2 Experimental Setup

The test plant and its design is described in greater detail in Chapter 3.2. A brief sketch is given in Figure 4.2.

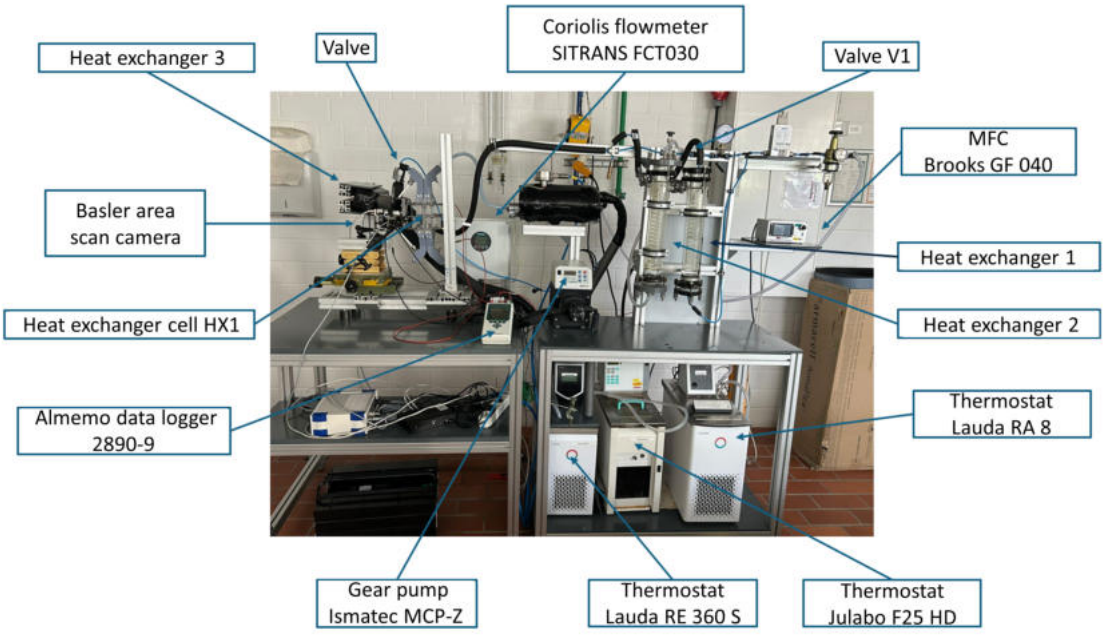

Figure 4.2: Brief overview of the experimental test rig.

For each sample, the experiments were carried out at a relative humidity of $\varphi = 60$ % and $\varphi = 80$ %. The duration of each experiment was approximately 4 hours to ensure that steady-state operation was achieved. In addition, each experiment was carried out twice to ensure reproducibility.

At the beginning of the tests, the Julabo F25 (HD) thermostat and the Lauda RA 8 thermostat were set to 20 °C to control the temperature of the air. The Lauda RE 630 S thermostat was

set to 5 °C to cool the water, which meant that the temperature of the water at the inlet to the HX1 was approximately 6.3 °C. The compressed air was set to 6 bar and the volume flow at the Brooks MFC GF 040 flow controller to 10000 mL/min. In addition, the valve on the bypass was opened until the desired relative humidity was reached.

The mass flow of the cooling water was adjusted via the gear pump MCP-Z so that a mass flow of approx. 10 kg/h could be measured at the Coriolis flowmeter SITRANS FCT030. The data recorded by the digital Almemo FHAD46-C2L05 probes from Ahlborn and the PT-100 temperature probes from Ahlborn, as well as the mass flow data, were recorded by the Almemo data logger 2890-9 from Ahlborn and transferred to the *Almemo Control* software version 6.2.0.47.

The camera settings were managed in the *Pylon Viewer 64-bit* software, version 6.3.0.23157.

Before the start of the experiment, it was ensured that the temperatures of the air and water, as well as the relative humidity and the mass flow of the cooling water, were constant. Then the data recording was started using the *Almemo-Control* software and the image recording was started using the *Pylon Viewer 64-bit* software. Finally, the valve in front of the HX1 was opened, causing the air to be directed into HX1. This marked the start of the experiment.

The camera used in this experimental setup to determine the droplet size distribution is an ASI 1600 MM Mono (resolution: 4656 px × 3520 px, maximum image detail: 2.18 mm × 1.65 mm), which is equipped with a tenfold microscope lens. The experiments were carried out under the same experimental conditions. The subcooling of the humid air was 15 °C and the relative humidity was set to φ =60 % and φ =80 %. The exact experimental setup is described in Fotachov et al. [89]. The experiments were carried out for the polished stainless steel, the graphite composite without surface modification and the graphite composite with surface modification.

The program *Fiji* in version 1.54k was used to evaluate the images. A sequence of image processing steps was applied that allowed the detection of the drops and the evaluation of the drop size. The result was a table showing the Feret radius of each individual drop detected.

The images used for the evaluation were all taken during the stationary state of the condensation. For each experiment, 36 images were evaluated at equal time intervals and the mean values were finally calculated from the results.

4.2.3 Data Reduction and Modeling

Population balances

Population balances can be used to determine the number of objects with a certain property [88]. These objects include crystals, bubbles and droplets, which can be analyzed, for example, in terms of their size or mass. In this way, the number of droplets in a certain balance space can be described as a function of the droplet size [88]. The droplet balance is of interest for the droplet condensation investigated in this work, which is why the droplet size distribution is used below as an example to describe a population balance. Instead of the absolute number of

droplets, a number density function f is usually used. This describes the number of droplets per unit area and radius and is therefore given in the unit m^{-3}.

In general, the change in the number density function of the droplets can be described by Eq. 4.1 [88].

$$\frac{df}{dt} = -\frac{d(G \cdot f)}{dr} + B - D \tag{4.1}$$

Where G is the growth rate of the droplets, r is the radius of the droplets, B (birth) is a source and D (death) is a sink. In the case of droplet condensation, for example, a source is the direct condensation on the surface, whereby nucleation sites for condensation are formed. A sink is the rolling or bouncing of droplets when they become too large to remain attached to the surface. The entrainment of droplets when other droplets roll off also represents a sink.

The growth rate can also be described, as in Eq. 4.2, as the change of the radius r over time t [88].

$$G = \frac{dr}{dt} \tag{4.2}$$

Modeling the droplet dize distribution and heat flux during dropwise condensation

In the following, the model used in this work to describe the droplet size distribution during droplet condensation from humid air is described. The model for droplet condensation from pure water vapor from Wang et al. [83] is used as a basis. However, some equations of the model are replaced by those of Tancon et al. [84] in order to be able to transfer the model to condensation from humid air instead of water vapor. Wang et al. [83] describe the droplet condensation of pure water vapor on a surface that is additionally coated with a promoter. The promoter coating favors droplet condensation and prevents film condensation. Micro- and/or nanostructures can be used for this purpose, which increase the contact angle between the water droplets and the surface, thus creating hydrophobic or superhydrophobic surfaces [83]. The main difference between condensation of water from pure water vapor and humid air is that air contains non-condensable gases (e.g. nitrogen, oxygen, etc.). These cause additional resistance to heat transfer, which means that the heat transfer coefficient h and, consequently, the heat flux $\dot{q}$ transferred, are significantly lower when condensing from humid air than when condensing from pure water vapor [84].

Heat flux through a drop

At first, the heat transfer resistances of the single droplets are considered. For this purpose, Wang et al. [83] first describe the temperature difference ΔT between the surface and the humid air. As Eq. 4.3 shows, this is composed of four individual terms.

$$\Delta T = \Delta T_{\mathrm{C}} + \Delta T_{\mathrm{I}} + \Delta T_{\mathrm{D}} + \Delta T_{\mathrm{P}} \tag{4.3}$$

Where, ΔT_{C} is the temperature difference that occurs due to the curvature of the drop, ΔT_{I} is the temperature difference that occurs due to the resistance of the gas-liquid phase interface,

ΔT_D describes the temperature difference that occurs due to the droplet as an additional heat conduction resistance. ΔT_P is the temperature difference between the promoter layer and the substrate surface due to heat conduction through the promoter [83]. ΔT_c is given by Eq. 4.4.

$$\Delta T_c = \frac{2\,T_s\,\sigma}{H_{fg}\,r\,\rho_l} \tag{4.4}$$

In Eq. 4.4, T_S describes the dew point of the humid air, σ the surface tension of the condensate, H_{fg} the enthalpy of vaporization of the condensate, r the radius of the droplets and ρ_L the density of the condensate. ΔT_I can be determined using Eq. 4.5.

$$\Delta T_I = \frac{\Phi}{2\,\pi\,r^2\,h_{I,NCG}\,(1-cos\,\theta)} \tag{4.5}$$

Where, Φ is the heat flow through a single droplet, $h_{I,NCG}$ is the interfacial heat transfer coefficient, and θ is the contact angle between the condensate and the surface. The interfacial heat transfer coefficient $h_{I,NCG}$ takes into account the presence of non-condensable gases and can be determined using Eq. 4.6 [84].

$$h_{I,NCG} = \left(\frac{x/M_L}{x/M_L + x/M_A}\right)\frac{2\,\alpha_c}{2-\alpha_c}\left(\frac{M_L}{2\,\pi\,R\,T_S}\right)^{1/2}\frac{H_{fg}^2\,\rho_V}{T_S}\left(1-\frac{p_V}{2\,H_{fg}\,\rho_V}\right) \tag{4.6}$$

In Eq. 4.6 is M_L the molar mass of the condensate, M_A the molar mass of the dry air, R the universal gas constant, ρ_V the density of the humid air, x is the relative water loading of the air and p_V is the vapor pressure of the humid air. α_c is a so-called accommodation coefficient, which describes the efficiency of energy transfer during collisions between gas molecules and a surface [90].

The temperature difference ΔT_D can be calculated according to Eq. 4.7 [83].

$$\Delta T_D = \frac{\Phi\,\theta}{4\,\pi\,\lambda_L\,r\,sin\,\theta} \tag{4.7}$$

In Eq. 4.7, λ_L is the thermal conductivity of the condensate.

The temperature difference ΔT_P can be determined according to Eq. 4.8.

$$\Delta T_P = \frac{\Phi\,\delta_P}{\pi\,r^2\,\lambda_P\,sin^2\,\theta} \tag{4.8}$$

Where, λ_P is the thermal diffusivity of the promoter, δ_P is the thickness of the promoter coating, and r is the radius of the droplet.

The heat flow Φ through a single drop can be calculated using Eq. 4.9 as follows, where the individual heat transfer resistances are in the denominator [83]. The equation for the heat flow Φ given in the paper by Wang et al. [83] differs from Eq. 4.9 shown here in that the denominator contains the term $\frac{r\,sin\,\theta}{\lambda_L} + \frac{\theta}{4}$ instead of $\frac{\theta\,r\,sin\,\theta}{4\,\lambda_L}$ are the terms $\frac{r\,sin\,\theta}{\lambda_L} + \frac{\theta}{4}$. However, this was identified as incorrect because, on the one hand, the individual terms from the temperature

differences in the denominator should be a sum and, on the other hand, the terms $\frac{r\,sin\,\theta}{\lambda_L}$ and $\frac{\theta}{4}$ should not be added due to different units.

$$\Phi = \frac{\pi\, r^2\, sin\,\theta\, \Delta T\, (1 - \frac{r_{min}}{r})}{\frac{1+cos\,\theta}{2\, h_{I,NCG}} + \frac{\theta\, r\, sin\,\theta}{4\, \lambda_L} + \frac{\delta_P}{\lambda_P}} \tag{4.9}$$

Here, r_{min} is the minimum radius of the droplets.

Modeling the droplet size distribution

According to Wang et al. [83] and Tancon et al. [84], the drops are divided into small and large drops. Small droplets range from the minimum radius r_{min} to the coalescence radius r_e, and large droplets range from the coalescence radius r_e to the maximum radius r_{max}. This classification is based on the assumption that the small drops are mainly formed by direct condensation on the surface and the large drops are formed by coalescence of smaller drops.

This results in two drop size distributions, namely $n(r)$ as the drop size distribution for small drops and $N(r)$ as the drop size distribution for large drops.

The size distribution $N(r)$ of the large drops can be described using Eq. 4.10 [83, 84].

$$N(r) = \frac{1}{3\,\pi\, r^2\, r_{max}} \left(\frac{r}{r_{max}}\right)^{-2/3} \tag{4.10}$$

The maximum drop radius r_{max} when condensing from humid air can be determined using Eq. 4.11 [84].

$$r_{max} = \left[\frac{6\,\sigma\,(cos\,\theta_{rec} - cos\,\theta_{adv}) sin\,\theta_{Eq}}{\pi\,(2 - 3\,cos\,\theta_{Eq} + cos^3\,\theta_{Eq})\rho_L\, g}\right]^{1/2} \tag{4.11}$$

Where, g is the acceleration due to gravity, θ_{adv} is the advancing angle, θ_{rec} is the receding angle, and θ_{Eq} is the equilibrium contact angle, which is defined via Eq. 4.12 [84].

$$\theta_{Eq} = cos^{-1}\,(0.5\,cos\,\theta_{adv} + 0.5\,cos\,\theta_{rec}) \tag{4.12}$$

The drop size distribution for small drops $n(r)$ is determined using a population balance. Since Wang et al. [83] does not describe the exact procedure for determining $n(r)$, the equations needed for the population balance are given by Wen et al. [91]. In the balance, the number of droplets entering the size range corresponds to the sum of the droplets leaving the size range and rolling off the surface. The interaction of these processes is assumed to be stationary. The described relationship is shown in Eq. 4.13 [91].

$$A\, n_1\, G_1 = A\, n_2\, G_2 + S\, n_{1-2}\, \Delta r \tag{4.13}$$

Where, A describes a section of the surface on which the condensation takes place, G is the growth rate of the droplets that grow into the size range or grow out of it, respectively. S is the roll-off rate and n_{1-2} is the average population density between r_1 and r_2.

The growth rate G of the droplets is as defined in Eq. 4.14 [91].

$$G = \frac{dr}{dt} \tag{4.14}$$

Eq. 4.13 can be further simplified and summarized to Eq. 4.15.

$$\frac{d}{dr}(G\,n) + \frac{n}{\tau} = 0 \tag{4.15}$$

Here, τ is the roll-off period and can be written as the quotient of A and S, as shown in Eq. 4.16 [91].

$$\tau = \frac{A}{S} \tag{4.16}$$

The heat flow through a single drop Φ can also be expressed as a function of the growth rate of the drops. This relationship is shown in Eq. 4.17 [83].

$$\Phi = \rho_{\mathrm{L}}\, H_{\mathrm{fg}}\, 2(1 - cos\,\theta)\,\pi\, r^2\, \frac{dr}{dt} \tag{4.17}$$

By equating Eq. 4.6 and Eq. 4.17, the growth rate G of the droplets can be represented as in Eq. 4.18 [83].

$$G = A_1\, \frac{1 - r_{\mathrm{min}}/r}{A_2\, r + A_3} \tag{4.18}$$

The parameters A_1, A_2 and A_3 can be used to summarize various quantities, as described in Eq. 4.19a, Eq. 4.19b and Eq. 4.19c [83].

$$A_1 = \frac{\Delta T}{2\,\rho_{\mathrm{L}}\, H_{\mathrm{fg}}} \tag{4.19a}$$

$$A_2 = \frac{\theta\,(1 - cos\,\theta)}{4\,\lambda_{\mathrm{L}}\, sin\,\theta} \tag{4.19b}$$

$$A_3 = \frac{1}{2\,h_{\mathrm{I,NCG}}} + \frac{\delta_{\mathrm{P}}\,(1 - cos\,\theta)}{\lambda_{\mathrm{P}}\, sin^2\,\theta} \tag{4.19c}$$

A distinction between small and large drops is made by the coalescence radius r_{e}, which is defined as in Eq. 4.20 [84].

$$r_{\mathrm{e}} = \frac{1}{4\,\sqrt{N_{\mathrm{s}}}} \tag{4.20}$$

Where, N_{s} is the nucleation density.

The minimum radius r_{min} of water droplets that form by condensation from humid air can be calculated using Eq. 4.21 [84].

$$r_{\min} = \frac{2\,\sigma\,T_{\mathrm{S}}}{\rho_{\mathrm{L}}\,H_{\mathrm{fg}}\,\Delta T_{\mathrm{S}}} \tag{4.21}$$

In Eq. 4.21, ΔT_{S} is the temperature difference between the sample surface and the dew point of the humid air.

The droplet size distribution for small droplets $n(r)$ can then be obtained from the solution of Eq. 4.15 using Eq. 4.18 as an expression for the growth rate of the droplets. Thus, the drop size distribution for small drops $n(r)$ can be described by Eq. 4.22 [83, 84].

$$n(r) = \frac{1}{3\,\pi\,r_{\mathrm{e}}^3\,r_{\max}} \left(\frac{r_{\mathrm{e}}}{r_{\max}}\right)^{-2/3} \frac{r\,(r_{\mathrm{e}} - r_{\min})}{r - r_{\min}} \frac{A_2\,r + A_3}{A_2\,r_{\mathrm{e}} + A_3} exp(B_1 + B_2) \tag{4.22}$$

Here, B_1, B_2 and τ in Eq. 4.23a, Eq. 4.23b and Eq. 4.23c are used to summarize some quantities [83].

$$B_1 = \frac{A_2}{\tau\,A_1}\left[\frac{r_{\mathrm{e}}^2 - r^2}{2} + r_{\min}\,(r_{\mathrm{e}} - r) + r_{\min}^2\,ln\left(\frac{r_{\mathrm{e}} - r_{\min}}{r - r_{\min}}\right)\right] \tag{4.23a}$$

$$B_2 = \frac{A_3}{\tau\,A_1}\left[r_{\mathrm{e}} - r + r_{\min}\,ln\left(\frac{r_{\mathrm{e}} - r_{\min}}{r - r_{\min}}\right)\right] \tag{4.23b}$$

$$\tau = \frac{3\,r_{\mathrm{e}}^2\,(A_2\,r_{\mathrm{e}} + A_3)^2}{A_1\,(11\,A_2\,r_{\mathrm{e}}^2 - 14\,A_2\,r_{\mathrm{e}}\,r_{\min} + 8\,A_3\,r_{\mathrm{e}} - 11\,A_3\,r_{\min})} \tag{4.23c}$$

Total heat flux

The total heat flow during droplet condensation consists of the heat flow through the individual droplets of different sizes and the heat flow through the surface on which there are no droplets, as well as the heat flow through the droplet surfaces.

Thus, the heat flux $\dot{q}$, as shown in Eq. 4.24, can be described [83].

$$\dot{q} = \dot{q}_{\mathrm{F}} + \dot{q}_{\mathrm{D}} \tag{4.24}$$

Where, $\dot{q}_{\mathrm{F}}$ is the convective heat flux and $\dot{q}_{\mathrm{D}}$ is the heat flux through the individual droplets.

The convective heat flux $\dot{q}_{\mathrm{F}}$ is composed of two parts, as shown in Eq. 4.25 [83].

$$\dot{q}_{\mathrm{F}} = \left(\frac{A_{\mathrm{F}}}{A} + \frac{A_{\mathrm{LV}}}{A}\right) h_{\mathrm{F,V}}\,\Delta T \tag{4.25}$$

Here, $h_{\mathrm{F,V}}$ is the convective heat transfer coefficient of the humid air. The first part of Eq. 4.25, $\frac{A_{\mathrm{F}}}{A}$, represents the ratio of the drop-free surface to the total condensation surface. This ratio can be represented by $1-\phi$, where ϕ is the ratio of the surface covered by droplets to the total surface area. ϕ can be described by Eq. 4.26 [83].

$$\phi = \int_{r_{\min}}^{r_{\mathrm{e}}} \pi\,r^2\,sin^2\,\theta\,n(r)\,dr + \int_{r_{\mathrm{e}}}^{r_{\max}} \pi\,r^2\,sin^2\,\theta\,N(r)\,dr \tag{4.26}$$

The second part from Eq. 4.25, namely $\frac{A_{\mathrm{LV}}}{A}$, describes the ratio of all drop surfaces to the total surface area. This ratio is described by Eq. 4.27 [83].

$$\frac{A_{\mathrm{LV}}}{A} = \int_{r_{\min}}^{r_{\mathrm{e}}} 2\,\pi\,r^2\,(1 - cos\,\theta)\,n(r)\,dr + \int_{r_{\mathrm{e}}}^{r_{\max}} 2\,\pi\,r^2\,(1 - cos\,\theta)\,N(r)\,dr \tag{4.27}$$

The heat flux through all droplets $\dot{q}_{\mathrm{D}}$ can be determined from the heat flux through a single droplet and the droplet size distributions $n(r)$ and $N(r)$. This relationship is given by Eq. 4.28 [83].

$$\dot{q}_{\mathrm{D}} = \int_{r_{\min}}^{r_{\mathrm{e}}} \Phi(r)\,n(r)\,dr + \int_{r_{\mathrm{e}}}^{r_{\max}} \Phi(r)\,N(r)\,dr \tag{4.28}$$

Inserting Eq. 4.25 to Eq. 4.28 into Eq. 4.24 yields the relationship shown in Eq. 4.29 for the total heat flux density [83].

$$\dot{q} = \left[(1-\phi) + \int_{r_{\min}}^{r_{\mathrm{e}}} 2\,\pi\,r^2\,(1 - cos\,\theta)\,n(r)\,dr + \int_{r_{\mathrm{e}}}^{r_{\max}} 2\,\pi\,r^2(1 - cos\,\theta)\,N(r)\,dr\right] h_{\mathrm{F,V}}\,\Delta T + \dot{q}_{\mathrm{D}} \tag{4.29}$$

The convective heat transfer coefficient $h_{\mathrm{F,V}}$ of the humid air can be determined using the Nusselt number Nu according to equation Eq. 4.30 [83].

$$h_{\mathrm{F,V}} = \frac{Nu\,\lambda_{\mathrm{v}}}{L} \tag{4.30}$$

Here, λ_{v} is the thermal conductivity of the humid air and L is a characteristic length [83].

The Nusselt number Nu can be calculated for Reynolds numbers $Re < 5{\cdot}10^5$ using the following Nusselt correlation, as in Eq. 4.31, [83].

$$Nu = 0.664\,Re^{\frac{1}{2}}\,Pr^{\frac{1}{3}} \tag{4.31}$$

Where, Pr is the Prandtl number, which can be calculated as follows via Eq. 4.32 [83].

$$Pr = \frac{\eta_{\mathrm{V}}\,c_{\mathrm{p,V}}}{\lambda_{\mathrm{V}}} \tag{4.32}$$

In Eq. 4.32, η_{V} is the dynamic viscosity of the humid air and $c_{\mathrm{p,V}}$ is the specific heat capacity of the humid air [83].

The Reynolds number Re can be calculated using Eq. 4.33 [83].

$$Re = \frac{u_{\mathrm{V}}\,L}{\nu_{\mathrm{V}}} \tag{4.33}$$

In Eq. 4.33, u_{V} is the velocity of the humid air and ν_{V} is the kinematic viscosity of the humid air.

The condensation behavior should be examined in more detail using the model for droplet condensation described in chapter 4.2.3 [83, 84]. The model was implemented for this purpose with the equations given in chapter 4.2.3 in the *Julia* programming language.

The model was used to determine the droplet size distribution, which was then used to calculate the heat flux density, which is considered below.

To apply the model to condensation from humid air, some properties of humid air had to be calculated. The specific heat capacity of humid air $c_{\mathrm{p,V}}$, the dynamic viscosity of humid air η_{V} and the thermal conductivity of humid air λ_{V} were determined using the relationships from Cheng et al. [92]. The density of humid air ρ_{V} was determined using an equation from the VDI Heat Atlas [93]. The dew point of the humid air T_{d}, as well as the vapor pressure of the humid air p_{v} were calculated using empirical equations [94].

The nucleation density N_{s} was assumed to be $6.1 \cdot 10^8$ m^{-2}, as taken from Tancon et al. [84], and the accommodation coefficient was assumed to be $\alpha_{\mathrm{c}} = 0.001$.

To calculate the velocity of the gas side u_{v}, the volume flow set in the condensation experiments and the cross-sectional area are used.

For the static contact angle θ, an angle of 170° was assumed for the graphite composite with surface modification considered here, for the advancing contact angle θ_{adv}, an angle of 170° was also assumed, and for the receding contact angle θ_{rec} an angle of 165° was assumed.

The lauric acid, which was used to lower the surface energy of the mirco- and nanostructured graphite composite considered in this work, is considered a promoter layer in the modeling. A promoter thickness of $\delta_{\mathrm{P}} = 0.5 \cdot 10^6$ m was assumed.

The temperature difference ΔT between the humid air and the sample surface was determined for the modeling under some simplifications. It was assumed that both the flowing cooling water and the flowing humid air have a uniform temperature. Furthermore, it was assumed that the heat transfer takes place without losses to the environment. With the help of the experimentally determined heat flux $\dot{q}$ and the heat transfer coefficient $h_{\mathrm{F,W}}$ of the cooling water, as well as the thickness of the graphite composite s and the thermal conductivity of the graphite composite λ, it was possible to determine the temperature of the sample surface on the side of the humid air using Fourier's law of heat conduction [93]. The temperature difference ΔT then resulted as the difference between the temperature of the humid air and the surface temperature of the graphite composite on the side of the humid air.

The model only describes droplet condensation on a surface coated with a promoter. Therefore, the modeled heat flux result is compared only to the experimental heat flux result for the surface-modified graphite composite (SHGC).

4.3 Results and Discussion

The contact angle measurements were performed as in chapter 3.2.2. The results of the measured data is depicted in Figure 4.3.

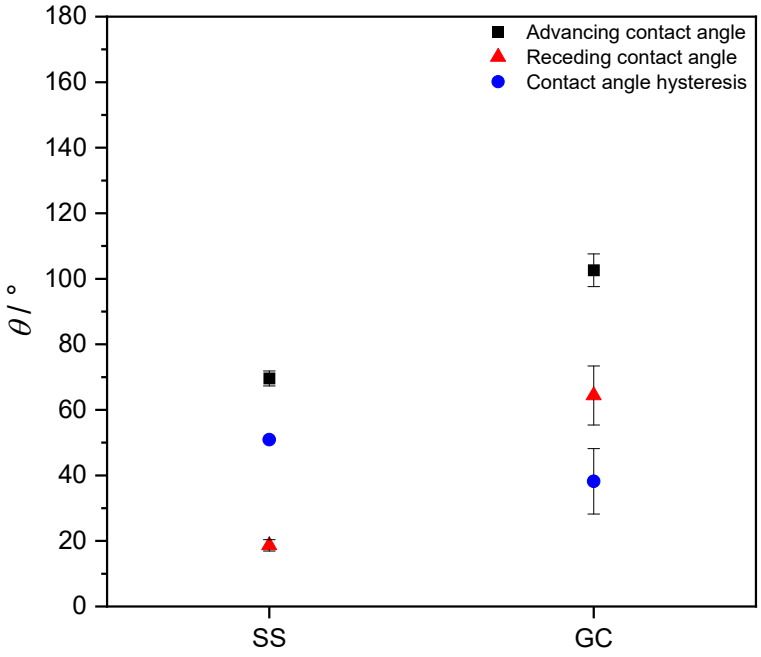

Figure 4.3: Comparison of experimentally determined contact angles of the dynamic measurements.

The contact angle measurement for the superhydrophobic graphite composite surface could not be recorded for these measurements because it was so water-repellent that the drops rolled off immediately after settling with the contact angle microscope.

To further investigate the condensation, the droplet size distribution on the graphite composite without surface modification (GC) was experimentally determined and additionally mapped by a modified model from Wang et al. [83] and Tancon et al. [84].

In the following section, the results of the experimentally determined droplet size distribution are compared with the results of the modeled droplet size distribution $N(r)$ in the steady state.

For this purpose, the drop size distributions on the graphite composite without surface modification (GC) for relative humidities of $\varphi = 60$ % and $\varphi = 80$ % were determined experimentally, as described in chapter 4.2.3.

Here, the determination of the drop size distribution was only possible from a radius of about 10 µm, because the drops with a smaller radius were not recognizable for the evaluation program in the image section. For this reason, the experimental results are compared exclusively

with the modeled drop size distribution for large drops $N(r)$. This was calculated, as explained in chapter 4.2.3, using Equation 4.10.

The results of the experimentally determined drop size distribution and those of the modeled drop size distribution are plotted in Figure 4.4 in a double logarithmic scale as a function of the drop radius r. The number of drops per radius and area is represented on the ordinate by $N(r)$.

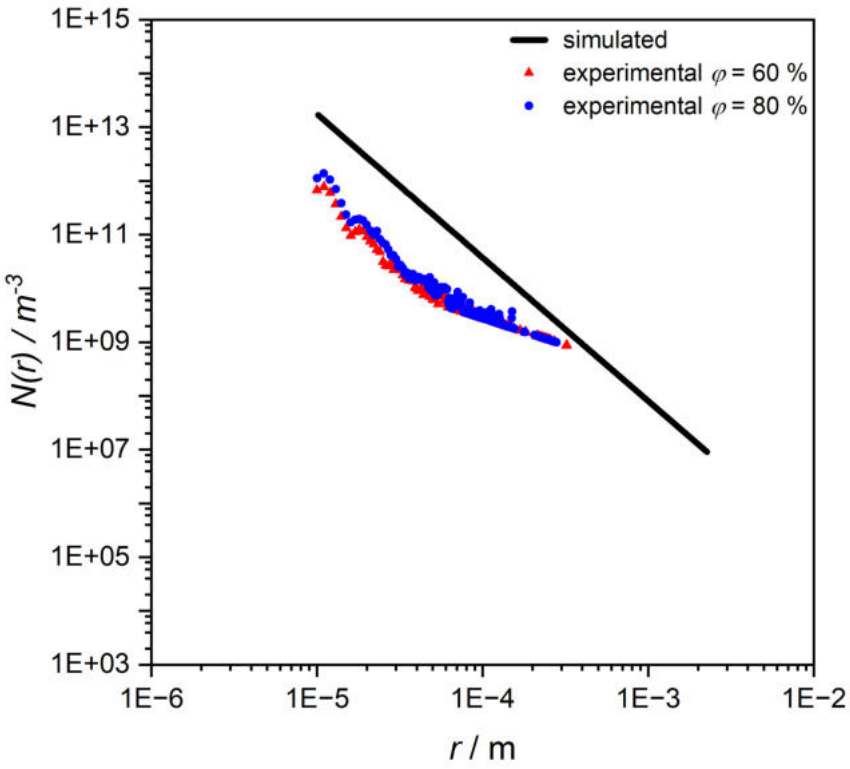

Figure 4.4: Comparison of experimentally determined and modeled drop size distributions $N(r)$ of the graphite composite without surface modification (GC) at relative humidities of $\varphi = 60$ % and $\varphi = 80$ %.

Figure 4.4 shows that both the model and the experimentally determined results show the same trend. The larger the drops become, the fewer of them there are on the sample surface. The model of the drop size distribution shows a linear decrease in the double-logarithmic representation. The experimental results of the drop size distribution also suggest a linear decrease. Furthermore, it can be seen that the experimentally determined results of the droplet size distribution are very similar for a relative humidity of $\varphi = 60$ % and $\varphi = 80$ %. However, the experimentally determined droplet size distribution is lower than the droplet size distribution modeled for all droplet radii considered.

The deviations between the experimental and modeled results can be traced back to the *Fiji* evaluation program.

The spatial calibration of the images was first set by assigning a distance of 3520 pixels to

correspond to 1650 µm, using micrometers (µm) as the unit and applying the calibration globally. Subsequently, automatic thresholding was performed using the default method to segment the structures of interest from the background. The "Black Background" option was activated to ensure that the background would be black in the subsequent binary conversion. The image was then converted into a binary mask, and subsequently inverted so that the particles of interest appeared white on a black background. After reconfirming the "Black Background" setting, two successive dilation steps were applied to slightly expand and connect nearby structures, followed by hole filling to ensure that all segmented structures were solid. A watershed algorithm was then employed to separate touching structures at narrow points. To further refine the segmentation, shape smoothing was performed with a relative proportion of Fourier descriptors set to 1, after which a second watershed operation was applied to optimize the separation. Particle analysis was conducted on the resulting structures, selecting only those with an area between 50 µm and infinity and a circularity between 0.75 and 1.00, while excluding edge-touching particles and displaying the results as overlay masks. Finally, the processed image was saved as a PNG file and the measurement results were exported as a CSV file, both to the specified file paths.

The program was not always able to clearly recognize the drops, which often resulted in too few drops being detected in a particular size range. This fact is shown in Figure 4.5.

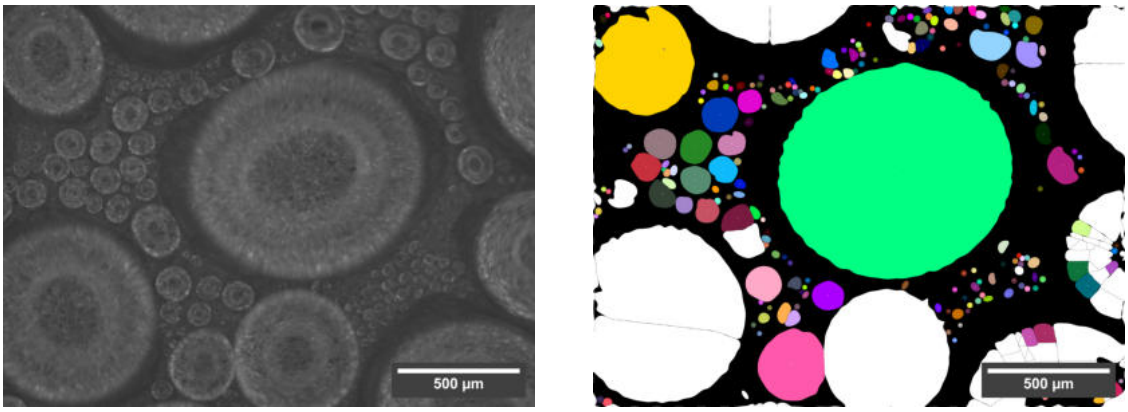

(a) Original image **(b)** Image after processing in Fiji

Figure 4.5: Images of water droplets during condensation on graphite composite without surface modification at a relative humidity of $\varphi = 60$ % before (left) and after (right) processing in Fiji.

Figure 4.5 shows the original image, taken during the condensation, on the left and the same image after processing and evaluation in the Fiji program on the right. The colored drops in the right-hand image are those that were identified as drops in the evaluation program. The white drops in the image, on the other hand, were not evaluated because, for example, some of them protrude from the image section. In addition, some areas of the right image are black, where there are actually drops, but they were not recognized as such. The deviation of the experimental drop size distribution from the modeled drop size distribution is due to the failure to recognize drops.

4.4 Modeling the Heat Flux

The model of Wang et al. [83] and Tancon et al. [84] first describes the droplet size distribution during condensation and also enables the calculation of the heat flux using the droplet size distribution. To further compare the model with the experimental data, the heat flux calculated using the model was considered.

In the following section, the result of the heat flux density calculated using the model is compared with the result of the experimentally determined heat flux density for the graphite composite with surface modification (SHGC) at a relative humidity of $\varphi = 80$ %.

The heat flux was calculated using the model described in chapter subsection 4.2.3 according to the procedure which is shown there.

The experimentally determined value of the heat flux was determined as described in subsection 3.2.3.

The calculated heat flux density by the model is 196.6 W/m^2 and the experimentally determined heat flux density from chapter 3 is 775.81 W/m^2. So the modeled value is 75% lower than the experimentally determined value. This large deviation shows that the model of Wang et al. [83], despite some adjustments using equations from Tancon et al. [84], does not yet sufficiently describe the condensation process from humid air instead of pure water vapor.

One possible explanation for this is that the model does not realistically represent the droplet size distribution $n(r)$ for small drops (see chapter 4.2.3). The droplet size distribution $n(r)$ determined by the model for small drops could not be confirmed experimentally because these drops are too small to be recorded using image-optical technology. In addition, the small drops are crucial for heat transfer [95]. Only a very small proportion of the heat is transferred via the larger drops. Even a small deviation in the drop size distribution $n(r)$ of the small drops would lead to a large change in the heat flux.

In the model, the heat flux is calculated from the heat transfer coefficient h_F (see chapter 4.2.3). For the graphite composite with surface modification (SHGC), this results in a heat transfer coefficient of $h_\mathrm{F,V} = 8$ W/(m^{2}K), which seems too small compared to the experimentally determined values of the heat transfer coefficients in chapter 3.

However, these two heat transfer coefficients cannot be compared directly either because they are applied or calculated in different ways. In the experimental part of this work, the heat transfer coefficient $h_\mathrm{F,V}$ is calculated from the heat flux, and in the considered model, the convective heat transfer coefficient $h_\mathrm{F,V}$ is first calculated using a Nusselt correlation and then used to determine the heat flux.

In general, the method of calculating the heat flux in the experimental part in chapter 3.2.3 also differs greatly from the calculation using the model from Wang et al. [83] and Tancon et al. [84] (see chapter 4.2.3), which makes it difficult to compare specific quantities.

4.5 Conclusion and Outlook

In this work, the results of the experiments from chapter 3 were compared to the model described in chapter 4.2.3

The drop size distribution on the untreated graphite composite was experimentally determined with the help of camera recordings. The drop size distribution was additionally predicted using a model from Wang et al. [83] and Tancon et al. [84] and the results compared. The results showed good agreement between the experimental results and the model, with the small deviations being due to the experimental image evaluation in the Fiji program.

Finally, the same model was used by Wang et al. [83] and Tancon et al. [84] to predict the heat flux during the condensation of water from humid air on the surface of the graphite composite with surface modification. The heat flux density calculated by the model showed a large deviation from the experimentally determined heat flux density. In general, the model of Wang et al. [83] could be responsible for this, since it is actually designed for the condensation of water from pure water vapor, whereas in this work the condensation from humid air was considered. The humid air contains non-condensable gases, such as nitrogen and oxygen, which create additional resistance to the mass transfer of water, thereby limiting heat transfer. Despite some adjustments to the model from Wang et al. [83] with equations from Tancon et al. [84] that describe the condensation of water from humid air, no good agreement with the experimental data could be achieved.

Due to this large deviation, the model should be examined in more detail in the future and some further adjustments should be made to the humid air condition. Another idea would be to use a different model to predict the condensation of water droplets from humid air on superhydrophobic surfaces, such as that of Baghel et al. [96] or Zheng et al. [97].

In the future, the wetting behavior of superhydrophobic surfaces could be further investigated experimentally to find a way to prevent the long adhesion of the droplets to the samples or to promote the formation of nucleation sites for the small droplets. This could increase heat transfer and further improve graphite composites, or polymer composites in general, as materials in heat exchangers.

5 Conclusion and Outlook

This thesis focuses on the superhydrophobization and characterization of highly filled graphite composites containing 80 wt.-% graphite particles with regard to their condensation behavior. Polymers are gaining importance as heat exchanger materials in the chemical industry, primarily due to their excellent chemical resistance in highly corrosive environments. The main challenge is to overcome their low thermal conductivity and develop strategies to optimize their thermal performance for efficient heat transfer applications. In this work, a composite material based on a conventional thermoplastic matrix was employed, incorporating a high mass fraction of graphite particles to enhance its thermal conductivity. In parallel, the objective of this study is to further improve heat transfer performance by modifying the surface of these composites to promote targeted dropwise condensation through tailored surface structuring and functionalization. The major obstacle to the effective utilization of superhydrophobic surfaces in industrial applications is ensuring their long-term durability and, in view of the heat transfer, a targeted droplet condensation with an increased heat transfer coefficient.

Chapter 2 presents a robust and scalable approach for the fabrication of superhydrophilic and superhydrophobic surfaces on thermally conductive polymer–graphite composites via thermal imprinting combined with hierarchical structuring using metal oxide nanostructures (MONSTRs). The method leverages reusable silicon wafer molds, which can be regenerated through pyrolysis, thereby offering both process longevity and economic efficiency. The integration of microstructured features with secondary nanostructuring and subsequent surface functionalization using stearic or lauric acid enabled the achievement of superhydrophobicity, as evidenced by static contact angles exceeding 160° for aluminum oxide nanostructures and 170° for copper oxide nanostructures, along with contact angle hysteresis values below 5°. The formation of superhydrophobic aluminum oxide structures was contingent on prior microstructuring through thermal embossing, whereas copper-based nanostructures demonstrated comparable wetting performance even without additional microscale features. The aluminum metal oxide nanostructures exhibited extremely small structural sizes, which necessitated prior microstructuring of the surface to achieve superhydrophobic behavior by enhancing the hierarchical surface roughness. In contrast, the copper metal oxide nanostructures formed significantly larger, needle-like morphologies, resembling the structures observed in black silicon. Due to their size and anisotropic shape, the copper-based nanostructures were capable of imparting superhydrophobic properties independently, without requiring additional microstructuring. A systematic investigation of the influence of fatty acid concentration and exposure time revealed that maximum contact angles, approaching 180°, were achieved within 30–60 minutes. However, prolonged exposure (24 hours) led to excessive surface coverage by the fatty acids, particularly on copper nanostructures, resulting in a measurable decline in contact angle. The

presented manufacturing technique offers a high degree of versatility and scalability and is therefore well suited for a wide variety of industrial applications.

Chapter 3 provides a comprehensive analysis of the wetting behavior, condensation dynamics, and heat transfer performance of stainless steel (SS), graphite composite (GC), and superhydrophobic graphite composite (SHGC) under varying relative humidity (RH) conditions. The results underscore the critical influence of surface wettability on condensation mechanisms and thermal transport efficiency. Static and dynamic contact angle measurements confirmed distinct wetting regimes: SS exhibited hydrophilic behavior ($65° \pm 7°$), GC showed hydrophobic characteristics ($97° \pm 2°$), and SHGC achieved superhydrophobicity ($> 170°$). Condensation experiments conducted at RH levels of 60%, 80%, and 100% revealed that while SS outperformed at lower RH, GC and SHGC demonstrated superior heat transfer at saturated conditions. At 100% RH, GC achieved the highest heat flux of $1,320\,\mathrm{W/m^2} \pm 1.7\%$, followed by SHGC ($1,210\,\mathrm{W/m^2} \pm 2.3\%$) and SS ($968\,\mathrm{W/m^2} \pm 3.5\%$). Corresponding heat transfer coefficients (HTCs) were $309\,\mathrm{W/m^2K} \pm 2.3\%$ for GC, $244\,\mathrm{W/m^2K} \pm 2.9\%$ for SHGC, and $134\,\mathrm{W/m^2K} \pm 6.5\%$ for SS. The enhanced performance of GC and SHGC is attributed to favorable surface characteristics that promote efficient droplet nucleation, coalescence, and shedding. Condensate mass measurements corroborated heat flux trends, showing that GC and SHGC surpass SS at higher RHs. The slightly reduced performance of SHGC relative to GC is ascribed to the Wenzel pinning effect and increased thermal resistance from hierarchical surface features and the hydrophobic coating. CFD simulations supported the experimental findings, confirming laminar flow conditions and yielding vapor-side heat transfer coefficients in close agreement with measured data. The results highlight the potential of thermally conductive graphite composites, particularly with surface functionalization, to enhance condensation heat transfer in industrial heat exchanger applications.

Chapter 4 focuses on the application of population balance modeling (PBM) for predicting heat transfer rates and droplet size distributions during condensation processes. In the chemical industry, accurate modeling of phase change phenomena, such as condensation, is critical for the design and optimization of energy-efficient heat exchangers and separation systems. Population models enable the prediction of droplet dynamics, including nucleation, growth, coalescence, and departure, all of which strongly influence local heat transfer coefficients and overall process performance. Such predictive capabilities are particularly important for evaluating new materials and surface treatments without relying exclusively on time-consuming and costly experimental campaigns. In chapter 4, the droplet size distribution on an untreated GC surface was experimentally determined using high-resolution imaging and analyzed via the Fiji software. These results were compared with predictions from the PBM developed by Wang et al. [83] and extended by Tancon et al. [84]. A good agreement was observed between the model and the experimental data, with only minor discrepancies attributed to limitations in the image analysis process. The same model was subsequently employed to predict the heat flux resulting from water condensation on surface-modified GC under humid air conditions. However, significant deviations were found between the predicted and experimental heat flux densities. This discrepancy is primarily attributed to the original formulation of the model by Wang et al. [83], which assumes condensation from pure water vapor and does not fully account for the influence of non-condensable gases (NCGs), such as nitrogen and oxygen, present in

humid air. These gases introduce additional mass transfer resistance, thereby reducing condensation rates. Despite modifications incorporating the humid air corrections proposed by Tancon et al. [84], the model could not accurately capture the experimental heat transfer behavior, highlighting the need for further refinement of PBMs to extend their applicability to real-world condensation scenarios involving complex gas mixtures and structured surfaces.

While the current study demonstrates the potential of surface-structured polymer–graphite composites for enhanced condensation heat transfer, further research is essential to optimize these surfaces for long-term industrial use. In particular, the durability and stability of hierarchical surface features under prolonged thermal and mechanical stress must be systematically evaluated. Moreover, enhancing droplet shedding dynamics through improved surface design could lead to higher droplet removal rates, thereby sustaining dropwise condensation and further increasing heat transfer coefficients. Future investigations should focus on tailoring micro- and nanoscale geometries to minimize contact line pinning and promote continuous droplet departure. In parallel, there is a pressing need for the development of advanced condensation models that incorporate the effects of NCGs. Existing models, primarily developed for pure vapor systems, fail to capture the mass transfer limitations and interfacial resistances introduced by NCGs, which are ubiquitous in industrial condensation scenarios. A predictive framework that couples droplet population dynamics with heat and mass transfer in multicomponent gas mixtures would represent a significant advancement, enabling more accurate simulation and design of condensation-based thermal management systems.

Nomenclature

Latin Letters

Symbol	Description	Unit
A	Total heat transfer area	m^2
A_F	Heat transfer area not wetted by droplets	m^2
A_{LV}	Surface area of the droplets	m^2
B	Birth	$m^{-3}s^{-1}$
c_p	Specific heat capacity	J $kg^{-1}K^{-1}$
D	Death	$m^{-3}s^{-1}$
f	Number density function	m^{-3}
g	Acceleration due to grativity	ms^{-2}
G	Growth rate of the droplets	$m\,s^{-1}$
H	Height	µm
H_{fg}	Enthalpy of evaporation of the condensate	J kg^{-1}
h_I	Overall heat transfer coefficient	W m^{-2} K^{-1}
h_I	Interfacacial heat transfer coefficient	W m^{-2} K^{-1}
h_F	Convective heat transfer coefficient	W m^{-2} K^{-1}
L	Characteristic length	m
L_W	Length of the silicon wafers	mm
M	Molecular weight	kg mol^{-1}
M_A	Molecular weight of the dry air	kg mol^{-1}
M_L	Molecular weight of the condensate	kg mol^{-1}
$\dot{M}_W$	Mass flow rate of cooling water	kg s^{-1}
n	Droplet size distribution for droplets $<$ r_E	m^{-3}
N	Droplet size distribution for droplets $>$ r_E	m^{-3}
N_s	Nucleation density	m^{-2}
Nu	Nusselt number	-
p_V	Vapor pressure of humid air	Pa
Pr	Prandtl number	-
$\dot{Q}$	Heat flux	W
$\dot{q}$	Heat flux density	W m^{-2}
$\dot{q}_D$	Heat flux density through all droplets	W m^{-2}
$\dot{q}_F$	Convective heat flux	W m^{-2}
R	Universal gas constant	J $mol^{-1}K^{-1}$
Re	Reynolds number	-
r	Drop radius	m
r_e	Coalescence radius	m
r_{max}	Maximum drop radius	m
r_{min}	Minimum drop radius	m

continued ...

... continued

S_a	Mean arithmetic roughness	µm
S	Roll-off rate	$m^2 s^{-1}$
s	Sample thickness	m
t	Time	s
T	Temperature	K
T_S	Dew point temperature of humid air	K
u	Velocity	$m\ s^{-1}$
U	Thermal transmittance	$W\ m^{-2}\ K^{-1}$
W	Width	µm
w_L	Mass fraction of water in humid air	kg/kg
w_L	Mass fraction of water in humid air	kg/kg
x	Specific humidity	kg/kg

Greek Letters

Symbol	Description	Unit
α_c	Accommodation coefficient	-
Δr	Difference between two specific radii	-
ΔT	Temperature difference between the sample surface and the humid air	K
ΔT_C	Temperature difference due to drop curvature	K
$\Delta a T_D$	Temperature difference due to heat conduction through the drop	K
ΔT_I	Temperature difference due to the resistance at the phase interface	K
ΔT_{log}	Mean logarithmic temperature difference	K
ΔT_M	Mean logarithmic driving temperature gradient	K
ΔT_P	Temperature difference due to heat conduction by the promoter	K
ΔT_S	Temperature difference between the sample surface and the dew point of the humid air	K
ΔT_W	Temperature difference of the cooling water	K
δ_P	Thickness of the promoter layer	m
η	Dynamic viscosity	Pa s
θ	Contact angle	°
θ_{Eq}	Equilibrium contact angle	°
ϑ	Temperature	°C
λ	Thermal conductivity	$W\ m^{-1} K^{-1}$
ν	Kinematic viscosity	$m^2 s^{-1}$
ρ	Density	$kg\ m^{-3}$
ρ_l	Density of the condensate	$kg\ m^{-3}$
σ	Surface tension	$N\ m^{-1}$
τ	Roll-off period	s
φ	Relative humidity	%
ϕ	Ratio of the surfaces of the droplets to the total heat transfer area	m^2 / m^2

continued ...

. . . continued

Φ	Heat flux through a single droplet	W

Subscripts

Symbol	Description
A	Dry air
adv	Advancing
C	Curvature
D	Droplets
F	Convective
I	Interfacial
L	Liquid condensate
LV	Total surface area of all droplets
e	Coalescence
Eq	Equilibrium
max	Maximum
min	Minimum
NCG	Non-condensable gases
P	Promoter
rec	Receding
S	Saturated
V	Humid air
W	Cooling water

Abbreviations

Symbol	Description
B	Bubble column
CA	Contact angle
CAH	Contact angle hysteresis
CFD	Computational fluid dynamics
DI	Deionized water
DWC	Dropwise condensation
FEP	Fluorinated ethylene propylene
FWC	Filmwise condensation
GC	Graphite composite
HTC	Heat transfer coefficient
HX1	Heat exchanger test section
LED	Light-emitting diode
MONSTR	Metal oxide nanostructure
Nu	Nusselt number
PET	Poly(ethylene terephthalate)
PMMA	Poly(methyl methacrylate)
PP	Polypropylene
Pr	Prandtl number
PS	Polystyrene
Re	Reynolds number
RH	Relative humidity

continued ...

. . . continued

SEM	Scanning electron microscope
SHGC	Superhydrophobic graphite composite
SHS	Superhydrophobic surfaces
SS	Stainless steel
T	Thermostat
V	Valve
wt	Weight

References

[1] J. Houghton, "Global warming," *Reports on Progress in Physics*, vol. 68, no. 6, pp. 1343–1403, 2005. DOI: 10.1088/0034-4885/68/6/R02.

[2] P. Smith, C. Fang, J. J. Dawson, and J. B. Moncrieff, "Impact of global warming on soil organic carbon," in *Advances in Agronomy Volume 97*, ser. Advances in Agronomy, vol. 97, Elsevier, 2008, pp. 1–43, ISBN: 9780123743527. DOI: 10.1016/S0065-2113(07)00001-6.

[3] R. A. Pielke, C. Landsea, M. Mayfield, J. Layer, and R. Pasch, "Hurricanes and global warming," *Bulletin of the American Meteorological Society*, vol. 86, no. 11, pp. 1571–1576, 2005. DOI: 10.1175/BAMS-86-11-1571.

[4] R. A. Kerr, "Climate change. global warming is changing the world," *Science (New York, N.Y.)*, vol. 316, no. 5822, pp. 188–190, 2007. DOI: 10.1126/science.316.5822.188.

[5] D. A. Lashof and D. R. Ahuja, "Relative contributions of greenhouse gas emissions to global warming," *Nature*, vol. 344, no. 6266, pp. 529–531, 1990. DOI: 10.1038/344529a0.

[6] M. Meinshausen et al., "Greenhouse-gas emission targets for limiting global warming to 2 degrees c," *Nature*, vol. 458, no. 7242, pp. 1158–1162, 2009. DOI: 10.1038/nature08017.

[7] *Advances in Carbon Capture*. Elsevier, 2020, ISBN: 9780128196571. DOI: 10.1016/C2018-0-05339-6.

[8] F. Bauer, J. P. Tilsted, S. Pfister, C. Oberschelp, and V. Kulionis, "Mapping ghg emissions and prospects for renewable energy in the chemical industry," *Current Opinion in Chemical Engineering*, vol. 39, p. 100 881, 2023. DOI: 10.1016/j.coche.2022.100881.

[9] M. Rehfeldt, T. Fleiter, and F. Toro, "A bottom-up estimation of the heating and cooling demand in european industry," *Energy Efficiency*, vol. 11, no. 5, pp. 1057–1082, 2018. DOI: 10.1007/s12053-017-9571-y.

[10] H.-J. Bart and S. Scholl, *Innovative Heat Exchangers*. Cham: Springer International Publishing, 2018, ISBN: 978-3-319-71639-8. DOI: 10.1007/978-3-319-71641-1.

[11] J. G. Cevallos, A. E. Bergles, A. Bar-Cohen, P. Rodgers, and S. K. Gupta, "Polymer heat exchangers—history, opportunities, and challenges," *Heat Transfer Engineering*, vol. 33, no. 13, pp. 1075–1093, 2012. DOI: 10.1080/01457632.2012.663654.

[12] J. B. P. Christmann, L. J. Krätz, and H.-J. Bart, "Novel polymer film heat exchangers for seawater desalination," *Desalination and Water Treatment*, vol. 21, no. 1-3, pp. 162–174, 2010. DOI: 10.5004/dwt.2010.1325.

[13] H. Kiepfer, P. Stannek, M. Grundler, and H.-J. Bart, "Development and thermal performance of a thermoplastic-graphite-composite based plate heat exchanger for use in corrosive media," *Applied Thermal Engineering*, vol. 236, p. 121 581, 2024. DOI: 10.1016/j.applthermaleng.2023.121581.

[14] E. Schmidt, W. Schurig, and W. Sellschopp, "Versuche über die Kondensation von Wasserdampf in Film- und Tropfenform," *Technische Mechanik und Thermodynamik*, vol. 1, no. 2, pp. 53–63, 1930. DOI: 10.1007/BF02641051.

[15] B. Peng, X. Ma, Z. Lan, W. Xu, and R. Wen, "Analysis of condensation heat transfer enhancement with dropwise-filmwise hybrid surface: Droplet sizes effect," *International Journal of Heat and Mass Transfer*, vol. 77, pp. 785–794, 2014. DOI: 10.1016/j.ijheatmasstransfer.2014.05.052.

[16] B. Rezaee, M. Mahlouji Taheri, H. Pakzad, M. Fakhri, A. Moosavi, and M. Aryanpour, "Enhancement of dropwise condensation heat transfer through a sprayable superhydrophobic coating," *Langmuir : the ACS journal of surfaces and colloids*, vol. 39, no. 23, pp. 8354–8366, 2023. DOI: 10.1021/acs.langmuir.3c00947.

[17] Y. Tang, X. Yang, L. Wang, Y. Li, and Di Zhu, "Dropwise condensate comb for enhanced heat transfer," *ACS applied materials & interfaces*, vol. 15, no. 17, pp. 21 549–21 561, 2023. DOI: 10.1021/acsami.2c20874.

[18] T. M. Thomas, P. Sinha Mahapatra, R. Ganguly, and M. K. Tiwari, "Preferred mode of atmospheric water vapor condensation on nanoengineered surfaces: Dropwise or filmwise?" *Langmuir : the ACS journal of surfaces and colloids*, vol. 39, no. 15, pp. 5396–5407, 2023. DOI: 10.1021/acs.langmuir.3c00022.

[19] A. Starostin, V. Valtsifer, Z. Barkay, I. Legchenkova, V. Danchuk, and E. Bormashenko, "Drop-wise and film-wise water condensation processes occurring on metallic micro-scaled surfaces," *Applied Surface Science*, vol. 444, pp. 604–609, 2018. DOI: 10.1016/j.apsusc.2018.03.065.

[20] J. Jeevahan, M. Chandrasekaran, G. Britto Joseph, R. B. Durairaj, and G. Mageshwaran, "Superhydrophobic surfaces: A review on fundamentals, applications, and challenges," *Journal of Coatings Technology and Research*, vol. 15, no. 2, pp. 231–250, 2018. DOI: 10.1007/s11998-017-0011-x.

[21] R. S. Voronov, D. V. Papavassiliou, and L. L. Lee, "Review of fluid slip over superhydrophobic surfaces and its dependence on the contact angle," *Industrial & Engineering Chemistry Research*, vol. 47, no. 8, pp. 2455–2477, 2008. DOI: 10.1021/ie0712941.

[22] M. Santhakumari and N. Sagar, "A review of the environmental factors degrading the performance of silicon wafer-based photovoltaic modules: Failure detection methods and essential mitigation techniques," *Renewable and Sustainable Energy Reviews*, vol. 110, pp. 83–100, 2019. DOI: 10.1016/j.rser.2019.04.024.

[23] H. Y. Erbil and C. E. Cansoy, "Range of applicability of the wenzel and cassie-baxter equations for superhydrophobic surfaces," *Langmuir : the ACS journal of surfaces and colloids*, vol. 25, no. 24, pp. 14 135–14 145, 2009. DOI: 10.1021/la902098a.

[24] G. McHale, N. J. Shirtcliffe, and M. I. Newton, "Contact-angle hysteresis on superhydrophobic surfaces," *Langmuir : the ACS journal of surfaces and colloids*, vol. 20, no. 23, pp. 10 146–10 149, 2004. DOI: 10.1021/la0486584.

[25] H. J. Ensikat, P. Ditsche-Kuru, C. Neinhuis, and W. Barthlott, "Superhydrophobicity in perfection: The outstanding properties of the lotus leaf," *Beilstein journal of nanotechnology*, vol. 2, pp. 152–161, 2011. DOI: 10.3762/bjnano.2.19.

[26] M. A. Samaha, H. V. Tafreshi, and M. Gad-el-Hak, "Superhydrophobic surfaces: From the lotus leaf to the submarine," *Comptes Rendus. Mécanique*, vol. 340, no. 1-2, pp. 18–34, 2012. DOI: 10.1016/j.crme.2011.11.002.

[27] S. S. Latthe, C. Terashima, K. Nakata, and A. Fujishima, "Superhydrophobic surfaces developed by mimicking hierarchical surface morphology of lotus leaf," *Molecules (Basel, Switzerland)*, vol. 19, no. 4, pp. 4256–4283, 2014. DOI: 10.3390/molecules19044256.

[28] C. W. Berendsen, M. Škereň, D. Najdek, and F. Černý, "Superhydrophobic surface structures in thermoplastic polymers by interference lithography and thermal imprinting," *Applied Surface Science*, vol. 255, no. 23, pp. 9305–9310, 2009. DOI: 10.1016/j.apsusc.2009.07.001.

[29] Y.-C. Lin, S.-H. Hsu, and Y.-C. Chung, "Thermal imprint techniques for preparation of superhydrophobic polymer coatings," *Surface and Coatings Technology*, vol. 231, pp. 501–506, 2013. DOI: 10.1016/j.surfcoat.2012.01.015.

[30] J. Durret, P.-D. Szkutnik, N. Frolet, S. Labau, and C. Gourgon, "Superhydrophobic polymeric films with hierarchical structures produced by nanoimprint (nil) and plasma roughening," *Applied Surface Science*, vol. 445, pp. 97–106, 2018. DOI: 10.1016/j.apsusc.2018.03.010.

[31] Z. Zhan et al., "Creating superhydrophobic polymer surfaces with superstrong resistance to harsh cleaning and mechanical abrasion fabricated by scalable one–step thermal–imprinting," *Advanced Materials Interfaces*, vol. 6, no. 16, 2019. DOI: 10.1002/admi.201900240.

[32] N. S. Saadi, L. B. Hassan, and T. Karabacak, "Metal oxide nanostructures by a simple hot water treatment," *Scientific reports*, vol. 7, no. 1, p. 7158, 2017. DOI: 10.1038/s41598-017-07783-8.

[33] P. Yi, H. Wu, C. Zhang, L. Peng, and X. Lai, "Roll-to-roll uv imprinting lithography for micro/nanostructures," *Journal of Vacuum Science & Technology B, Nanotechnology and Microelectronics: Materials, Processing, Measurement, and Phenomena*, vol. 33, no. 6, 2015. DOI: 10.1116/1.4933347.

[34] R. Raab, D. Fotachov, E. Oesterschulze, T. Melchior, E. von Harbou, and H.-J. Bart, "Hierarchical structured superhydrophobic surfaces on graphite composites: Preprint," *Applied Polymer Science*, vol. 2024, [Online]. Available: https://zenodo.org/records/14514715.

[35] J. Wang, Z. Ma, G. Li, B. Sundén, and J. Yan, "Improved modeling of heat transfer in dropwise condensation," *International Journal of Heat and Mass Transfer*, vol. 155, p. 119 719, 2020. DOI: 10.1016/j.ijheatmasstransfer.2020.119719.

[36] M. Tancon et al., "Simultaneous measurement of heat flux and droplet population during dropwise condensation from humid air flowing on a vertical surface," *Experimental Thermal and Fluid Science*, vol. 136, p. 110 677, 2022. DOI: 10.1016/j.expthermflusci.2022.110677.

[37] M. Ma and R. M. Hill, "Superhydrophobic surfaces," *Current Opinion in Colloid & Interface Science*, vol. 11, no. 4, pp. 193–202, 2006. DOI: 10.1016/j.cocis.2006.06.002.

[38] A. Synytska, L. Ionov, V. Dutschk, M. Stamm, and K. Grundke, "Wetting on regularly structured surfaces from "core-shell" particles: Theoretical predictions and experimental findings," *Langmuir : the ACS journal of surfaces and colloids*, vol. 24, no. 20, pp. 11 895–11 901, 2008. DOI: 10.1021/la8010585.

[39] W. Barthlott, Z. Cerman, and A. K. Stosch, "Der lotus–effekt: Selbstreinigende oberflächen und ihre übertragung in die technik," *Biologie in unserer Zeit*, vol. 34, no. 5, pp. 290–296, 2004. DOI: 10.1002/biuz.200410260.

[40] M. Zhang, S. Feng, L. Wang, and Y. Zheng, "Lotus effect in wetting and self-cleaning," *Biotribology*, vol. 5, pp. 31–43, 2016. DOI: 10.1016/j.biotri.2015.08.002.

[41] Y. Lu, S. Sathasivam, J. Song, C. R. Crick, C. J. Carmalt, and I. P. Parkin, "Repellent materials. robust self-cleaning surfaces that function when exposed to either air or oil," *Science (New York, N.Y.)*, vol. 347, no. 6226, pp. 1132–1135, 2015. DOI: 10.1126/science.aaa0946.

[42] W. Bo et al., "Advances in superhydrophobic material research: From preparation to electrified railway protection," *RSC advances*, vol. 14, no. 17, pp. 12 204–12 217, 2024. DOI: 10.1039/D3RA08180J.

[43] M. Yang et al., "Robust fabrication of superhydrophobic and photocatalytic self-cleaning cotton textile based on tio2 and fluoroalkylsilane," *Journal of Materials Science*, vol. 54, no. 3, pp. 2079–2092, 2019. DOI: 10.1007/s10853-018-3001-1.

[44] L. Cao, A. K. Jones, V. K. Sikka, J. Wu, and Di Gao, "Anti-icing superhydrophobic coatings," *Langmuir : the ACS journal of surfaces and colloids*, vol. 25, no. 21, pp. 12 444–12 448, 2009. DOI: 10.1021/la902882b.

[45] G. Fang and A. Amirfazli, "Understanding the anti-icing behavior of superhydrophobic surfaces," *Surface Innovations*, vol. 2, no. 2, pp. 94–102, 2014. DOI: 10.1680/si.13.00046.

[46] S. M. Kang, K. Kim, S. Kim, D. G. Lee, T. An, and G. H. Kim, "Synthesis of hierarchical superhydrophilic/superhydrophobic nanostructured surfaces for oil/water separation," *Advanced Materials Interfaces*, vol. 11, no. 9, 2024. DOI: 10.1002/admi.202300627.

[47] Y. Wang et al., "Sustainable superhydrophobic surface with tunable nanoscale hydrophilicity for water harvesting applications," *Angewandte Chemie*, vol. 134, no. 10, 2022. DOI: 10.1002/ange.202115238.

[48] T. Pfeiffer, M. Kappl, H.-J. Butt, P. Stephan, and T. Gambaryan-Roisman, "Condensation of water on pdms-coated copper surfaces for fresh water harvesting," *Journal of Physics: Conference Series*, vol. 2766, no. 1, p. 012 119, 2024. DOI: 10.1088/1742-6596/2766/1/012119.

[49] H. Y. Wong et al., "Superhydrophobic surface designing for efficient atmospheric water harvesting aided by intelligent computer vision," *ACS applied materials & interfaces*, vol. 15, no. 21, pp. 25 849–25 859, 2023. DOI: 10.1021/acsami.3c03436.

[50] Y.-L. Wu, J.-W. Zheng, M. Muneeshwaran, K.-S. Yang, and C.-C. Wang, "Moist air condensation heat transfer enhancement via superhydrophobicity," *International Journal of Heat and Mass Transfer*, vol. 182, p. 121 973, 2022. DOI: 10.1016/j.ijheatmasstransfer.2021.121973.

[51] X. Wang, B. Xu, Q. Liu, Y. Yang, and Z. Chen, "Enhancement of vapor condensation heat transfer on the micro- and nano-structured superhydrophobic surfaces," *International Journal of Heat and Mass Transfer*, vol. 177, p. 121 526, 2021. DOI: 10.1016/j.ijheatmasstransfer.2021.121526.

[52] M. Ferrari and A. Benedetti, "Superhydrophobic surfaces for applications in seawater," *Advances in colloid and interface science*, vol. 222, pp. 291–304, 2015. DOI: 10.1016/j.cis.2015.01.005.

[53] R. Qi, L. Lu, H. Yang, and F. Qin, "Investigation on wetted area and film thickness for falling film liquid desiccant regeneration system," *Applied Energy*, vol. 112, pp. 93–101, 2013. DOI: 10.1016/j.apenergy.2013.05.083.

[54] B. Köroğlu, N. Bogan, and C. Park, "Effects of tube row on heat transfer and surface wetting of microscale porous-layer coated, horizontal-tube, falling-film evaporator," *Journal of Heat Transfer*, vol. 135, no. 4, 2013. DOI: 10.1115/1.4023014.

[55] E. Lee and D. H. Kim, "Simple fabrication of asphalt-based superhydrophobic surface with controllable wetting transition from cassie-baxter to wenzel wetting state," *Colloids and Surfaces A: Physicochemical and Engineering Aspects*, vol. 625, p. 126 927, 2021. DOI: 10.1016/j.colsurfa.2021.126927.

[56] Y. Xiao, Y. Zhang, Y. Yan, Z. Guo, J. Liu, and W. Can, "Study of wettability transition on hierarchical structured aluminum cut by wire electric discharge machining," *Colloids and Surfaces A: Physicochemical and Engineering Aspects*, vol. 627, p. 127 200, 2021. DOI: 10.1016/j.colsurfa.2021.127200.

[57] S. Milles, M. Soldera, T. Kuntze, and A. F. Lasagni, "Characterization of self-cleaning properties on superhydrophobic aluminum surfaces fabricated by direct laser writing and direct laser interference patterning," *Applied Surface Science*, vol. 525, p. 146 518, 2020. DOI: 10.1016/j.apsusc.2020.146518.

[58] B. Liu, Y. He, Y. Fan, and X. Wang, "Fabricating super–hydrophobic lotus–leaf–like surfaces through soft–lithographic imprinting," *Macromolecular Rapid Communications*, vol. 27, no. 21, pp. 1859–1864, 2006. DOI: 10.1002/marc.200600492.

[59] J. Feng, M. T. Tuominen, and J. P. Rothstein, "Hierarchical superhydrophobic surfaces fabricated by dual–scale electron–beam–lithography with well–ordered secondary nanostructures," *Advanced functional materials*, vol. 21, no. 19, pp. 3715–3722, 2011. DOI: 10.1002/adfm.201100665.

[60] Y. He, C. Jiang, H. Yin, J. Chen, and W. Yuan, "Superhydrophobic silicon surfaces with micro-nano hierarchical structures via deep reactive ion etching and galvanic etching," *Journal of colloid and interface science*, vol. 364, no. 1, pp. 219–229, 2011. DOI: 10.1016/j.jcis.2011.07.030.

[61] R. Liao, Z. Zuo, C. Guo, Y. Yuan, and A. Zhuang, "Fabrication of superhydrophobic surface on aluminum by continuous chemical etching and its anti-icing property," *Applied Surface Science*, vol. 317, pp. 701–709, 2014. DOI: 10.1016/j.apsusc.2014.08.187.

[62] V. S. Saji, "Electrophoretic-deposited superhydrophobic coatings," *Chemistry, an Asian journal*, vol. 16, no. 5, pp. 474–491, 2021. DOI: 10.1002/asia.202001425.

[63] Y. Lin, R. Zhou, and J. Xu, "Superhydrophobic surfaces based on fractal and hierarchical microstructures using two–photon polymerization: Toward flexible superhydrophobic films," *Advanced Materials Interfaces*, vol. 5, no. 21, 2018. DOI: 10.1002/admi.201801126.

[64] D. Fotachov and E. Oesterschulze, "Self-draining microchannel surface structure for droplet condensation with controlled droplet radius distribution," *International Journal of Heat and Mass Transfer*, vol. 234, p. 126 105, 2024. DOI: 10.1016/j.ijheatmasstransfer.2024.126105.

[65] C. Bethke, R. Adelung, and S. Schwarzer, "Generierung einer mikro– und nanostrukturierten kupferoberfläche mit lotos–effekt – ein versuch für die sekundarstufen i und ii," *CHEMKON*, vol. 24, no. 1, pp. 31–38, 2017. DOI: 10.1002/ckon.201710290.

[66] A. R. Lotz, "Studien zur nanostrukturierung von aluminium-oberflächen mittels elektrochemischer methoden," Ph.D. dissertation, Universitätsbibliothek Gießen, 2009. DOI: 10.22029/jlupub-10141.

[67] Z. Rahimi-Ahar, M. S. Hatamipour, and L. R. Ahar, "Air humidification-dehumidification process for desalination: A review," *Progress in Energy and Combustion Science*, vol. 80, p. 100 850, 2020. DOI: 10.1016/j.pecs.2020.100850.

[68] X. Li, G. Yuan, Z. Wang, H. Li, and Z. Xu, "Experimental study on a humidification and dehumidification desalination system of solar air heater with evacuated tubes," *Desalination*, vol. 351, pp. 1–8, 2014. DOI: 10.1016/j.desal.2014.07.008.

[69] T. Ming, T. Gong, R. K. de Richter, Y. Wu, and W. Liu, "A moist air condensing device for sustainable energy production and water generation," *Energy Conversion and Management*, vol. 138, pp. 638–650, 2017. DOI: 10.1016/j.enconman.2017.02.012.

[70] K. DAOU, R. WANG, and Z. XIA, "Desiccant cooling air conditioning: A review," *Renewable and Sustainable Energy Reviews*, vol. 10, no. 2, pp. 55–77, 2006. DOI: 10.1016/j.rser.2004.09.010.

[71] A. W. Kandeal et al., "Research progress on recent technologies of water harvesting from atmospheric air: A detailed review," *Sustainable Energy Technologies and Assessments*, vol. 52, p. 102 000, 2022. DOI: 10.1016/j.seta.2022.102000.

[72] W. Lu, W. L. Ong, and G. W. Ho, "Advances in harvesting water and energy from ubiquitous atmospheric moisture," *Journal of Materials Chemistry A*, vol. 11, no. 24, pp. 12 456–12 481, 2023. DOI: 10.1039/D2TA09552A.

[73] X. Liu, D. Beysens, and T. Bourouina, "Water harvesting from air: Current passive approaches and outlook," *ACS Materials Letters*, vol. 4, no. 5, pp. 1003–1024, 2022. DOI: 10.1021/acsmaterialslett.1c00850.

[74] P. Stephan, S. Kabelac, M. Kind, D. Mewes, K. Schaber, and T. Wetzel, Eds., *VDI-Wärmeatlas: 483 Tabellen* (Springer Reference Technik), 12. Auflage. Berlin: Springer Vieweg, 2019, ISBN: 978-3-662-52988-1.

[75] N. Miljkovic, R. Enright, and E. N. Wang, "Effect of droplet morphology on growth dynamics and heat transfer during condensation on superhydrophobic nanostructured surfaces," *ACS nano*, vol. 6, no. 2, pp. 1776–1785, 2012. DOI: 10.1021/nn205052a.

[76] N. Miljkovic et al., "Jumping-droplet-enhanced condensation on scalable superhydrophobic nanostructured surfaces," *Nano letters*, vol. 13, no. 1, pp. 179–187, 2013. DOI: 10.1021/nl303835d.

[77] L. Yin, Y. Wang, J. Ding, Q. Wang, and Q. Chen, "Water condensation on superhydrophobic aluminum surfaces with different low-surface-energy coatings," *Applied Surface Science*, vol. 258, no. 8, pp. 4063–4068, 2012. DOI: 10.1016/j.apsusc.2011.12.100.

[78] M. Ahlers, A. Buck-Emden, and H.-J. Bart, "Is dropwise condensation feasible? a review on surface modifications for continuous dropwise condensation and a profitability analysis," *Journal of advanced research*, vol. 16, pp. 1–13, 2019. DOI: 10.1016/j.jare.2018.11.004.

[79] T. Ashworth and D. R. Smith, Eds., *Thermal Conductivity 18*. Boston, MA: Springer US, 1985, ISBN: 978-1-4684-4918-1. DOI: 10.1007/978-1-4684-4916-7.

[80] D. Fotachov, R. Raab, H.-J. Bart, and E. Oesterschulze, "Drainage during condensation on microgrooved biphilic surfaces," *Langmuir : the ACS journal of surfaces and colloids*, vol. 40, no. 2, pp. 1195–1202, 2024. DOI: 10.1021/acs.langmuir.3c02433.

[81] K. Kurogi, H. Yan, and K. Tsujii, "Importance of pinning effect of wetting in super water-repellent surfaces," *Colloids and Surfaces A: Physicochemical and Engineering Aspects*, vol. 317, no. 1-3, pp. 592–597, 2008. DOI: 10.1016/j.colsurfa.2007.11.048.

[82] J. Sun and P. B. Weisensee, "Microdroplet self-propulsion during dropwise condensation on lubricant-infused surfaces," *Soft matter*, vol. 15, no. 24, pp. 4808–4817, 2019. DOI: 10.1039/C9SM00493A.

[83] J. Wang, Z. Ma, G. Li, B. Sundén, and J. Yan, "Improved modeling of heat transfer in dropwise condensation," *International Journal of Heat and Mass Transfer*, vol. 155, p. 119 719, 2020.

[84] M. Tancon et al., "Simultaneous measurement of heat flux and droplet population during dropwise condensation from humid air flowing on a vertical surface," *Experimental Thermal and Fluid Science*, vol. 136, p. 110 677, 2022.

[85] H.-J. Bart and S. Scholl, *Innovative Wärmetauscher*. Springer, 2023.

[86] H. Kiepfer, "Development characterization and performance evaluation of thermoplastic-graphite based plate heat exchangers," Ph.D. dissertation, Rheinland-Pfälzische Technische Universität Kaiserslautern-Landau, 2024.

[87] F. Chu and X. Wu, "Fabrication and condensation characteristics of metallic superhydrophobic surface with hierarchical micro-nano structures," *Applied Surface Science*, vol. 371, pp. 322–328, 2016.

[88] D. Ramkrishna, *Population balances: Theory and applications to particulate systems in engineering*. Elsevier, 2000.

[89] D. Fotachov, R. Raab, H.-J. Bart, and E. Oesterschulze, "Drainage during condensation on microgrooved biphilic surfaces," *Langmuir*, vol. 40, no. 2, pp. 1195–1202, 2023.

[90] E. Davis, "A history and state-of-the-art of accommodation coefficients," *Atmospheric research*, vol. 82, no. 3-4, pp. 561–578, 2006.

[91] H. W. Wen and R. M. Jer, "On the heat transfer in dropwise condensation," *The chemical engineering journal*, vol. 12, no. 3, pp. 225–231, 1976.

[92] L. Cheng and L. Junming, "Laminar forced convection heat and mass transfer of humid air across a vertical plate with condensation," *Chinese Journal of Chemical Engineering*, vol. 19, no. 6, pp. 944–954, 2011.

[93] V. D. I. V.-G. V. und Chemieingenieurwesen (GVC), *Vdi-Wärmeatlas*. Springer, 2006.

[94] R. A. S. of Heating, A. C. Engineers, and G. Atlanta, *ASHRAE handbook: fundamentals*. ASHRAE, 2009.

[95] C. Graham and P. Griffith, "Drop size distributions and heat transfer in dropwise condensation," *International Journal of Heat and Mass Transfer*, vol. 16, no. 2, pp. 337–346, 1973.

[96] V. Baghel, B. S. Sikarwar, and K. Muralidhar, "Dropwise condensation from moist air over a hydrophobic metallic substrate," *Applied Thermal Engineering*, vol. 181, p. 115 733, 2020.

[97] S. Zheng, F. Eimann, C. Philipp, T. Fieback, and U. Gross, "Experimental and modeling investigations of dropwise condensation out of convective humid air flow," *International Journal of Heat and Mass Transfer*, vol. 151, p. 119 349, 2020.

[98] L. Allen, A. O'Connell, and V. Kiermer, "How can we ensure visibility and diversity in research contributions? how the contributor role taxonomy (credit) is helping the shift from authorship to contributorship," *Learned Publishing*, vol. 32, no. 1, pp. 71–74, 2019. DOI: 10.1002/leap.1210.

Supporting Information

Supporting Information for Chapter 2

Confocal microscope measurements various thermal imprinted graphite composites

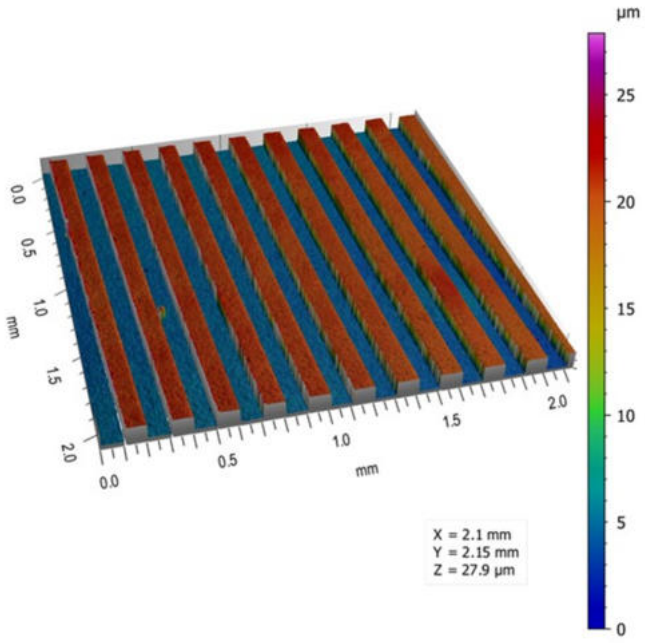

Figure 1: 3D profile of a 100 µm strip structured thermal imprinted graphite composite captured by a confocal microscope.

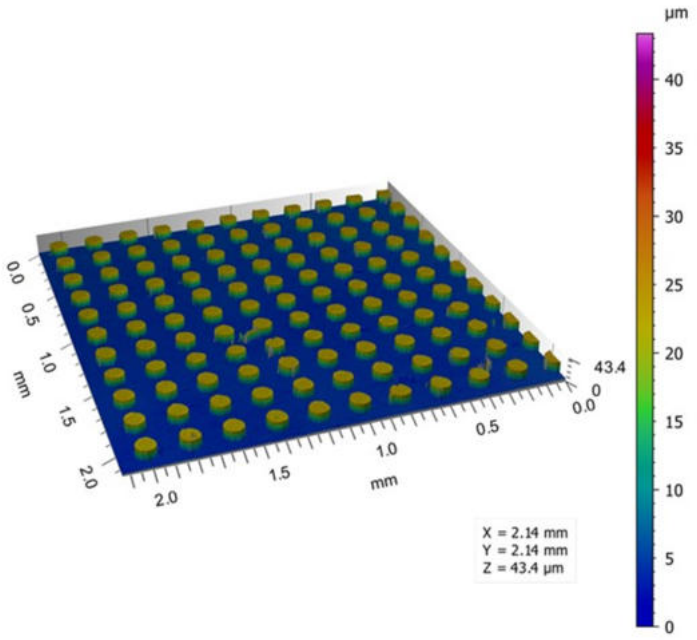

Figure 2: 3D profile of a cylindrical structured thermal imprinted graphite composite captured by a confocal microscope.

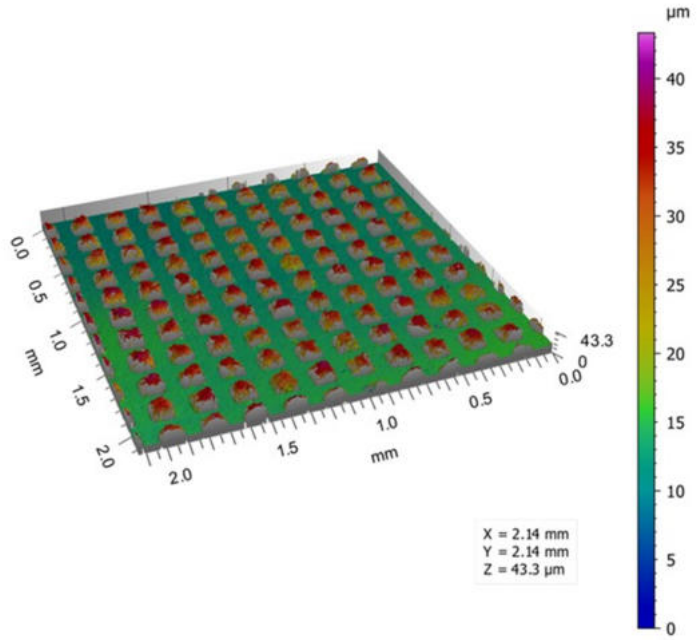

Figure 3: 3D profile of a half-rounded square columns structured thermal imprinted graphite composite captured by a confocal microscope.

Confocal microscope measurements silicon molds

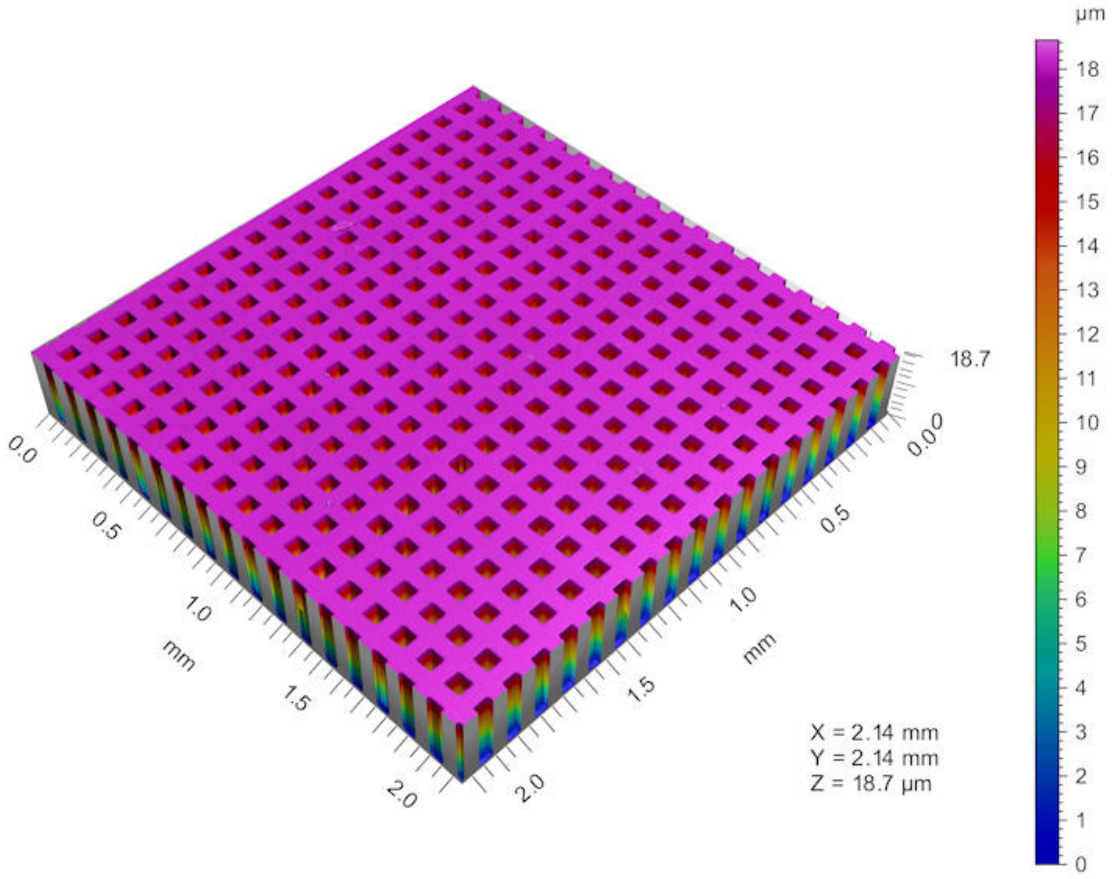

Figure 4: 3D profile of the 60 µm structured silicon wafer captured by a confocal microscope.

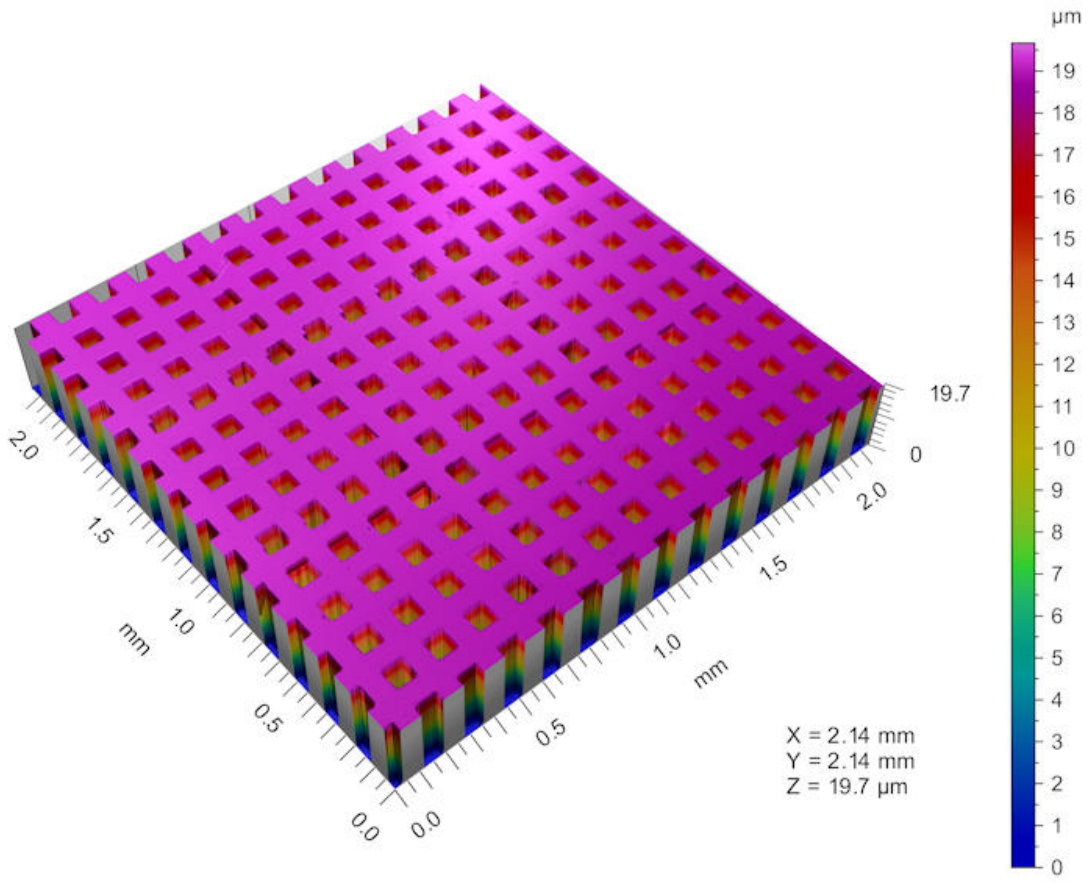

Figure 5: 3D profile of the 80 µm structured silicon wafer captured by a confocal microscope.

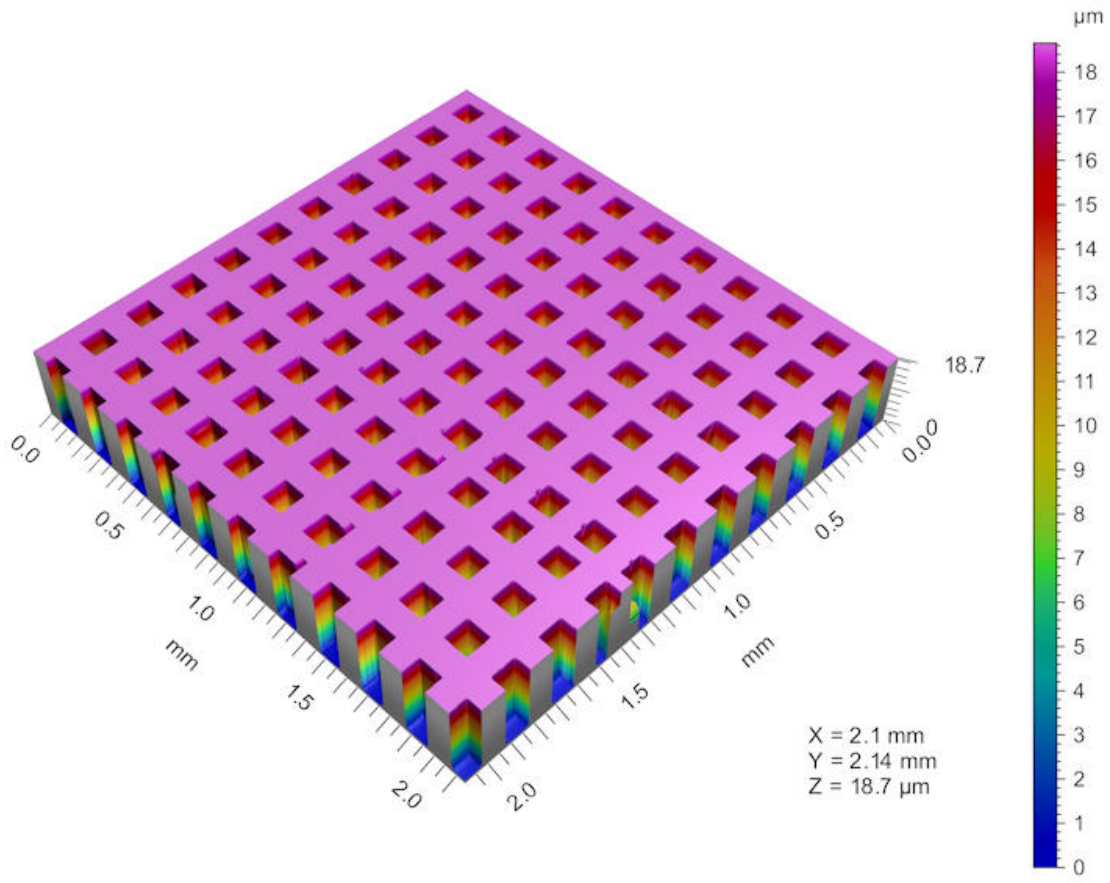

Figure 6: 3D profile of the 100 µm structured silicon wafer captured by a confocal microscope.

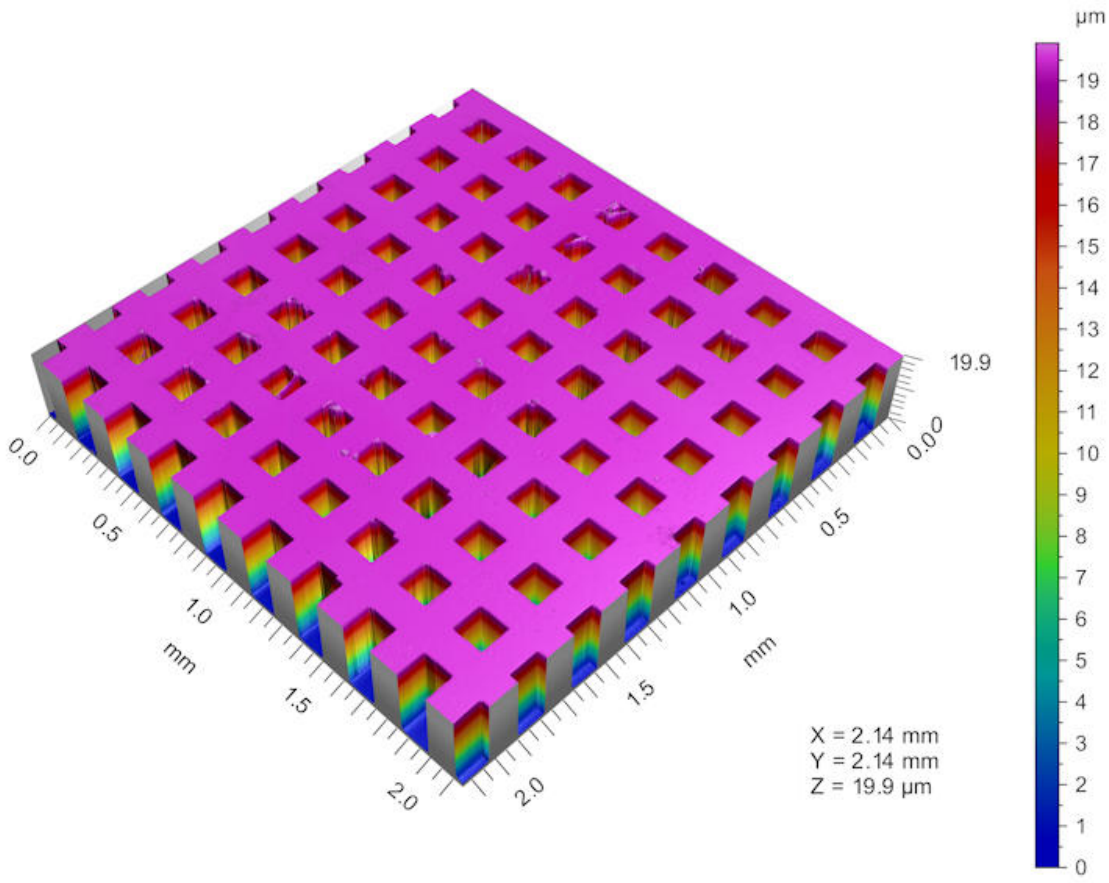

Figure 7: 3D profile of the 120 µm structured silicon wafer captured by a confocal microscope.

Cross-section measurements silicon molds

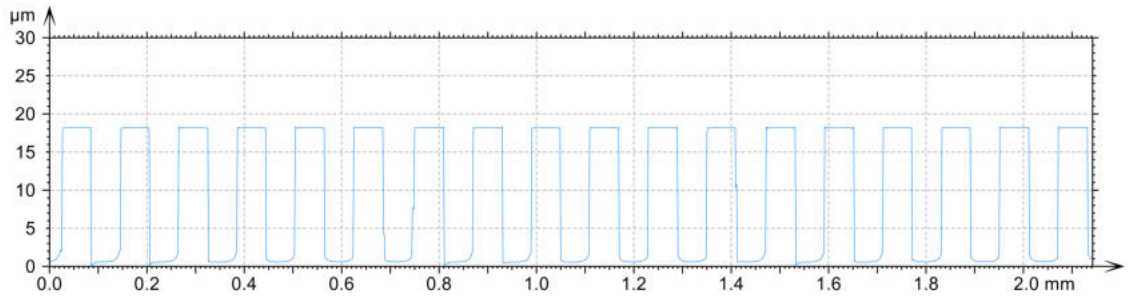

Parameter	Wert	Einheit
Länge	2.14	mm

Figure 8: Cross-section measurement of the 60 µm structured silicon wafer captured by a confocal microscope.

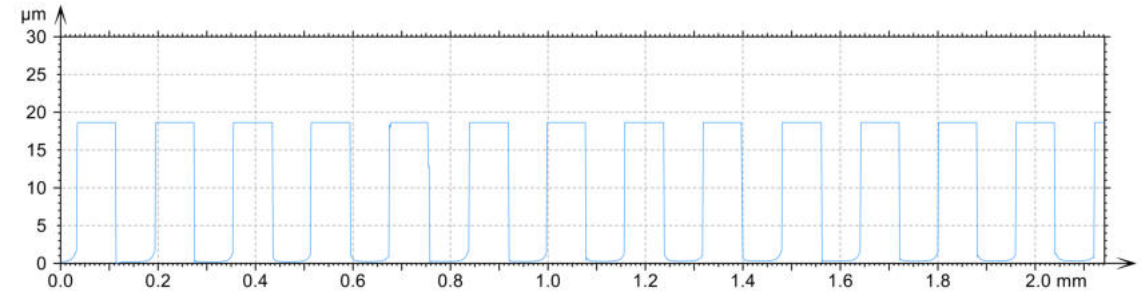

Parameter	Wert	Einheit
Länge	2.14	mm

Figure 9: Cross-section measurement of the 80 µm structured silicon wafer captured by a confocal microscope.

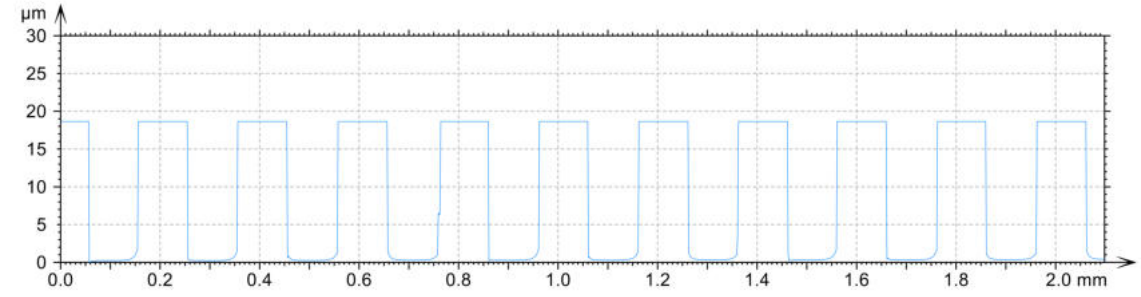

Parameter	Wert	Einheit
Länge	2.10	mm

Figure 10: Cross-section measurement of the 100 µm structured silicon wafer captured by a confocal microscope.

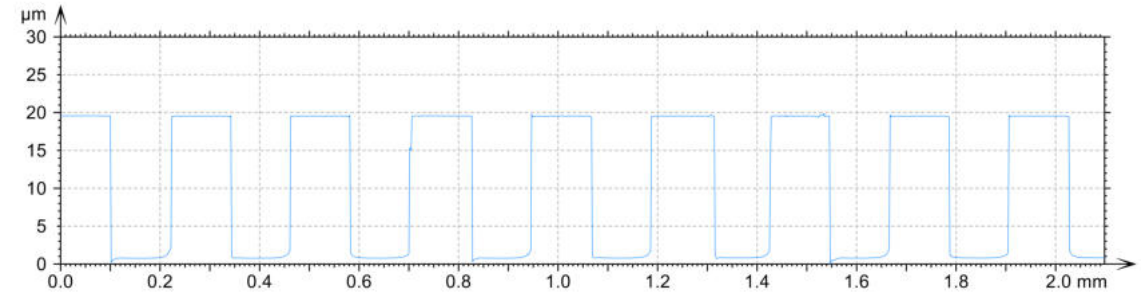

Parameter	Wert	Einheit
Länge	2.10	mm

Figure 11: Cross-section measurement of the 120 µm structured silicon wafer captured by a confocal microscope.

Confocal microscope measurements thermally imprinted graphite compounds

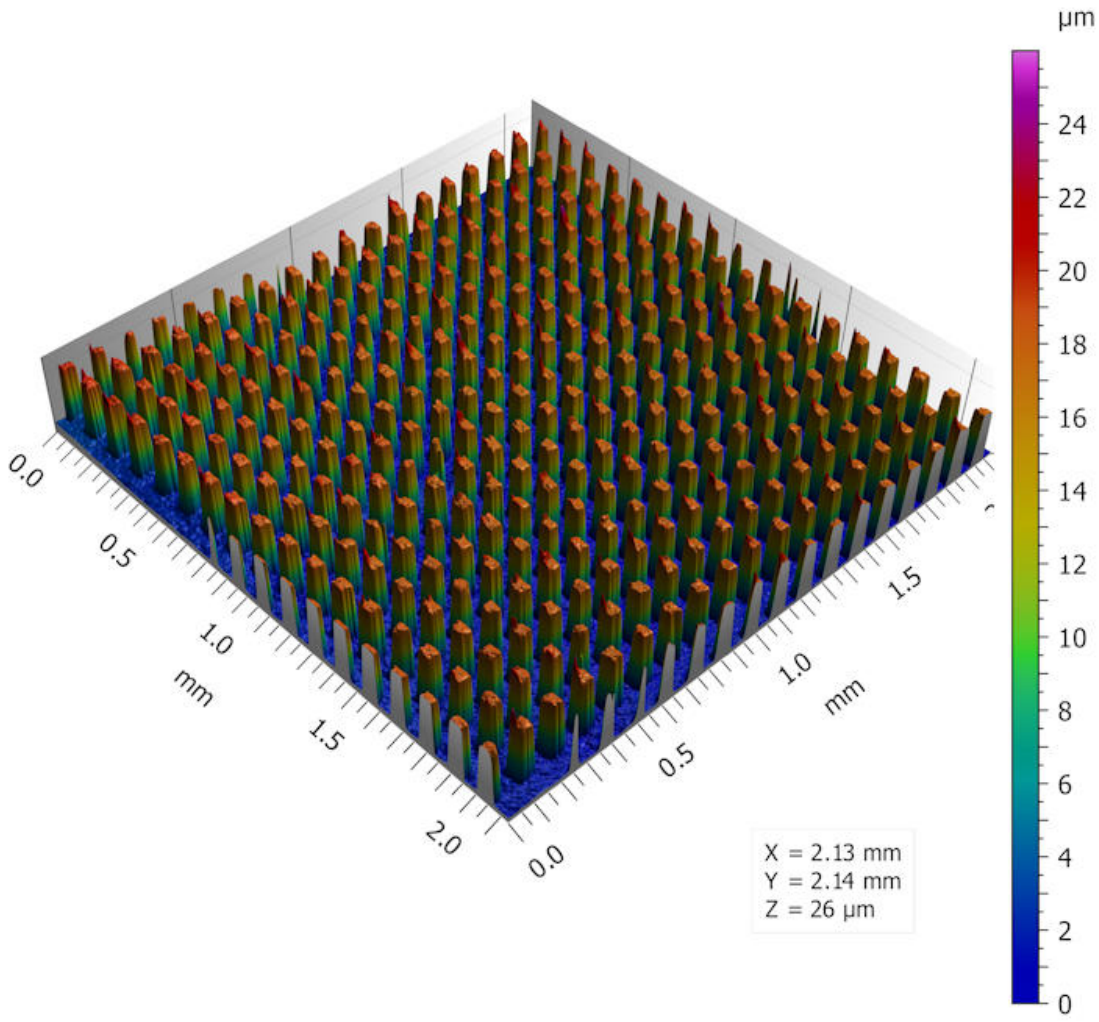

Figure 12: 3D profile of the embossed 60 µm structured graphite compound captured by a confocal microscope.

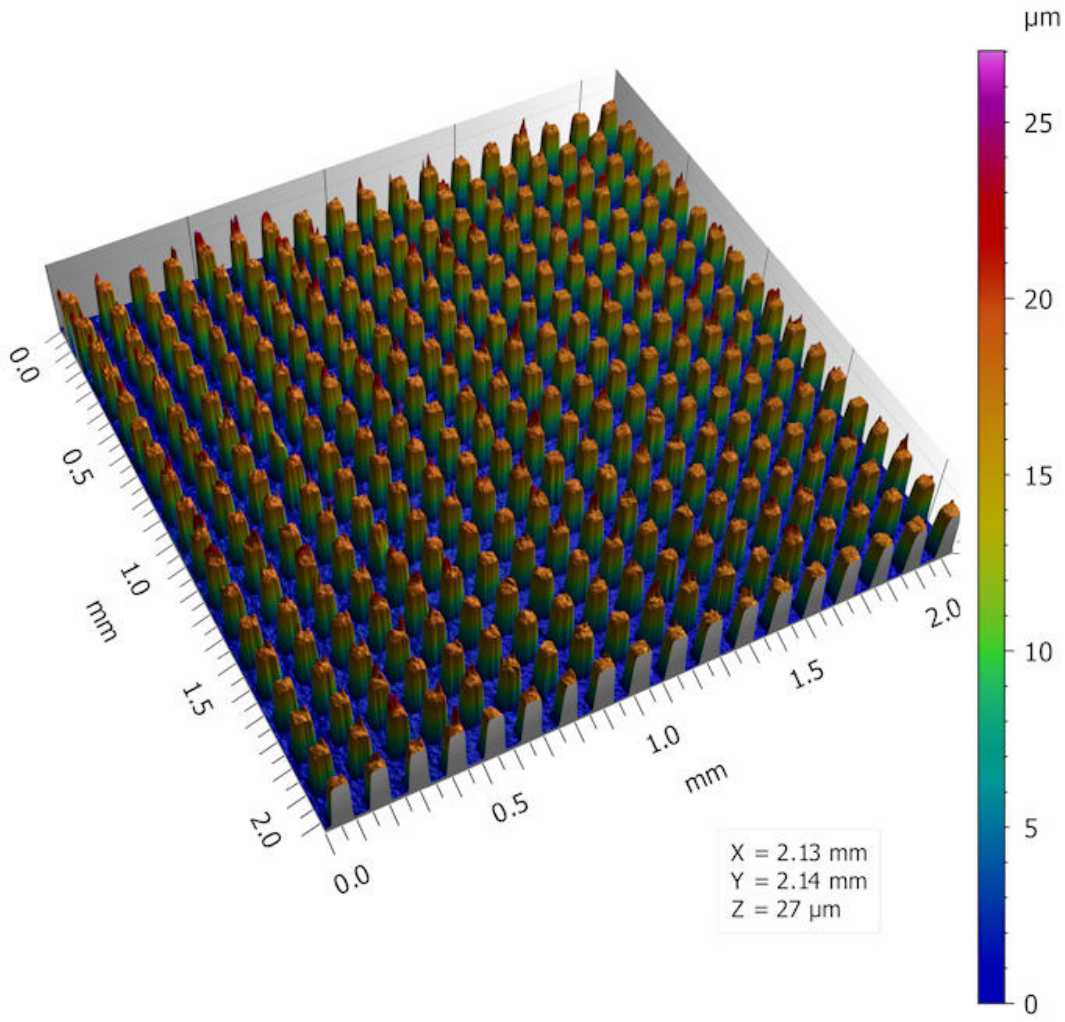

Figure 13: 3D profile of the second embossed 60 µm structured graphite compound captured by a confocal microscope.

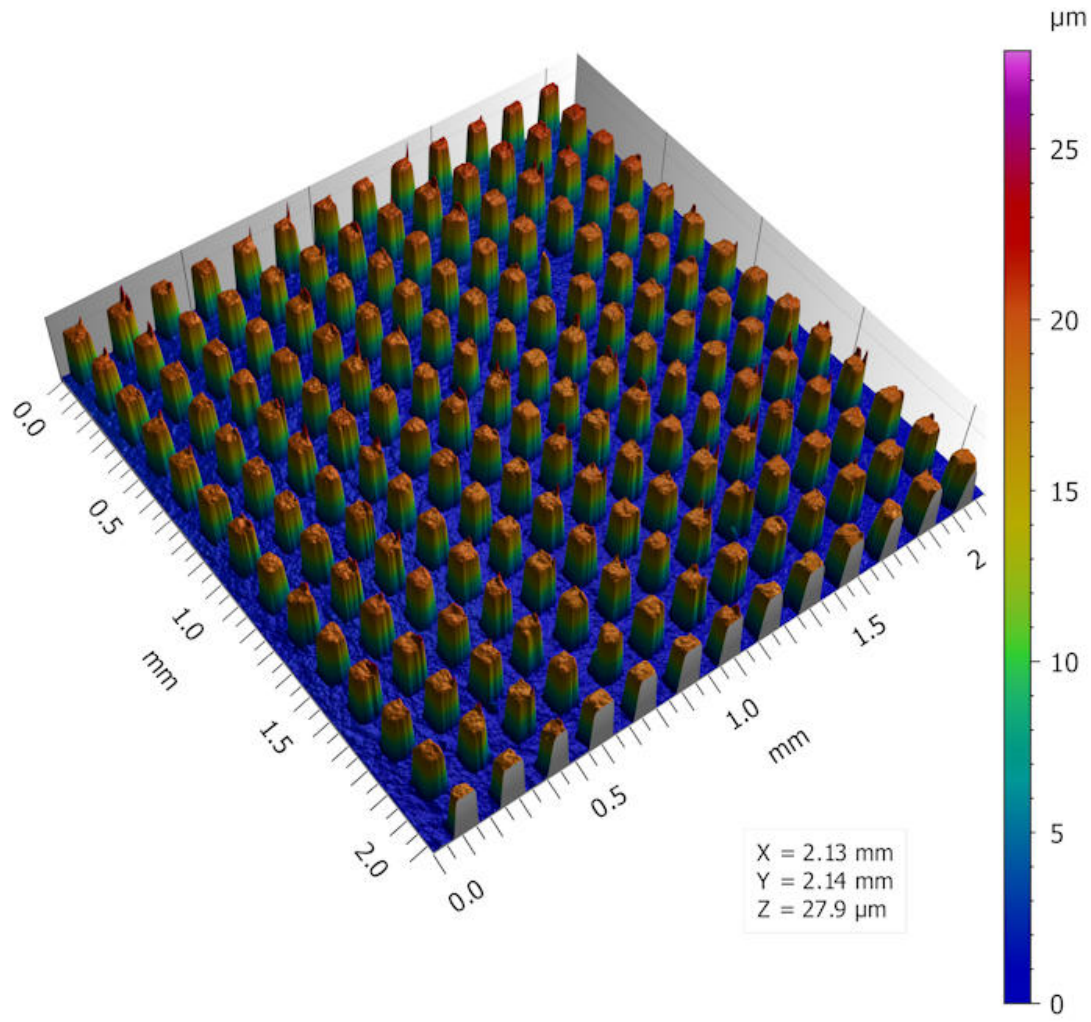

Figure 14: 3D profile of the embossed 80 µm structured graphite compound captured by a confocal microscope.

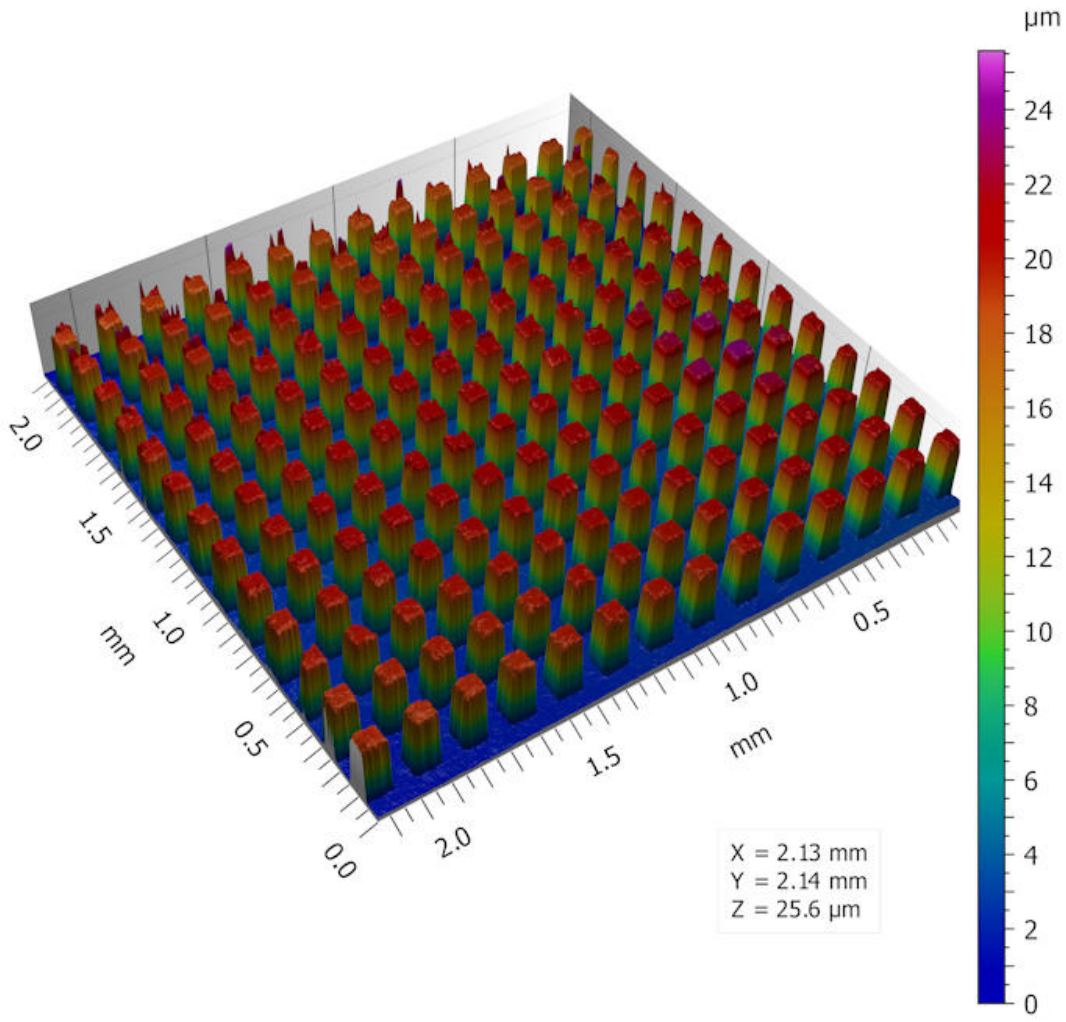

Figure 15: 3D profile of the second embossed 80 µm structured graphite compound captured by a confocal microscope.

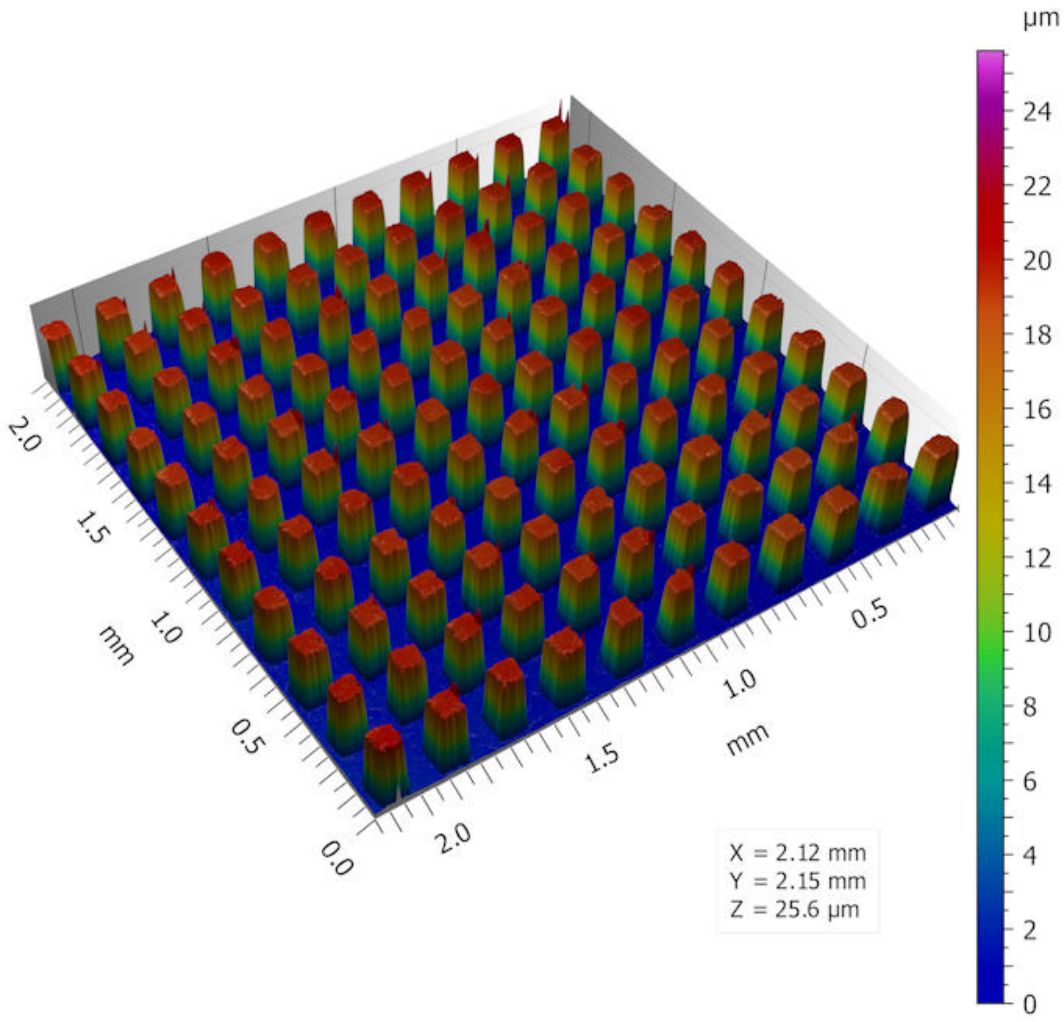

Figure 16: 3D profile of the embossed 100 µm structured graphite compound captured by a confocal microscope.

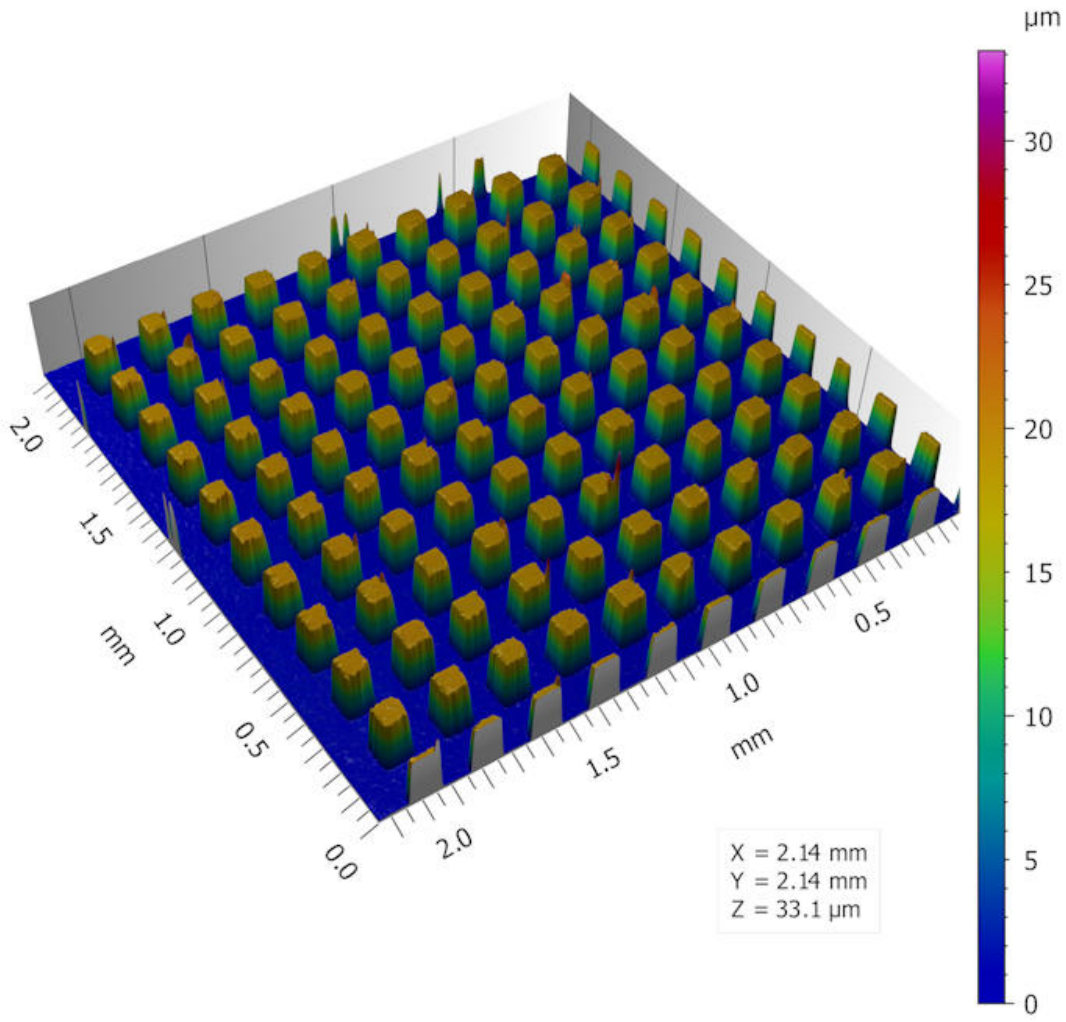

Figure 17: 3D profile of the second embossed 100 µm structured graphite compound captured by a confocal microscope.

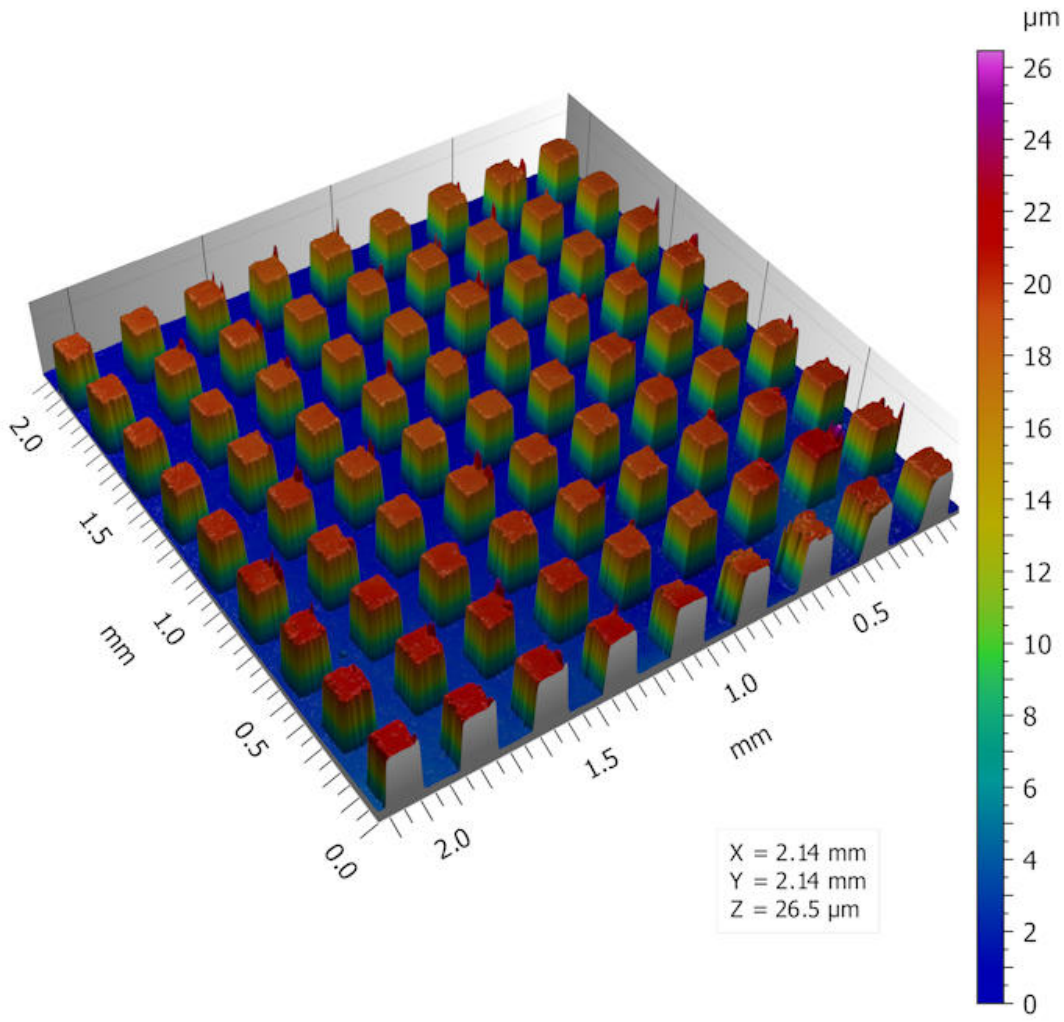

Figure 18: 3D profile of the embossed 120 µm structured graphite compound captured by a confocal microscope.

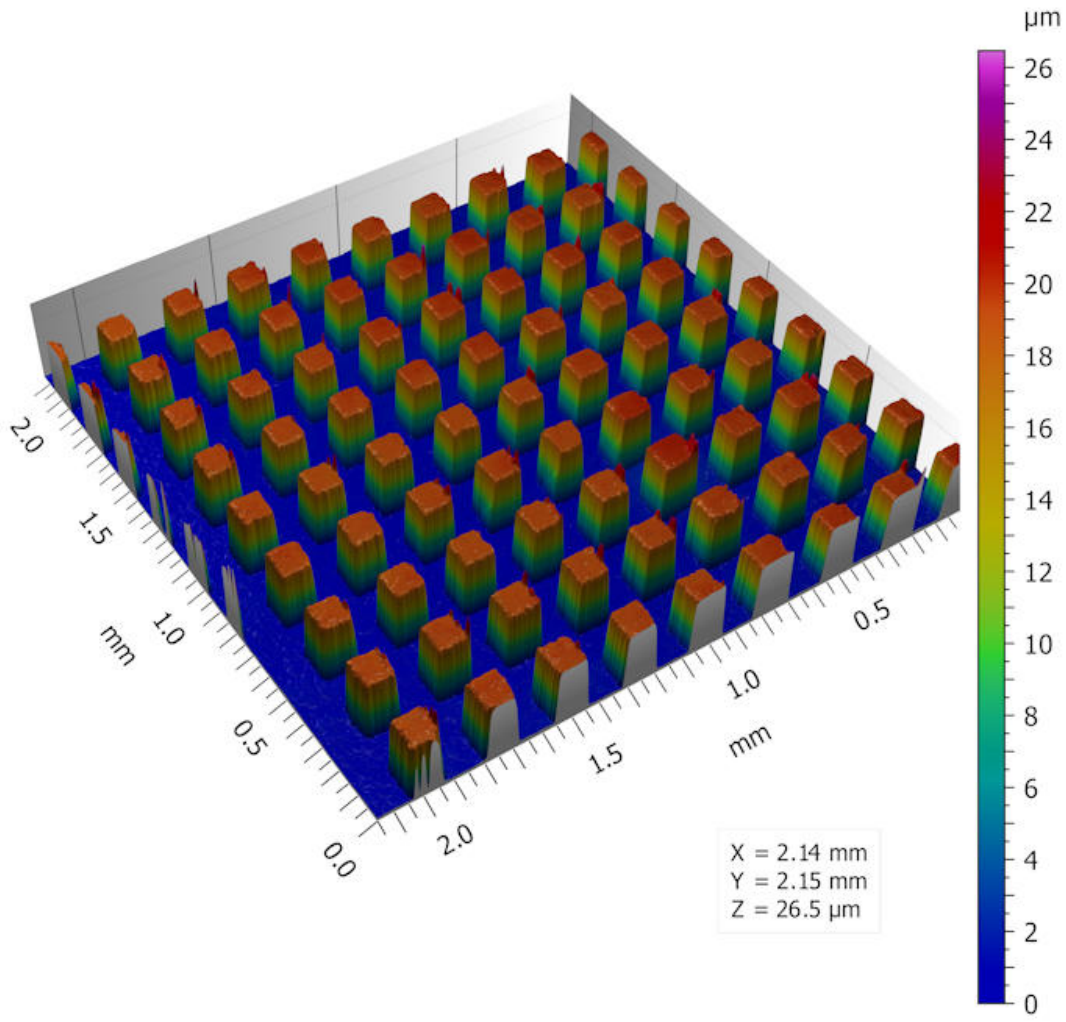

Figure 19: 3D profile of the second embossed 120 µm structured graphite compound captured by a confocal microscope.

Cross-section measurements thermally imprinted graphite compounds

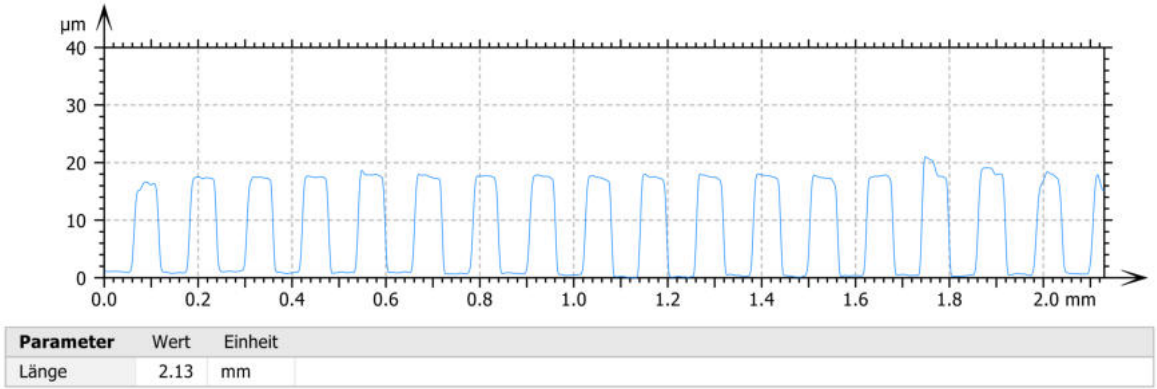

Figure 20: Cross-section measurement of the 60 µm thermally imprinted graphite composite captured by a confocal microscope.

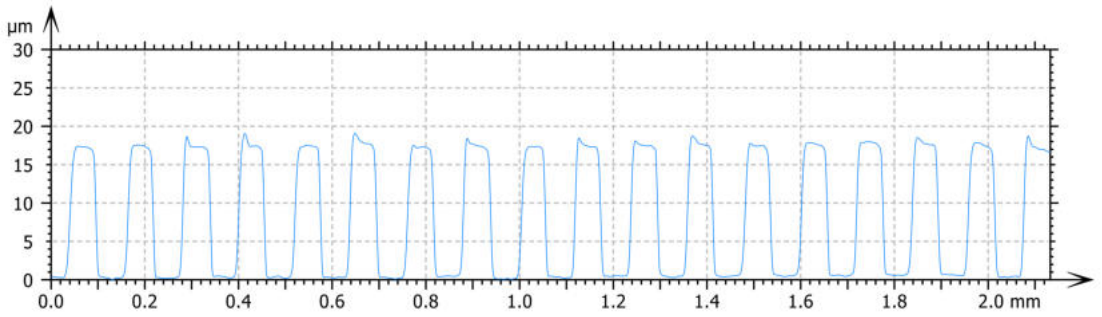

Parameter	Wert	Einheit
Länge	2.13	mm

Figure 21: Cross-section measurement of the second 60 µm thermally imprinted graphite composite captured by a confocal microscope.

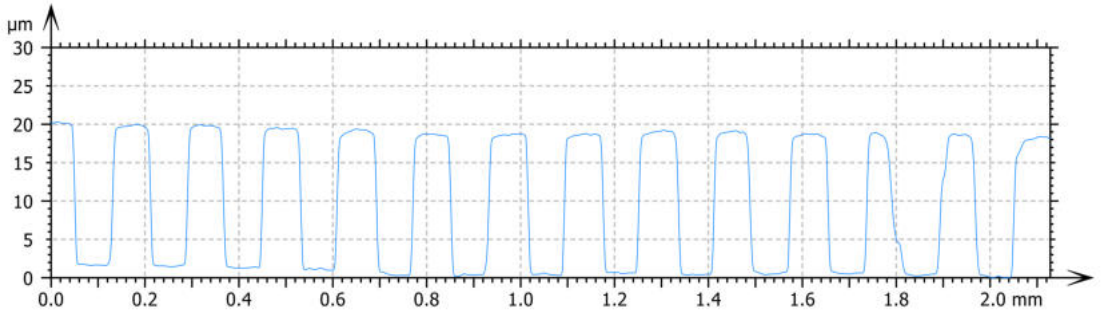

Parameter	Wert	Einheit
Länge	2.13	mm

Figure 22: Cross-section measurement of the 80 µm thermally imprinted graphite composite captured by a confocal microscope.

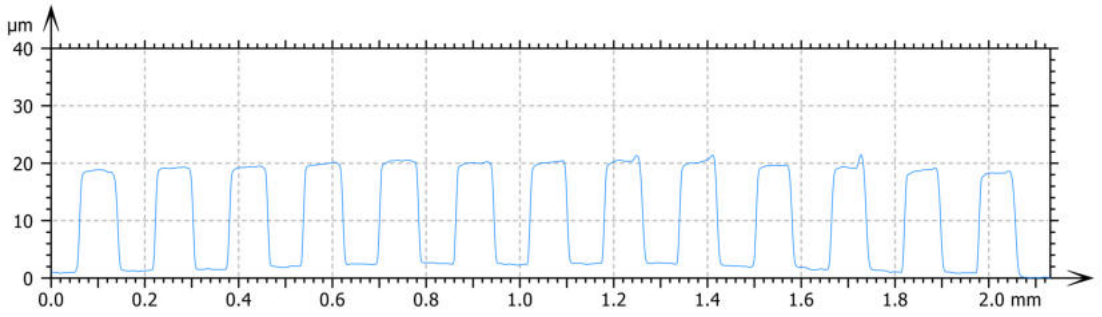

Parameter	Wert	Einheit
Länge	2.13	mm

Figure 23: Cross-section measurement of the second 80 µm thermally imprinted graphite composite captured by a confocal microscope.

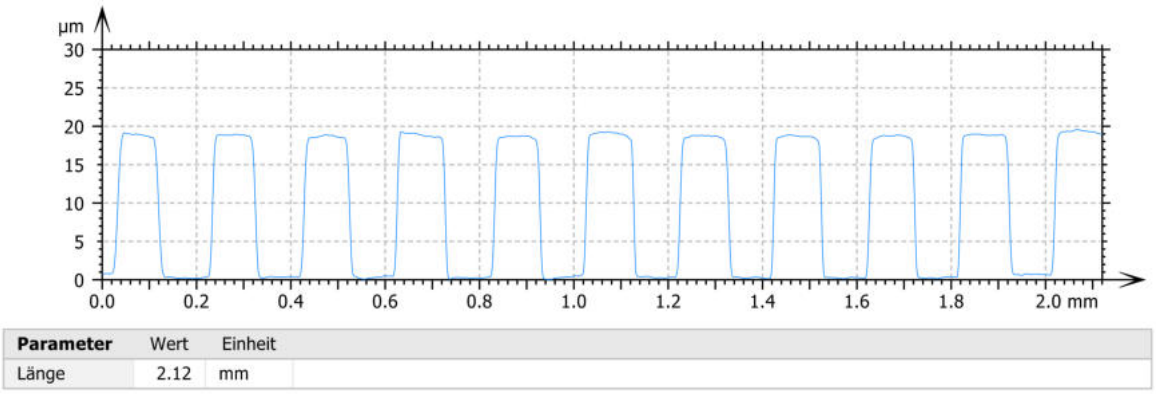

Parameter	Wert	Einheit
Länge	2.12	mm

Figure 24: Cross-section measurement of the 100 µm thermally imprinted graphite composite captured by a confocal microscope.

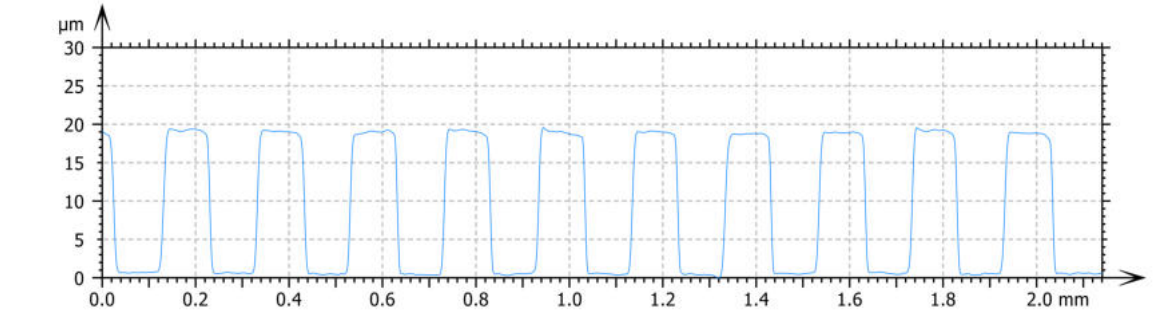

Parameter	Wert	Einheit
Länge	2.14	mm

Figure 25: Cross-section measurement of the second 100 µm thermally imprinted graphite composite captured by a confocal microscope.

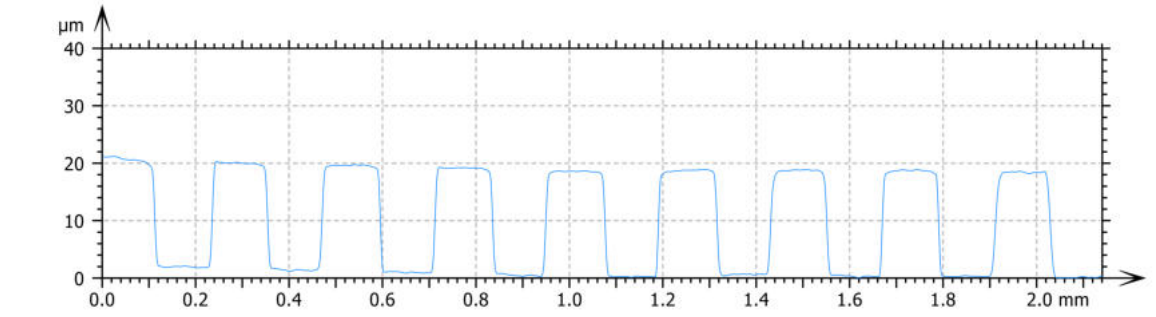

Parameter	Wert	Einheit
Länge	2.14	mm

Figure 26: Cross-section measurement of the 120 µm thermally imprinted graphite composite captured by a confocal microscope.

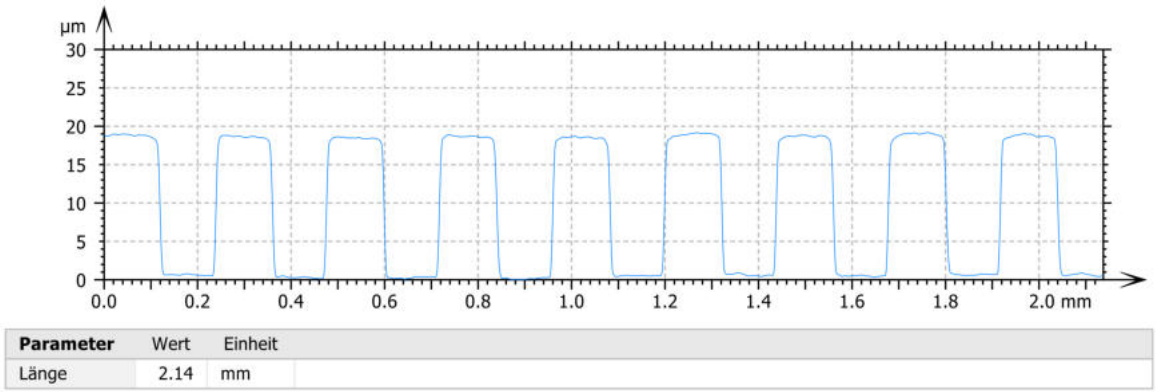

Figure 27: Cross-section measurement of the second 120 µm thermally imprinted graphite composite captured by a confocal microscope.

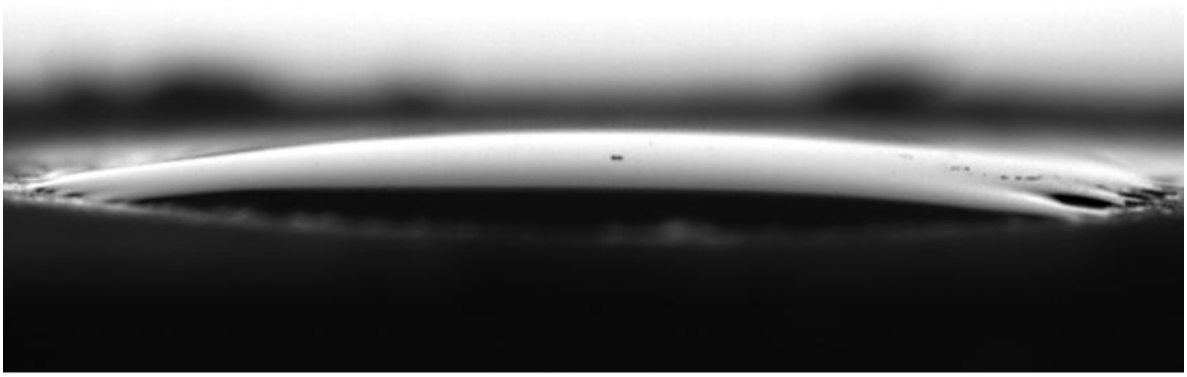

Figure 28: Contact angle measurement after oxidazation without low surface energy coating.

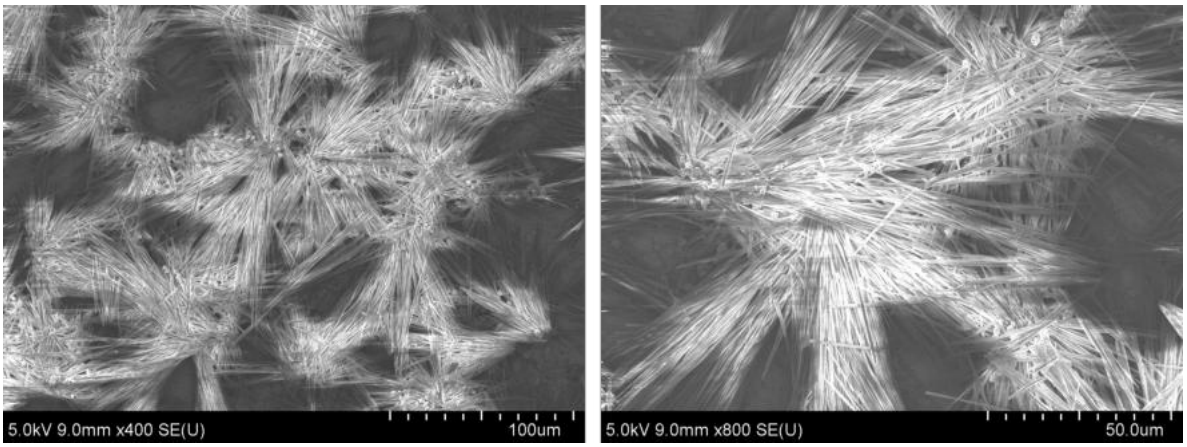

Figure 29: Top view SEM recordings of the copper nanostructures coated with 5 mmol/L lauric acid after 24 h.

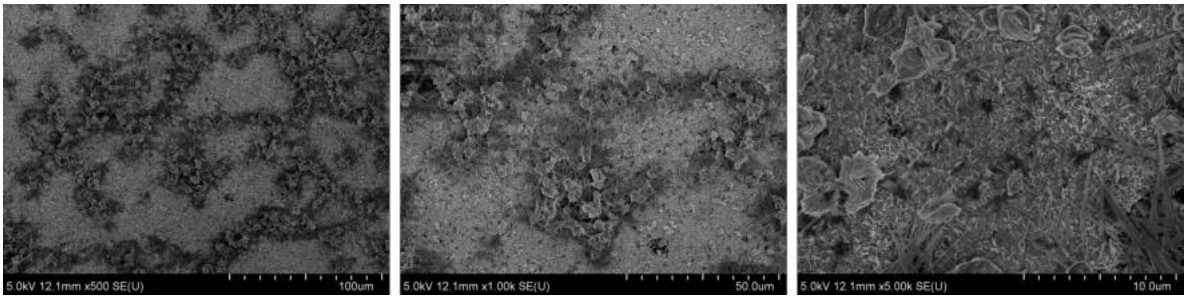

Figure 30: Top view SEM recordings of the copper nanostructures coated with 10 mmol/L lauric acid after 24 h.

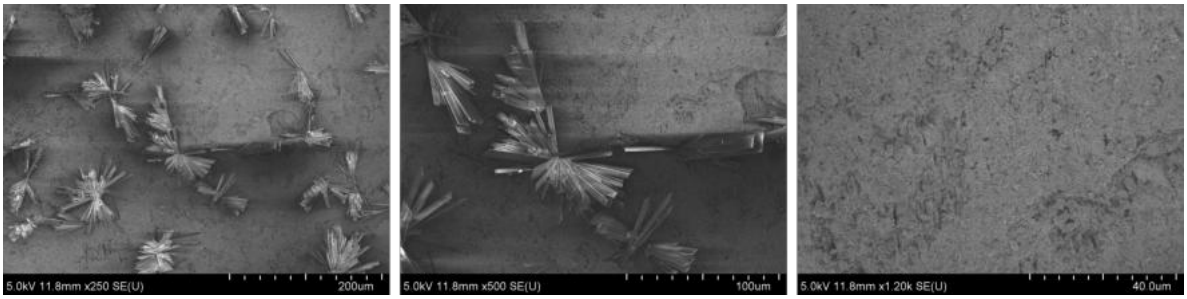

Figure 31: Top view SEM recordings of the copper nanostructures coated with 20 mmol/L lauric acid after 24 h.

Supporting Information for Chapter 3

Heat flux densities

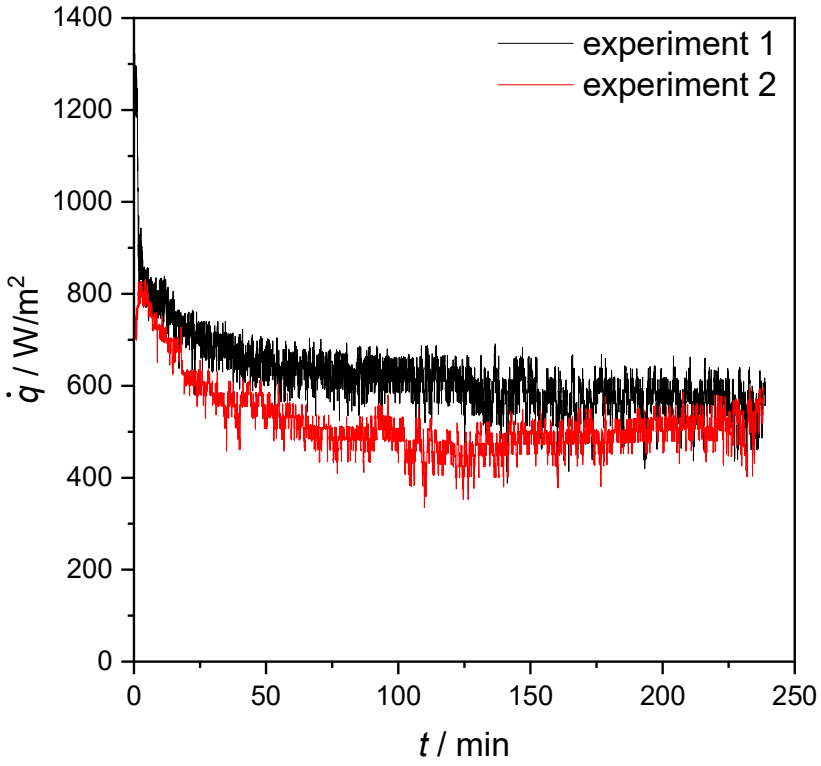

Figure 32: Heat flow density $\dot{q}$ of SS at a RH of $\varphi = 60$ %.

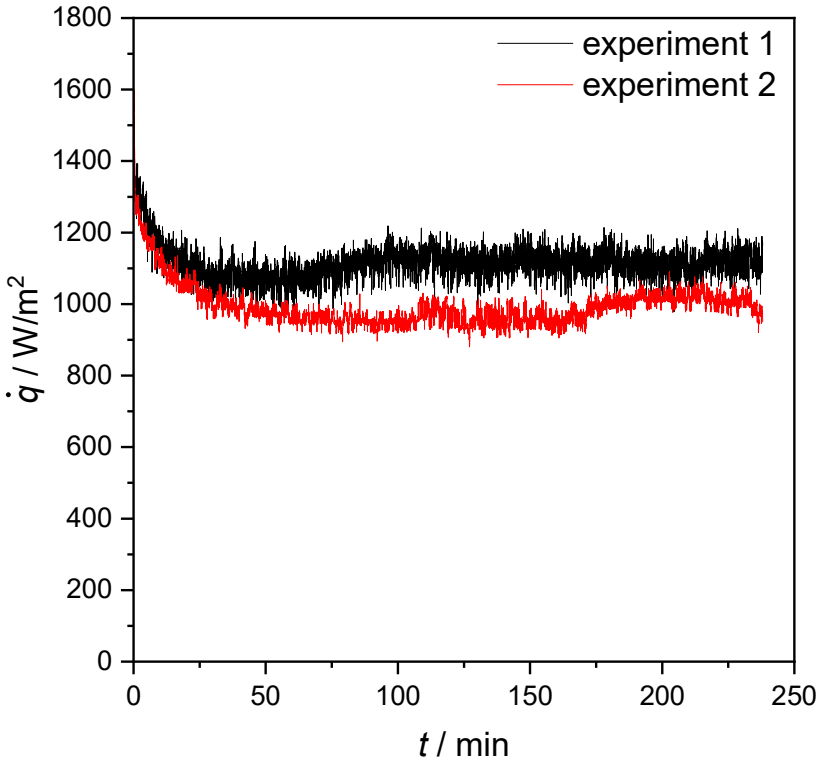

Figure 33: Heat flow density $\dot{q}$ of SS at a RH of $\varphi = 80$ %.

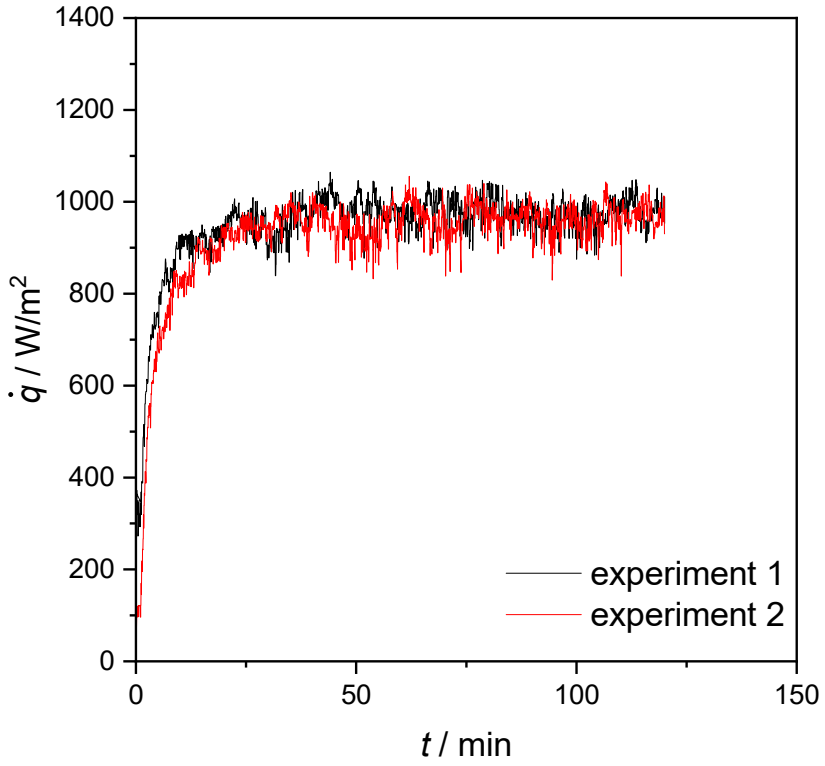

Figure 34: Heat flow density $\dot{q}$ of SS at a RH of $\varphi = 100$ %.

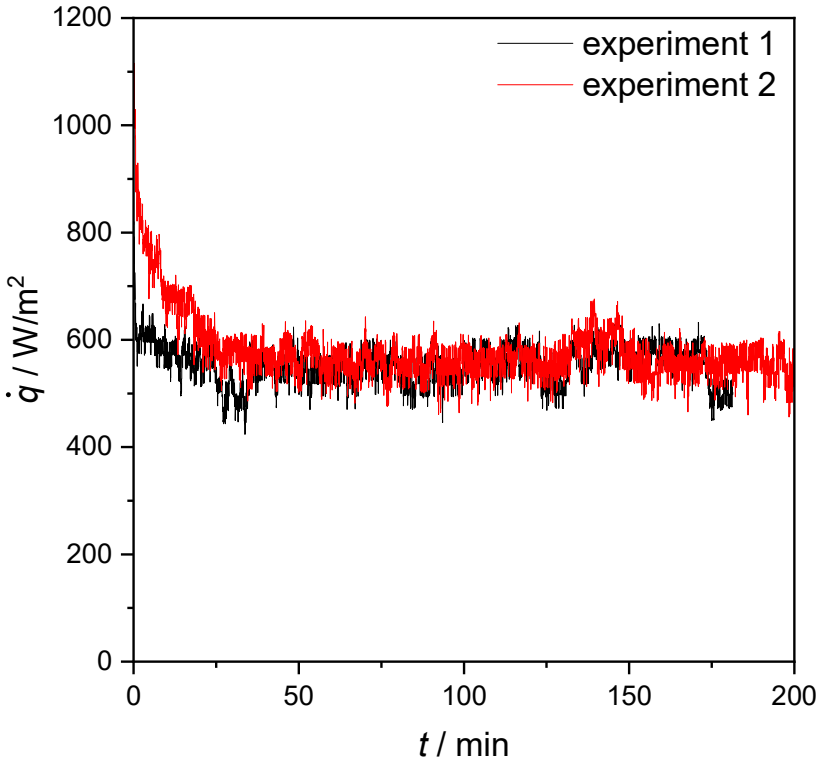

Figure 35: Heat flow density $\dot{q}$ of GC at a RH of $\varphi = 60$ %.

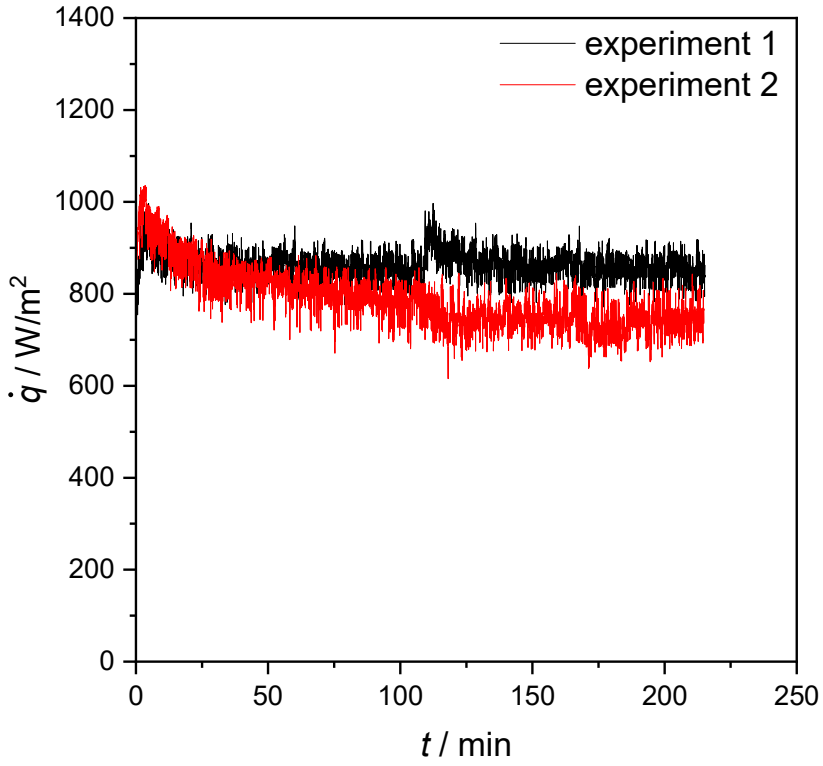

Figure 36: Heat flow density $\dot{q}$ of GC at a RH of $\varphi = 80$ %.

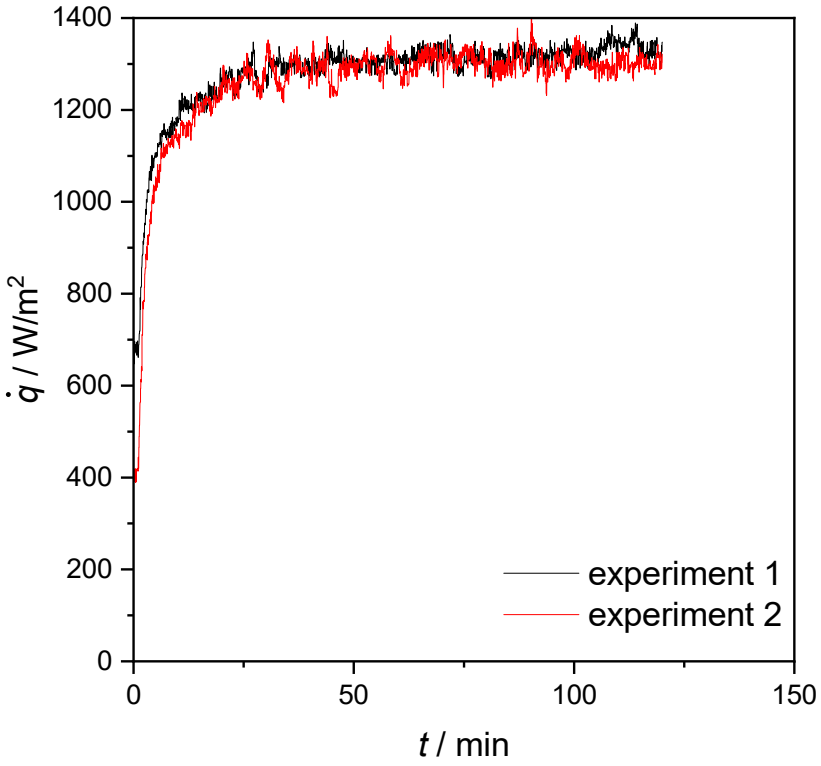

Figure 37: Heat flow density $\dot{q}$ of GC at a RH of $\varphi = 100$ %.

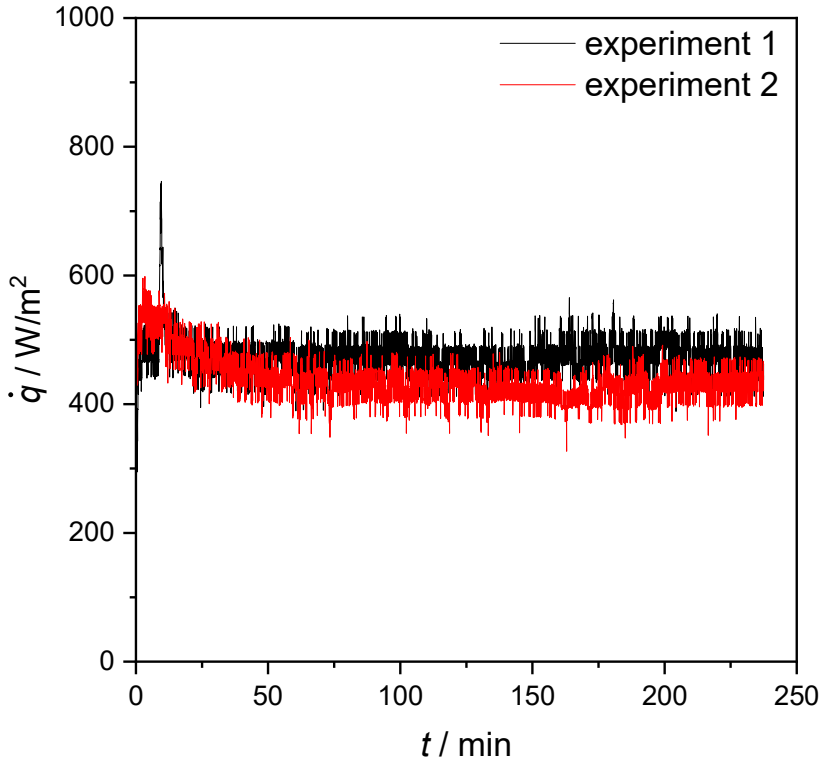

Figure 38: Heat flow density $\dot{q}$ of SHGC at a RH of $\varphi = 60$ %.

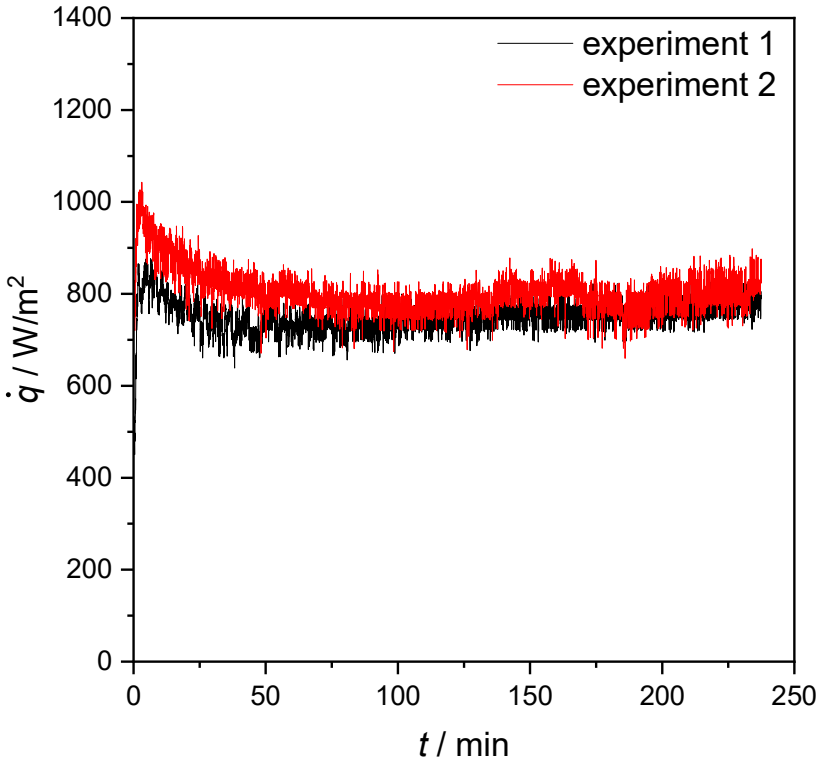

Figure 39: Heat flow density $\dot{q}$ of SHGC at a RH of $\varphi = 80$ %.

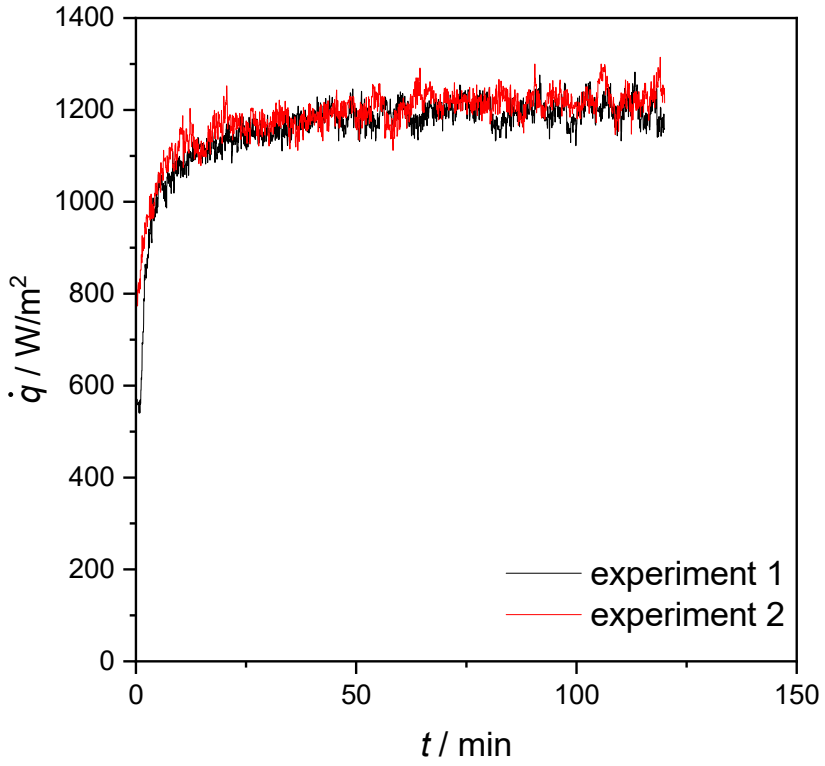

Figure 40: Heat flow density $\dot{q}$ of SHGC at a RH of $\varphi = 10$ %.

CFD simulations

Air

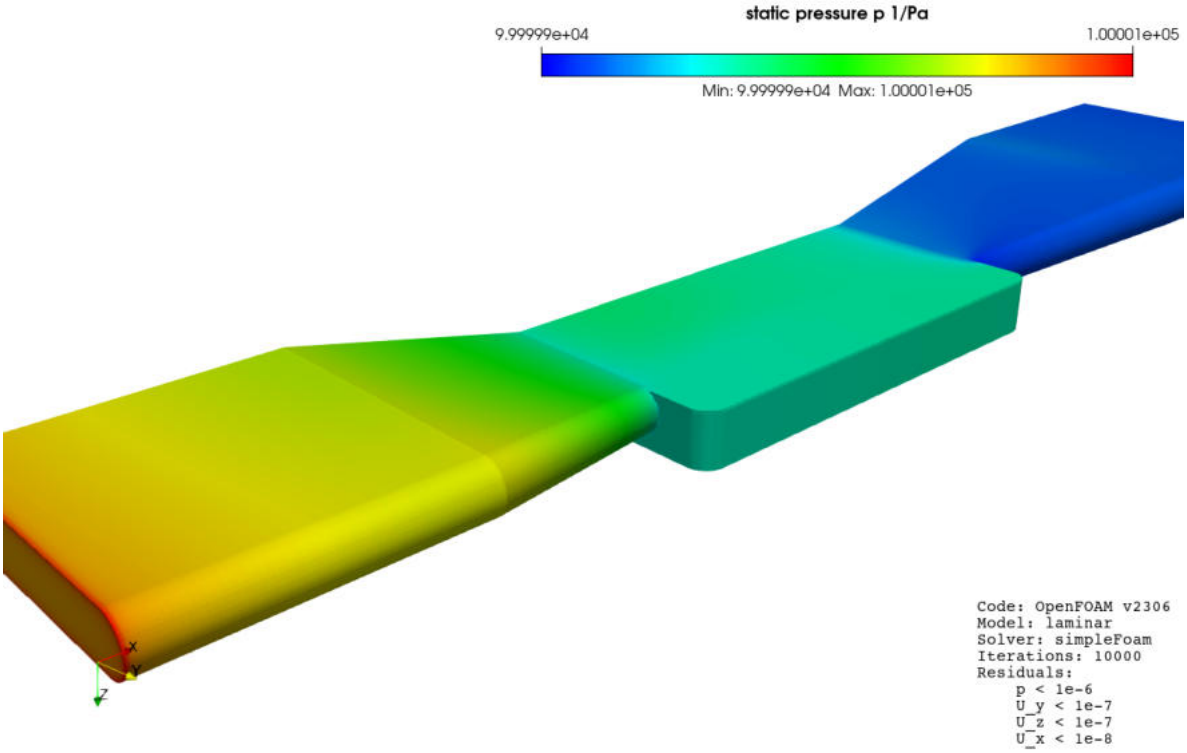

Figure 41: CFD simulation of the laminar air flow - pressure view.

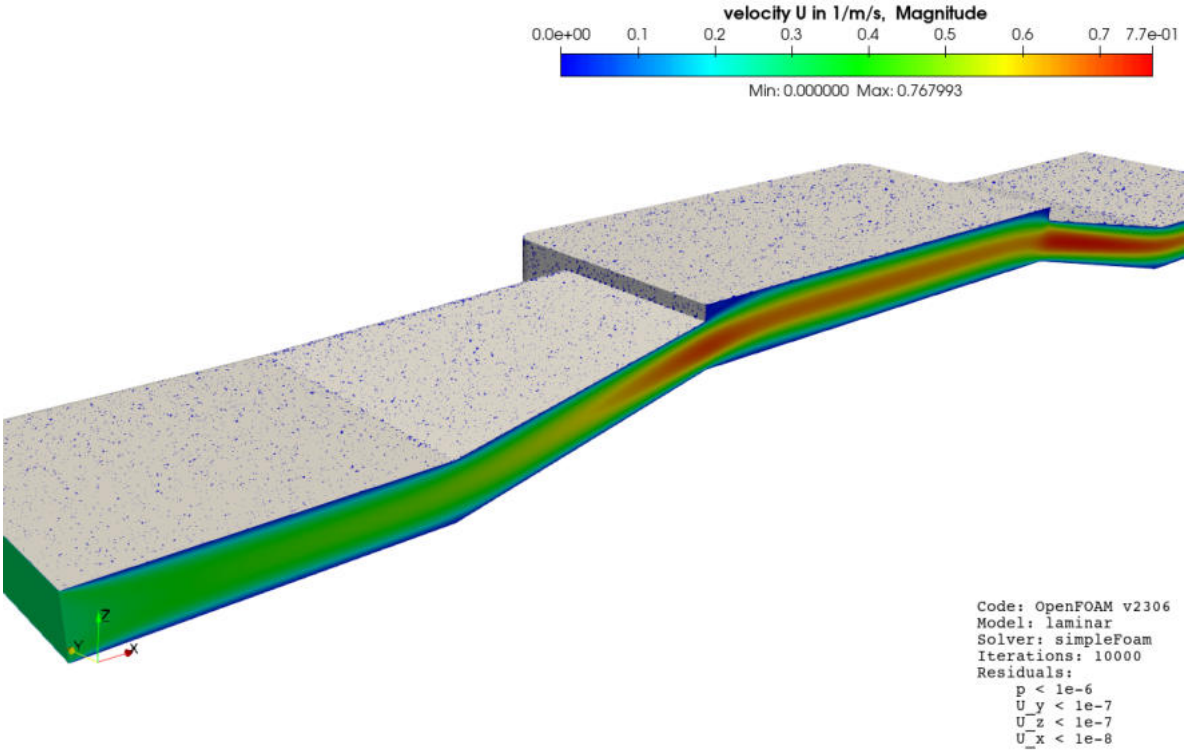

Figure 42: CFD simulation of the laminar air flow - velocity view.

Water

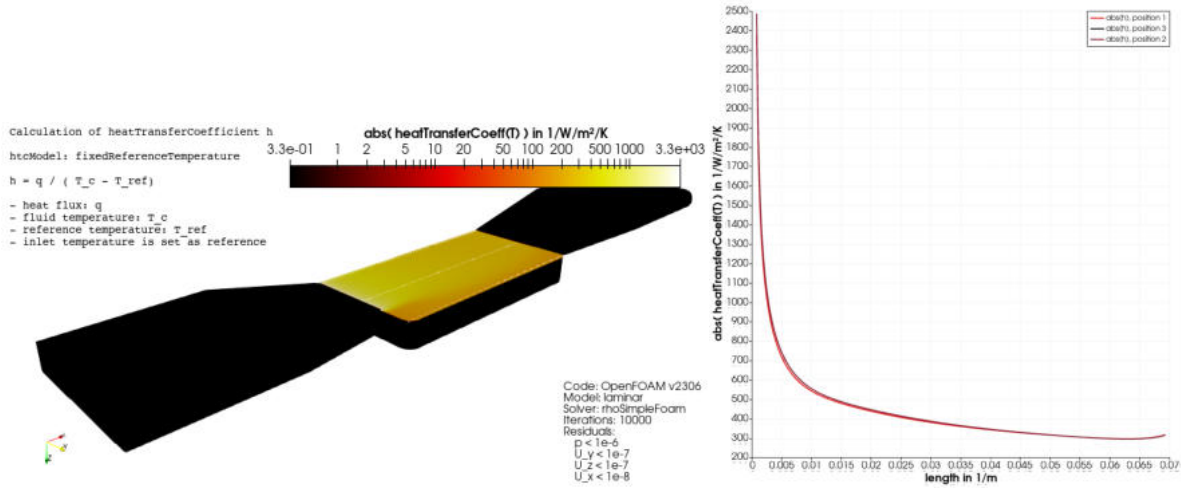

(a) (b)

Figure 43: Results of the CFD analysis of the HTC of SHGC of the cooling water circuit for 60% RH 20°C condensation experiment 1.

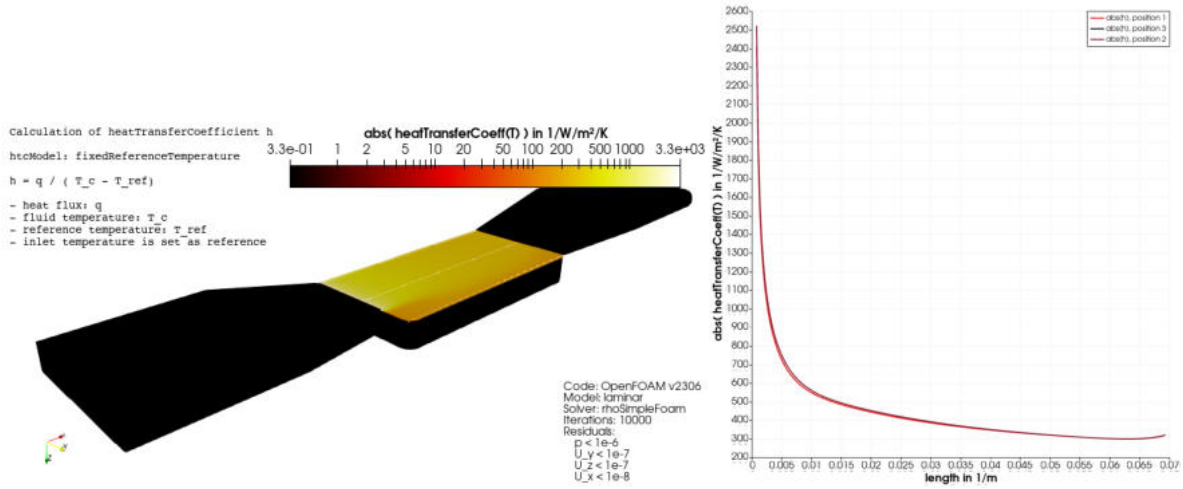

(a) (b)

Figure 44: Results of the CFD analysis of the HTC of SHGC of the cooling water circuit for 60% RH 20°C condensation experiment 2.

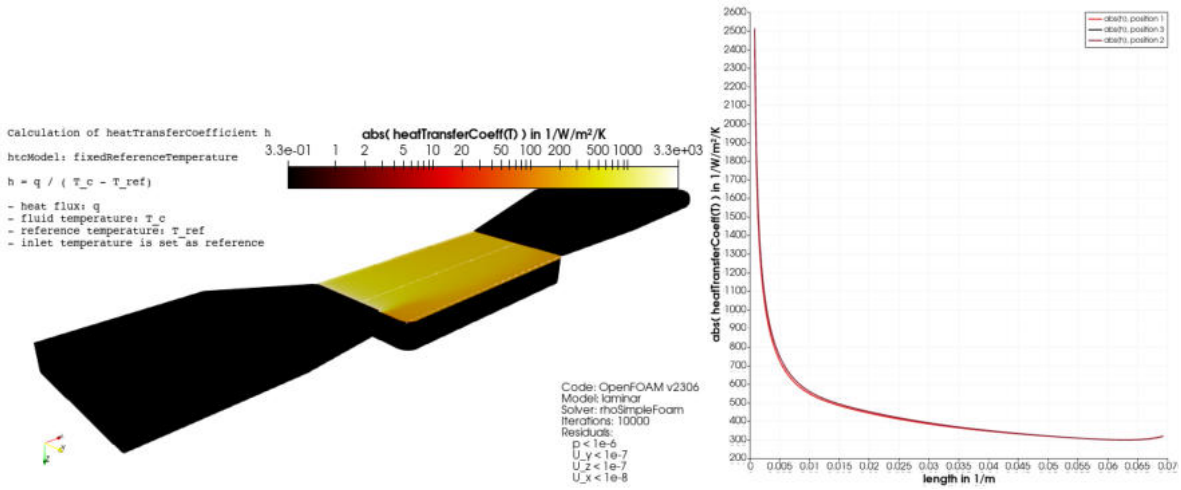

(a) **(b)**

Figure 45: Results of the CFD analysis of the HTC of SHGC of the cooling water circuit for 80% RH 20°C condensation experiment 1.

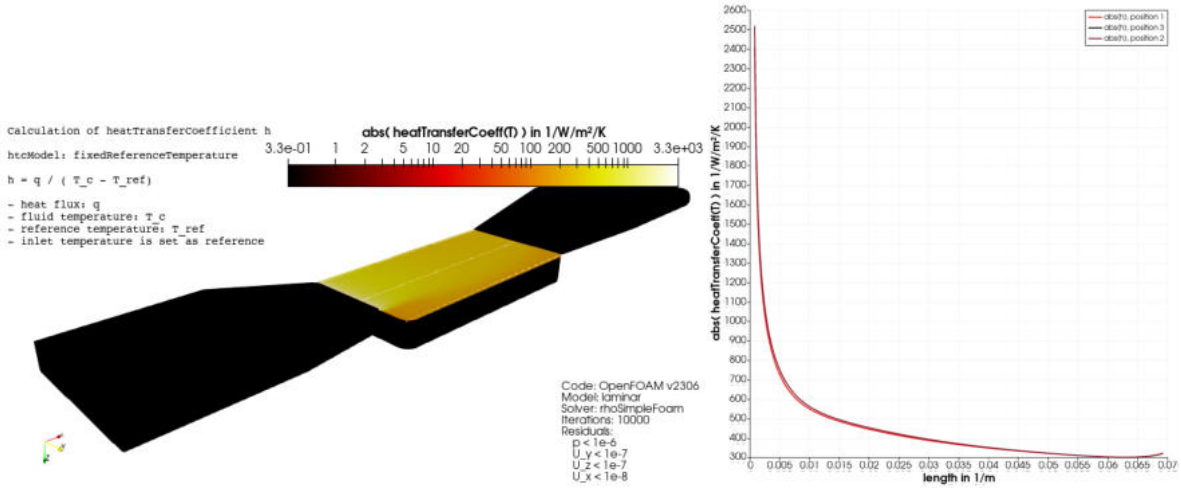

(a) **(b)**

Figure 46: Results of the CFD analysis of the HTC of SHGC of the cooling water circuit for 80% RH 20°C condensation experiment 2.

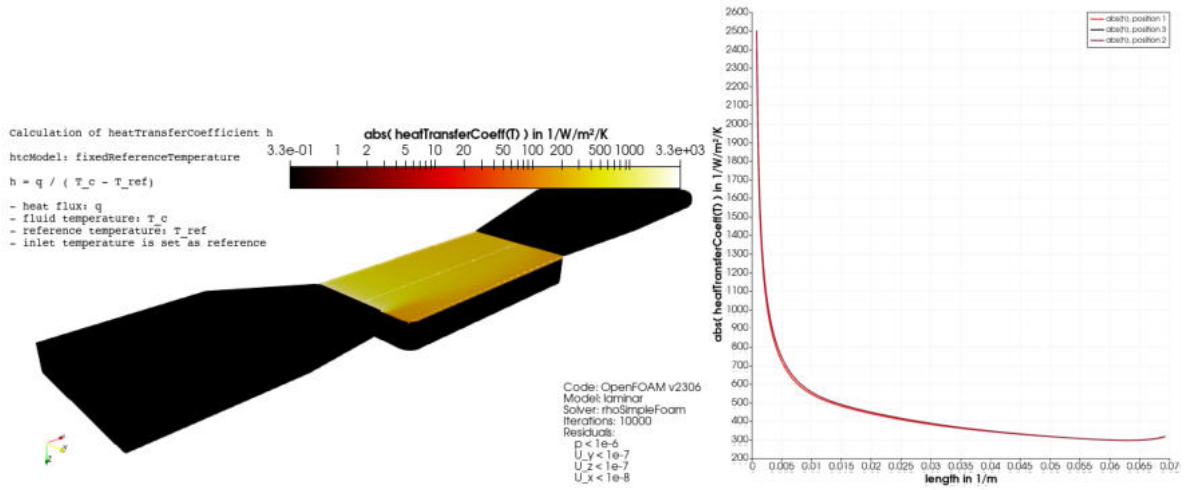

(a) **(b)**

Figure 47: Results of the CFD analysis of the HTC of GC of the cooling water circuit for 60% RH 20°C condensation experiment 1.

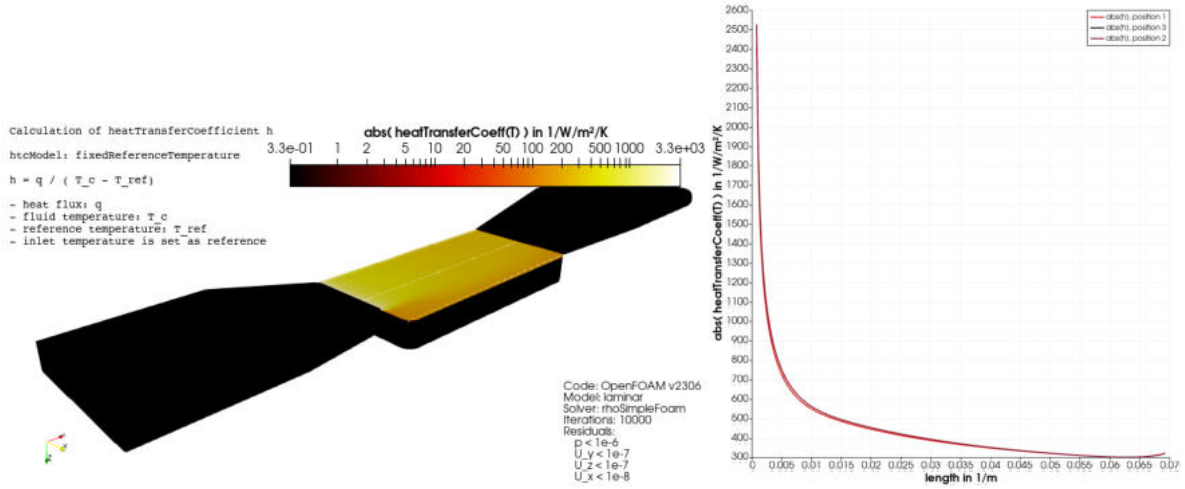

(a) **(b)**

Figure 48: Results of the CFD analysis of the HTC of GC of the cooling water circuit for 60% RH 20°C condensation experiment 2.

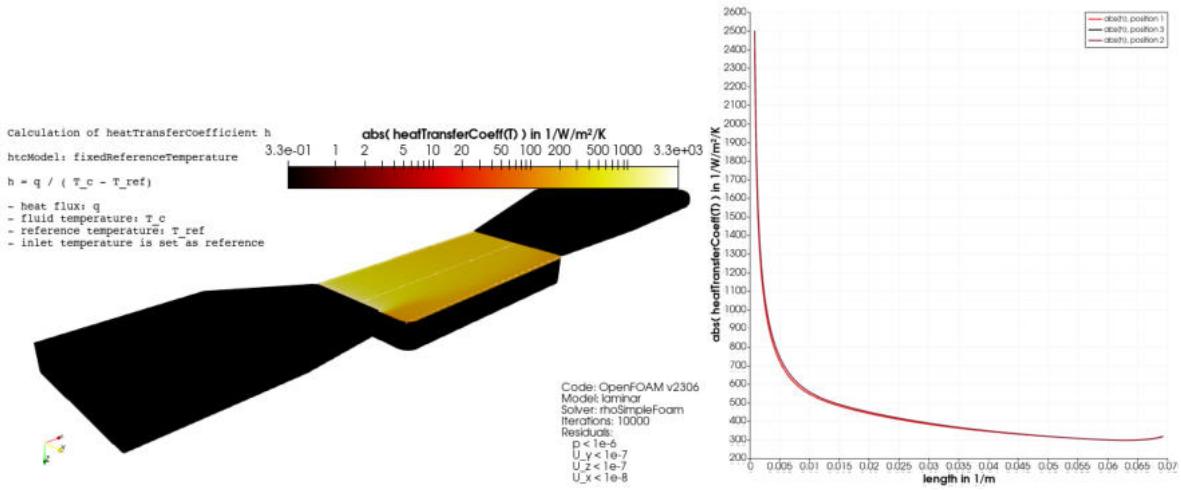

(a) **(b)**

Figure 49: Results of the CFD analysis of the HTC of GC of the cooling water circuit for 80% RH 20°C condensation experiment 1.

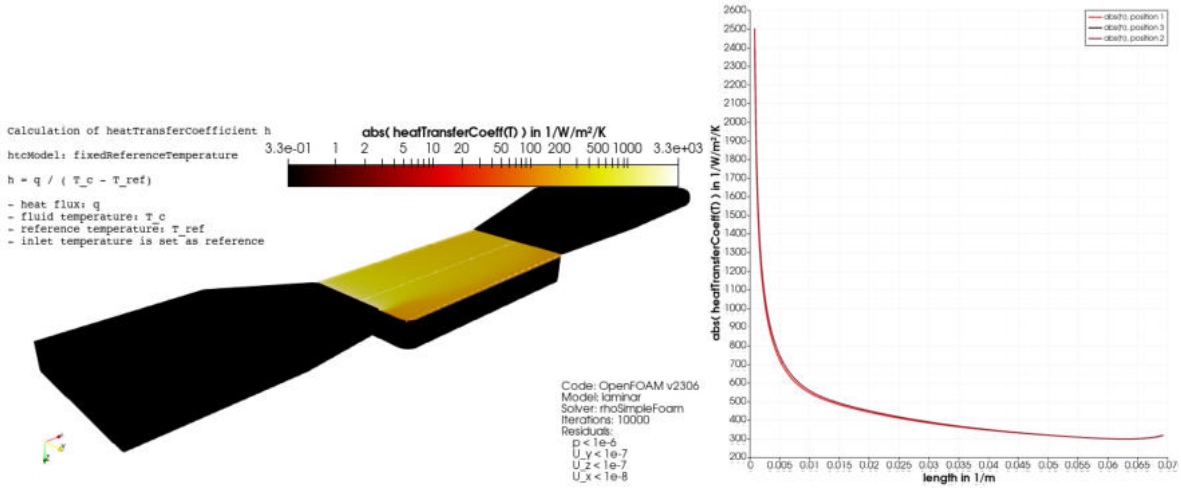

(a) **(b)**

Figure 50: Results of the CFD analysis of the HTC of GC of the cooling water circuit for 80% RH 20°C condensation experiment 2.

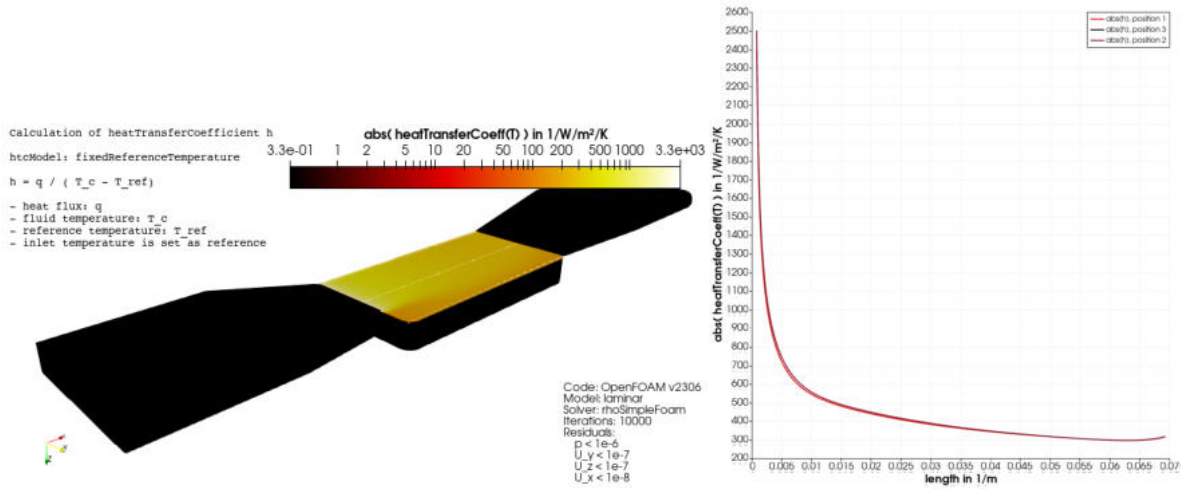

(a) **(b)**

Figure 51: Results of the CFD analysis of the HTC of SS of the cooling water circuit for 60% RH 20°C condensation experiment 1.

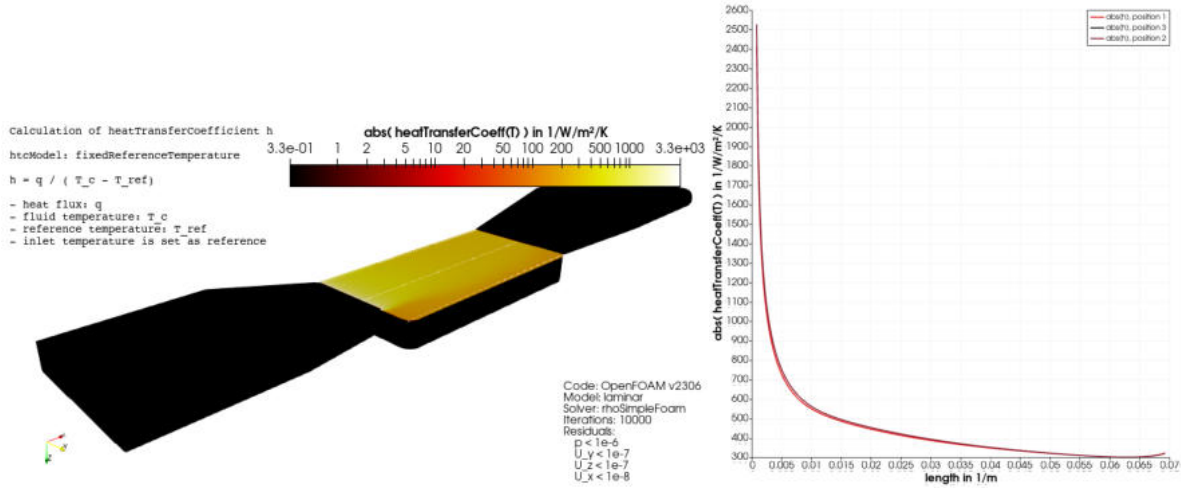

(a) **(b)**

Figure 52: Results of the CFD analysis of the HTC of SS of the cooling water circuit for 60% RH 20°C condensation experiment 2.

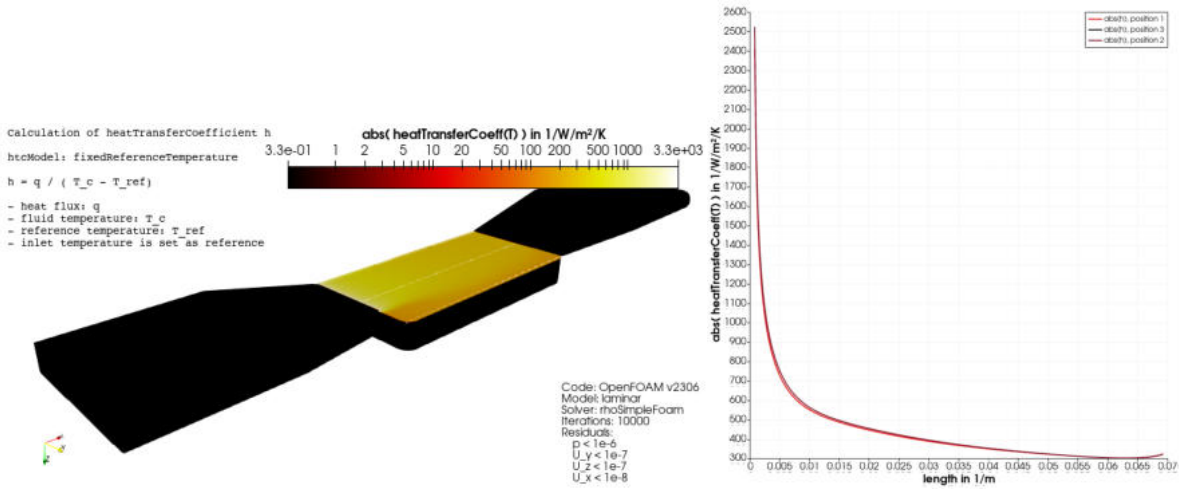

(a) **(b)**

Figure 53: Results of the CFD analysis of the HTC of SS of the cooling water circuit for 80% RH 20°C condensation experiment 1.

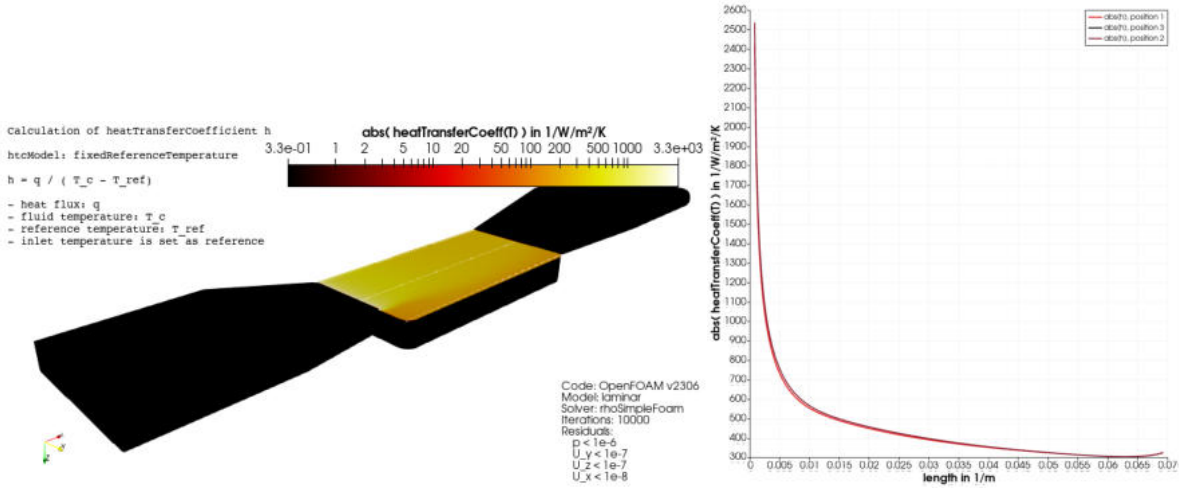

(a) **(b)**

Figure 54: Results of the CFD analysis of the HTC of SS of the cooling water circuit for 80% RH 20°C condensation experiment 2.

Detailed Contributor Roles Taxonomy

This chapter provides a detailed contributor roles taxonomy according to Allen et al. [98] of the publications and manuscripts redrafted in Chapters 2-4 including there Supplementary Information.

Chapter 2: Superhydrophobic Surfaces

Raphael Raab: conceptualization; formal analysis; methodology; project administration; validation; visualization; writing - original draft; writing - review & editing

Daniel Fotachov: data curation; investigation; methodology; writing - review & editing

Egbert Oesterschulze: writing - review & editing

Tobias Melchior: data curation; investigation; methodology; validation

Erik von Harbou: funding acquisition; resources; supervision; writing - review & editing

Hans-Jörg Bart: funding acquisition; resources; supervision; writing - review & editing

Chapter 3: Heat Transfer

Raphael Raab: conceptualization; formal analysis; methodology; project administration; validation; visualization; writing - original draft; writing - review & editing

Tobias Melchior: data curation; investigation; methodology; validation

Hannah Mennecke: data curation; investigation; methodology; validation

Daniel Fotachov: data curation; investigation; methodology; writing - review & editing

Egbert Oesterschulze: writing - review & editing

Thomas Reviol: data curation; investigation; methodology; writing - review & editing

Erik von Harbou: funding acquisition; resources; supervision; writing - review & editing

Hans-Jörg Bart: funding acquisition; resources; supervision; writing - review & editing

Chapter 4: PBE Modeling

Raphael Raab: conceptualization; formal analysis; methodology; project administration; validation; visualization; writing - original draft; writing - review & editing

Tobias Melchior: data curation; investigation; methodology; validation

Hannah Mennecke: data curation; investigation; methodology; validation

Daniel Fotachov: data curation; investigation; methodology; writing - review & editing

Egbert Oesterschulze: writing - review & editing

Thomas Reviol: data curation; investigation; methodology; writing - review & editing

Erik von Harbou: funding acquisition; resources; supervision; writing - review & editing

Hans-Jörg Bart: funding acquisition; resources; supervision; writing - review & editing

Publication List

The following list of scientific works was published by the author as part of his research.

Journal Articles

- J. M. Spörl, F. Batti, M.-P. Vocht, R. Raab, A. Müller, F. Hermanutz, and M. R. Buchmeister, "Ionic Liquid Approach Toward Manufacture and Full Recycling of All-Cellulose Composites," *Macromolecular Materials and Engineering*, vol. 303, no. 1, 2018. DOI: `https://doi.org/10.1002/mame.201700335`
- A. Mühlbauer, O. Böck, R. Raab, M. W. Hlawitschka, and H.-J. Bart, "Solid Particle Effects in Centi-scale Slurry Bubble Columns," *Chemie Ingenieur Technik*, vol. 93, no. 1-2, 2021. `https://doi.org/10.1002/cite.202000136`
- D. Fotachov, R. Raab, H.-J. Bart, and E. Oesterschulze, "Drainage during Condensation on Microgrooved Biphilic Surfaces," *Langmuir*, vol 40, no. 2, 2023. DOI: `https://doi.org/10.1021/acs.langmuir.3c02433`
- R. Raab, D. Fotachov, E. Oesterschulze, T. Melchior, E. von Harbou, and H.-J. Bart, "Hierarchical Structured Superhydrophobic Surfaces on Graphite Composites," *Applied Polymer Science*, vol. 142, no. 11, 2025. DOI: `https://doi.org/10.1002/app.56598`.

Lectures and Speeches

- R. Raab, D. Fotachov, E. Oesterschulze, E. v. Harbou, and H.-J. Bart, Conference Lecture, Topic: "Improved Condensation on Hierarchically Structured Surfaces," Presented at: Symposium Process Design, Raitenhaslach, Germany, October 2022
- R. Raab, D. Fotachov, T. Melchior, A. Przyklenk, H. Mennecke, E. Oesterschulze, E. v. Harbou, and H.-J. Bart, Conference Lecture, Topic: "Improved Condensation on Hierarchically Structured Polymers," Presented at: ACHEMA, Frankfurt am Main, Germany, June 2024
- R. Raab, D. Fotachov, T. Melchior, M. Vu, B. Storck, E. Oesterschulze, E. v. Harbou, and H.-J. Bart, Conference Lecture, Topic: "Enhanced Heat Transfer due to Dropwise Condensation caused by Hierarchical Structuring of Polymer Composites," Presented at: CHISA, Prague, Czech Republic, August 2024

Conference Posters

- R. Raab, D. Fotachov, T. Melchior, E. Oesterschulze, E. v. Harbou, and H.-J. Bart, "Improved Condensation on Structured Silicon Wafers," Presented at: Jahrestreffen der ProcessNet-Fachgruppen Computational Fluid Dynamics und Wärme- und Stoffübertragung, Frankfurt am Main, Germany, March 2023
- R. Raab, D. Fotachov, T. Melchior, M. Vu, S. Karazma, E. Oesterschulze, E. v. Harbou, and H.-J. Bart, "Condensation Behavior and Aging of Black Silicon and Embossed Polymers," Presented at: 11th International Conference On Boiling and Condensation Heat Transfer, Edinburgh, Scotland, Mai 2023
- R. Raab, D. Fotachov, T. Melchior, M. Vu, S. Karazma, E. Oesterschulze, E. v. Harbou, and H.-J. Bart, "Improved Condensation on Strucutured Polymers," Presented at: 13th European Congress of Chemical Engineering and 6th European Congress of Applied Biotechnology (ECCE13/ECAB6), Berlin, Germany, September 2023
- R. Raab, D. Fotachov, E. Oesterschulze, E. v. Harbou, and H.-J. Bart, "Enhanced Heat Transfer with Hierarchical Structuring of Polymer Composites," Presented at: Jahrestreffen der DECHEMA-Fachgruppe Fluidverfahrenstechnik, Bochum, Germany, March 2024

Supervised Student Theses

The following student theses were prepared under the supervision of the author of the present dissertation as part of the author's research program.

- J. Hau, "Experimental investigations with regard to improved condensation on modified silicon masters", Bachelor Thesis, Laboratory of Reaction and Fluid Process Engineering, RPTU Kaiserslautern, Germany, May 2021
- M. Vu, "Construction and commissioning of a test track for condensation experiments", Student Research Project, Laboratory of Reaction and Fluid Process Engineering, RPTU Kaiserslautern, Germany, October 2021
- J. Tran "Improved condensation for economical drinking water generation", DAAD RISE Program, Laboratory of Reaction and Fluid Process Engineering, RPTU Kaiserslautern, Germany, August 2022
- F. Youssef, "Investigation of the flow behavior over microstructured components with CFD analysis", Bachelor Thesis, Laboratory of Reaction and Fluid Process Engineering, RPTU Kaiserslautern, Germany, April 2023
- T. Melchior, "Condensation behavior of water on plastic films and single drop condensation", Student Research Project, Laboratory of Reaction and Fluid Process Engineering, RPTU Kaiserslautern, Germany, March 2023
- T. Melchior, "Investigation of the condensation behavior and embossing of structured surfaces", Bachelor Thesis, Laboratory of Reaction and Fluid Process Engineering, RPTU Kaiserslautern, Germany, September 2023
- J. Dieing, "CFD simulation of heat transfer through structured silicon wafers", Student Research Project, Laboratory of Reaction and Fluid Process Engineering, RPTU Kaiserslautern, Germany, October 2023
- V. Sivagunarajah, "Construction and commissioning of a heat exchanger cell manufactured using additive processes", Bachelor Thesis, Laboratory of Reaction and Fluid Process Engineering, RPTU Kaiserslautern, Germany, October 2023
- S. Karazma, "Investigation of the condensation behavior of microstructured polymer surfaces", Student Research Project, Laboratory of Reaction and Fluid Process Engineering, RPTU Kaiserslautern, Germany, April 2024
- B. Storck, "Experimental investigation of the heat transfer of hierarchically structured polymers with regard to condensation", Bachelor Thesis, Laboratory of Reaction and Fluid Process Engineering, RPTU Kaiserslautern, Germany, Mai 2024

- A. Przyklenk, "Production and characterization of hierarchically structured, superhydrophobic graphite composites", Bachelor Thesis, Laboratory of Reaction and Fluid Process Engineering, RPTU Kaiserslautern, Germany, September 2024
- H. Mennecke, "Experimental investigation and modeling of droplet condensation", Student Research Project, Laboratory of Reaction and Fluid Process Engineering, RPTU Kaiserslautern, Germany, November 2024

Raphael Raab

Curriculum Vitae

Professional Experience

04/2021 - 12/2024	**Scientific Assistant** Laboratory of Reaction and Fluid Process Engineering University of Kaiserslautern-Landau, Kaiserslautern, Germany
05/2019 - 04/2021	**Research Assistant** Chair of Separation Science and Technology Technical University of Kaiserslautern, Kaiserslautern, Germany
05/2014 – 08/2018	**Working Student** Logistics Schaeffler Technologies AG & Co. KG, Homburg/Saar, Germany

Education

10/2013 - 05/2018	**Technische Universität Kaiserslautern** Bachelor of Science in Bio- und Chemieingenieurwissenschaften Kaiserslautern, Germany
08/2018 - 12/2018	**Thompson Rivers University** Master of Scienence semester abroad Kamloops, Canada
05/2018 - 04/2021	**Technische Universität Kaiserslautern** Master of Science in Bio- und Chemieingenieurwissenschaften Kaiserslautern, Germany